

# Towards Accurate and Robust Modeling of Fluid-Driven Fracture

by

Andre Macieira Braga Costa

Department of Mechanical Engineering and Materials Science  
Duke University

Date: \_\_\_\_\_

Approved:

---

John Dolbow, Advisor

---

Manolis Veveakis

---

Wilkins Aquino

---

Johann Guilleminot

---

Alvaro Coutinho

Dissertation submitted in partial fulfillment of the requirements for the degree of  
Doctor of Philosophy in the Department of Mechanical Engineering and Materials  
Science  
in the Graduate School of Duke University  
2023

## ABSTRACT

# Towards Accurate and Robust Modeling of Fluid-Driven Fracture

by

Andre Macieira Braga Costa

Department of Mechanical Engineering and Materials Science  
Duke University

Date: \_\_\_\_\_

Approved:

---

John Dolbow, Advisor

---

Manolis Veveakis

---

Wilkins Aquino

---

Johann Guilleminot

---

Alvaro Coutinho

An abstract of a dissertation submitted in partial fulfillment of the requirements for  
the degree of Doctor of Philosophy in the Department of Mechanical Engineering  
and Materials Science  
in the Graduate School of Duke University  
2023

Copyright © 2023 by Andre Macieira Braga Costa  
All rights reserved

# Abstract

This work advances a phase-field method for fluid-driven fractures and proposes a robust and efficient discretization framework. It begins by addressing a modeling challenge related to the application of pressure loads on diffuse crack surfaces. Along the way, a new J-Integral for pressurized fractures in a regularized context is developed.

Then, the focus turns to a hybrid method to model fluid-driven fracture propagation. A so-called multi-resolution method is presented that uses a combination of enrichment schemes with the phase-field method to address the complex fluid-fracture interaction that occurs during hydraulic fracture. On one hand, the phase-field method alleviates some of the difficulties associated with the geometric evolution of the fracture, which are usually the limiting aspect of purely enrichment-based schemes. On the other hand, the discrete representation allows for a better treatment of the fluid loads and crack apertures, which are the main challenges associated with phase-field approaches.

The multi-resolution method is first presented in a simplified scheme to treat two-dimensional problems. Various benchmark problems are used to verify the framework against well-known analytical solutions. The method is then extended to three-dimensions. A robust algorithm to handle planar cracks in 3D is developed and its extension to non-planar cases is discussed. Finally, opportunities for improvements and extensions are discussed, paving the road for future work in this area.

# Contents

<b>Abstract</b>	<b>iv</b>
<b>List of Tables</b>	<b>viii</b>
<b>List of Figures</b>	<b>ix</b>
<b>Acknowledgements</b>	<b>xiv</b>
<b>1 Introduction</b>	<b>1</b>
1.1 Motivation . . . . .	1
1.2 Background . . . . .	3
1.3 Research contributions . . . . .	8
<b>2 Revisiting the Pressure Loading of Phase-Field Fractures</b>	<b>11</b>
2.1 Introduction . . . . .	11
2.2 Model . . . . .	12
2.2.1 Quasi-static derivation . . . . .	13
2.2.2 Derivation using the maximum dissipation principle . . . . .	19
2.2.3 Constitutive choices of the phase-field formulation . . . . .	22
2.3 A J-Integral for pressurized cracks in a phase-field setting . . . . .	24
2.4 Finite Element Implementation . . . . .	30
2.5 Results . . . . .	32
2.5.1 Uniaxial bar under traction in a pressurized environment . . . . .	33
2.5.2 Crack nucleation from a pressurized hole . . . . .	36

2.5.3	Stable propagation of a pre-existing crack . . . . .	39
<b>3</b>	<b>A Multi-Resolution Approach for Hydraulic Fracture Simulation</b>	<b>45</b>
3.1	Introduction . . . . .	45
3.2	Model formulation . . . . .	46
3.2.1	Governing equations for hydraulic fracture . . . . .	46
3.2.2	The phase-field method for fracture . . . . .	51
3.3	Multi-resolution method . . . . .	54
3.3.1	General overview . . . . .	54
3.3.2	Global problem discretization . . . . .	56
3.3.3	Local problem initialization . . . . .	57
3.3.4	Local problem discretization . . . . .	60
3.3.5	Crack propagation: translating local damage updates into global crack extensions . . . . .	62
3.3.6	Algorithm summary . . . . .	65
3.4	Numerical Results . . . . .	67
3.4.1	KGD problems . . . . .	67
3.4.2	Poroelastic problem with coupled matrix-fracture flow . . . . .	75
3.4.3	Propagation around an inclusion . . . . .	80
<b>4</b>	<b>Extending the Multi-Resolution Approach to Three Dimensions</b>	<b>84</b>
4.1	Introduction . . . . .	84
4.2	Theory . . . . .	85
4.3	Algorithm for planar fractures . . . . .	87
4.3.1	Fracture front construction . . . . .	88
4.3.2	Tracking damage in the fracture front elements . . . . .	91
4.4	Numerical examples . . . . .	92
4.4.1	Two parallel circular fractures under fluid injection . . . . .	93

4.4.2	Merging two circular fractures . . . . .	98
4.5	Extension to non-planar fractures . . . . .	102
4.5.1	Overview of a propagation algorithm for non-planar fractures .	102
4.5.2	Example problem . . . . .	108
<b>5</b>	<b>Conclusions and Future Work</b>	<b>112</b>
<b>A</b>	<b>Equivalence to SIF condition</b>	<b>115</b>
	<b>Bibliography</b>	<b>121</b>
	<b>Biography</b>	<b>134</b>

# List of Tables

2.1	Material properties for uniaxial bar . . . . .	34
2.2	Material properties, geometric parameters and applied loads for crack initiation problem . . . . .	37
2.3	Parameters used for pressurized crack propagation problem . . . . .	41
2.4	Absolute error in $J$ vs. $G_c^{eff}$ for the pressurized crack propagation problem, as a function of regularization length. . . . .	43
3.1	Material properties and problem parameters for the toughness-dominated KGD problem . . . . .	69
3.2	Effect of subdomain size on the relative error in the crack length. . . . .	72
3.3	Material properties and problem parameters for the viscosity-dominated KGD problem . . . . .	73
3.4	Material properties for poroelastic problem . . . . .	77
3.5	Problem settings . . . . .	77
3.6	Material properties for inclusion problem . . . . .	81
3.7	Problem settings . . . . .	81
4.1	Material properties for planar fracture problems. . . . .	93
4.2	Domain dimensions . . . . .	95
4.3	Reference values used in the time series plots. . . . .	95
4.4	Domain dimensions . . . . .	99
4.5	Reference values used in the time series plots. . . . .	99
4.6	Material properties for non-planar fracture problem. . . . .	109

# List of Figures

1.1	These plots show the evolution of fracking, leading to it becoming the main source of oil and gas in the United States. The numbers shown in the graphs are behind the actual values mentioned in the text because the charts were last updated in 2015. Courtesy from the US Energy Information Administration. . . . .	2
1.2	Simplified depiction of an EGS system. Courtesy of Los Alamos National Laboratory. . . . .	3
2.1	Generic body containing cracks loaded in pressure. . . . .	13
2.2	(a) Unloaded virtual crack. (b) Pressure loaded virtual crack; . . . . .	16
2.3	(a) The contour paths $\zeta_{in}$ and $\zeta_{out}$ and subdomain $\Lambda$ , in the vicinity of a regularized crack.; (b) Color contour plot indicating the assumed variation in the function $q$ . . . . .	26
2.4	Uniaxial cohesive bar. . . . .	33
2.5	Traction-separation curves for pressurized uniaxial cohesive bar problem, obtained with various phase-field models: (a) (LVC) with linear indicator function; (b) (LVC) with quadratic indicator function; (c) (LVC) with $2d - d^2$ indicator function; and (d) Proposed approach (UVC) with linear indicator function. . . . .	35
2.6	(a) Problem schematic; (b) Mesh used in the computations, exploiting symmetry. . . . .	37
2.7	(a) Final crack pattern using proposed model; (b) Damage field using the model from [1]. . . . .	39
2.8	(a) Geometry and boundary conditions for pressurized crack propagation problem; (b) J-Integral domain function $q$ . . . . .	40

2.9	Reference results with the LVC formulation. Curves with $\ell = a/160$ are not shown, as they are almost identical to the ones with $\ell = a/80$ . (a) $I(d) = d$ ; (b) $I(d) = d^2$ ; (c) $I(d) = 2d - d^2$	42
2.10	Results with the proposed formulation (UVC) (a) $I(d) = d$ ; (b) $I(d) = d^2$ ; (c) $I(d) = 2d - d^2$	42
2.11	Convergence of the proposed formulation with $I(d) = d$	43
3.1	Schematic of a poroelastic rock with a fracture, inspired by [2]	47
3.2	Global domain $\Omega$ on the left and local domain $\Omega_L$ on the right. The surface corresponding to the local domain boundary $\partial\Omega_L$ is indicated within the global domain with the dashed red lines. The local domain is magnified to highlight the phase-field representation of the global crack $\Gamma$ .	54
3.3	Global domain $\Omega$ on the left and local domain $\Omega_L$ on the right. The nodes in the subset $\mathcal{K}$ , where $d$ is set to 1 are colored in yellow.	58
3.4	Illustration of global cells (in gray) in the neighborhood of a local element, indicated in pink. The matrix pressure at a quadrature point in the local element is calculated using an average of global pressures from neighboring cells $\{i\}$ , with weights corresponding to the distances $r_i$ between the quadrature point and the cell center.	59
3.5	(a): Illustration of the global crack tip and global tip element. (b) Case when the local tip falls inside the tip element. (c) Case when the local tip falls outside the tip element.	63
3.6	(a): Construction of the segment connecting global and local tips. (b) New crack segment to be added. (c) Update of the global crack tip and global tip element.	64
3.7	Multi-resolution solution algorithm.	67
3.8	(a) Schematic of the KGD problem, inspired by [3]. (b) Computational domain for the KGD problem (not to scale).	68
3.9	Comparison of numerical results and analytical solution for the toughness-dominated KGD problem: (a) crack length vs. time and (b) pressure vs. time.	71
3.10	Study of the effects of subdomain size on the results of the toughness-dominated KGD problem: (a) influence on predicted crack length and (b) predicted pressure.	72

3.11 Numerical results and analytical solution for the viscosity-dominated KGD problem: (a) crack length vs. time; and (b) inlet pressure vs. time. . . . .	75
3.12 Geometry and notation for the coupled poroelastic-fracture problem. . . . .	76
3.13 Results from the fully coupled poroelastic-fracture problem for the multi-resolution method (with and without driving pressures) and a standard phase-field model: (a) crack size over time, (b) inlet pressure. The time for crack propagation ( $t_{ref}$ ) in the phase-field model and the corresponding inlet pressure ( $p_{ref}$ ) are used as references for the dimensionless charts above. . . . .	79
3.14 Fields from the coupled poroelastic-fracture problem, taken at the end of the simulation, contrasting results from the multi-resolution scheme without the driving pressures (top row) to those obtained using a standard phase-field model of fracture in poroelastic media (bottom row). (a) Contour plots of the damage field. (b) Contour plots of the pressure field. . . . .	79
3.15 Geometry for the inclusion problem. . . . .	80
3.16 Crack paths for the inclusion problem: (a) 2X stiffer inclusion; (b) 7X stiffer inclusion; and (c) 15X stiffer inclusion. . . . .	82
3.17 Inlet pressure as a function of time for the three inclusion problems, corresponding to inclusions with different stiffnesses. The reference values of the pressure $p_{ref}$ and time $t_{ref}$ were defined as the minimum pressure that led to fracture growth and the associated time, considering the simulated injection rate. . . . .	83
4.1 Illustrative example of a 3D surface with gaps, because surface elements do not connect smoothly. Extracted from [4]. . . . .	86
4.2 Multi-resolution solution algorithm. . . . .	87
4.3 Fractured element A and some of its neighbors. Element B is assigned to the front because the face it shares with A is fractured. C is not on the front because the face it shares with A is not fractured. D is not on the front because it does not share a face with a fractured element. . . . .	89
4.4 Penny shaped crack discretized in a coarse grid. Red elements represent the fractured elements (which contain EFEM enrichments). The fracture front elements are shown in green. . . . .	89
4.5 Sequence of steps performed during crack propagation. . . . .	90

4.6	Schematic of the problem geometry. . . . .	95
4.7	Two quantities of interest for the parallel fracture problem. On the left, the time series of the pressure at the injection point, on the right, the fracture aperture. Both plots show results scaled by reference values, calculated at the onset of propagation. . . . .	96
4.8	Snapshots of the simulated propagation. The left side of the figures shows the discrete fracture colored in grayscale according to the aperture and the subdomain colored according the damage value. The right side shows the pressure field in the global domain. (a) Snapshot $t/t_{ref} = 0$ ; (b) $t/t_{ref} = 1.5$ ; (c) $t/t_{ref} = 3$ ; and (d) $t/t_{ref} = 4.5$ . . . . .	97
4.9	Schematic of the geometry for the merging problem. . . . .	100
4.10	Two quantities of interest for the merging fracture problem. On the left, the time series of the pressure at the injection point, on the right, the fracture aperture. Both plots show results scaled by reference values, calculated at the onset of propagation. . . . .	100
4.11	Snapshots of the simulated propagation. The discrete fracture is colored in grayscale according to the aperture and the subdomain colored according the damage value. (a) Snapshot $t/t_{ref} = 0$ ; (b) $t/t_{ref} = 1.3$ ; (c) $t/t_{ref} = 2.6$ ; (d) $t/t_{ref} = 3.9$ ; (e) $t/t_{ref} = 5.2$ ; and (f) $t/t_{ref} = 6.5$ . . . . .	101
4.12	This figure shows a pathological case for the topological criterion proposed in 4.3.2. The element on the right is only partially damaged, however, the counts of cut edges and faces are higher than the ones for the element on the left, which is indeed fully cut. . . . .	103
4.13	Basic shapes for a planar cut in a brick element. . . . .	105
4.14	This figure shows how the aperture field computed with EFEM approaches an analytical solution as the mesh is refined. Note that the aperture field is discontinuity across element boundaries. Courtesy from [5] . . . . .	106
4.15	Flux in discontinuous fracture surfaces. D1 and D2 are the intersections of the damage field with the edges and serve to define a line segment that can be used to calculate the flux between the two fracture elements. . . . .	107
4.16	Enhancements to 4.2 to allow for non-planar fracture propagation. . .	108
4.17	Schematic of the edge crack problem. The load of the top surface is inclined 45deg, which leads to a curved fracture path. . . . .	111



# Acknowledgements

I want to thank Professor Ilinca Stanciulescu, with whom I worked during my undergraduate years, for her patient guidance in my first research project. I want to thank Dr. Henrique Versieux, my Masters advisor, for introducing me to the theory of phase-field and the mathematical background that was very important to me in this Ph.D. I want to thank Professor John Dolbow, my advisor, for his valuable advice, barbecues and Thanksgiving dinners, and for proofreading several poorly written drafts of mine. I want to thank Professors Wilkins Aquino, Johann Guilleminot, Manolis Vveakis for their time and service as my committee members. Most of the work in this dissertation originated from their course projects. I want to thank Dr. Matteo Cusini, Dr. Fan Fei, Dr. Tao Jin and Dr. Randolph Settgast from the Lawrence Livermore National Laboratory for many enlightening discussions. I want to thank my colleagues Dr. Gary Hu and Dr. Rudy Geelen for babysitting me during my first semesters as a graduate student.

I also want to thank my mom Celia, dad Fernando and sister Julia for all the support in these difficult years away from home. As well as my girlfriend Leticia for going through so much time on a long-distance relationship and for all our daily calls over these years.

# 1

## Introduction

### 1.1 Motivation

Hydraulic fracturing, commonly known as fracking, is a complex process that involves the initiation and/or propagation of fractures resulting from the application of hydraulic pressure by a fluid. This technique finds extensive applications, particularly in the field of geology. [3].

In the realm of oil and gas production, fracking is used to stimulate tight shale reservoirs, creating pathways for the extraction of shale gas. Since the pioneering field test at the Hugoton field in 1947, advancements in fracking technology, such as multi-stage hydraulic fracturing and horizontal drilling, have significantly enhanced productivity in these reservoirs. In fact, recent data from the US Energy Information Administration[6, 7] reveals that a significant portion, around 66% of all oil and 80% of all gas, produced in the United States comes from wells that undergo hydraulic fracturing. (See Figure 1.1.)

Hydraulic fracturing also plays a crucial role in geothermal energy, which offers a promising avenue for generating renewable, carbon-free electricity. In general, the biggest challenge of these geothermal systems is the low permeability of most

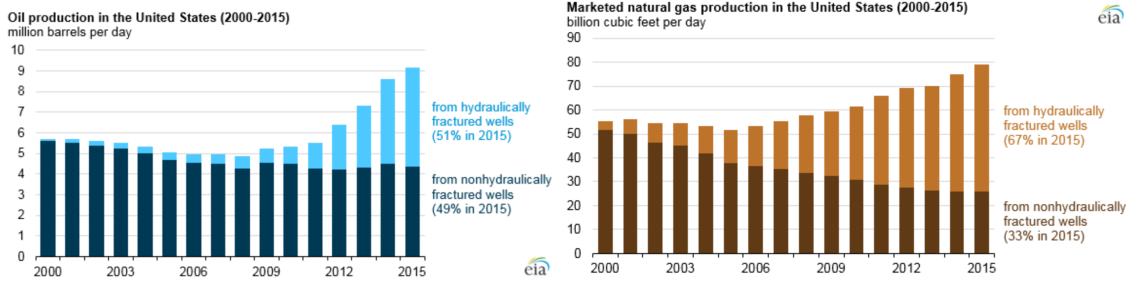


**FIGURE 1.1.** These plots show the evolution of fracking, leading to it becoming the main source of oil and gas in the United States. The numbers shown in the graphs are behind the actual values mentioned in the text because the charts were last updated in 2015. Courtesy from the US Energy Information Administration.

suitable hot rock formations, which limits the productivity of these systems in their natural state. By employing hydraulic fracturing techniques, the permeability, and consequently the efficiency of geothermal systems can be improved. These specially treated systems are commonly referred to as Enhanced Geothermal Systems (EGS). Advances in fracking science and technology are thus one of the key steps towards making EGS a viable and reliable clean energy source. The process is depicted in Figure 1.2.

Another significant geological process that addresses the global CO<sub>2</sub> problem is Carbon Storage and Sequestration, where CO<sub>2</sub> is injected and trapped in tight rock formations deep beneath the surface, preventing its release into the atmosphere. In the context of CO<sub>2</sub> sequestration, caprock fracturing, which can happen during injection or through long-term thermo-chemo-mechanical processes may lead to CO<sub>2</sub> leakage.[8] This consists thus of case where, in contrast of the previous ones, hydraulic fracture must be prevented.

One can also find applications in various other fields, including the disposal of waste drill cuttings underground [9], measurement of in situ stresses [10, 11], goafing and fault reactivation in mining operations [12, 13], and stimulation of groundwater wells [14, 15].

Despite its significant economic benefits, the process has raised concerns among critics regarding potential seismic events, especially in the context of O&G and EGS applications. Additional objections center around the environmental impact, including air and noise pollution, as well as the risk of groundwater and surface water contamination when chemicals are mixed with the injection fluids.

Given the importance of these applications and the associated risks, it is evident that a comprehensive understanding of fracture processes is crucial for the well-being of our planet and society. However, obtaining sufficient experimental data for deep subsurface processes is challenging due to the depths involved and the difficulty in replicating true rock conditions in laboratory experiments. Consequently, there has been a growing focus on computational modeling and simulation of fluid-driven fracture. These computational approaches provide a cost-effective means to gain insights into the intricate physical processes associated with hydraulic fracturing.

## 1.2 Background

Any mathematical model that tries to represent the hydraulic fracturing phenomena has to account for at least three different processes. The deformation of the rock, the fluid flow and the fracture propagation [3]. These three processes are strongly coupled, which makes the derivation of analytical solutions very complicated, and only possible when the fracture has a predefined shape. Some examples of that are

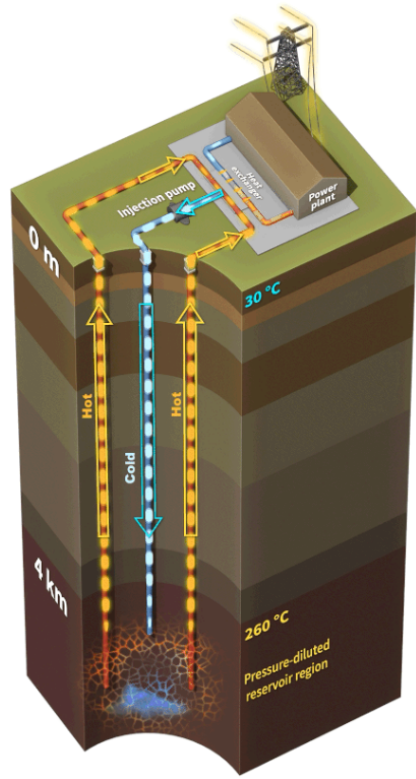


FIGURE 1.2. Simplified depiction of an EGS system. Courtesy of Los Alamos National Laboratory.

the PKN model [16, 17, 18] and the KGD model [19, 20], developed in the early days of the hydraulic fracturing technology. Although limited by restrictive assumptions, they were extremely useful at that time, providing engineers with good estimations of treatment parameters.

The topic of analytical approaches is still an ongoing area of research with significant progress being made in the past decades, specifically in understanding propagation regimes, near-tip processes, and scaling laws. Extensive research has yielded valuable insights. For instance, near-tip solutions for zero-toughness, impermeable fractures were derived using asymptotic theory in [21], and the analysis was extended to leak-off dominated cases in [22]. Subsequent studies have incorporated additional factors, such as finite toughness and fluid-lag [23, 24, 25]. Moreover, similar techniques have been applied to identify the dimensionless groups that govern the key characteristics of the solutions, enabling the categorization of main regimes (leak-off, toughness, or viscosity dominated) within the parameter space. This parameter space includes rock properties like elastic moduli, toughness, and leak-off coefficient, as well as treatment characteristics such as fluid viscosity and injection rate [26, 27, 28, 29, 30].

Although these analytical methods provide valuable insight into the physics and allow for useful back of the envelope calculations, they can not be used to simulate most of the practical fracking treatments due to their restrictive assumptions regarding fracture geometry and homogenous material properties. They also are not able to capture other important phenomena that affect hydraulic fracturing, such as the presence of confining (*in situ*) stresses, pre-existing (natural) fractures, propellant transport and etc. All these issues have been demonstrated by experiments to affect the fracture propagation and therefore, motivated the development of more widely applicable computational approaches that aim to obtain approximations to the solutions of fluid-driven fracture models in their general form.

These approaches range from production-level reservoir modeling tools such as ResFrac[31, 32], Xsite[33], Kinetix[34, 35] (check [36] for an extensive list) to open-source alternatives, such as GEOS[37, 38, 39], PyFrac[40] and others. Many of the models and associated codes assume fracture networks that remain planar, but in recent years strides have been made towards modeling cracks that evolve in arbitrary ways in response to fluid-driven loads. Some works in this direction include (i) Gupta and Duarte [41, 42] which used a higher-order generalized finite element method (GFEM) to discretize the fracture surface and compute accurate stress intensity factors(SIFs); (ii) Salimzadeh et al. [271, 272, 273] and Paluszny et al. [238] which used adaptive remeshing and a pure FEM based approach, in combination with the displacement correlation method to calculate the SIFs even in the presence of multiple interacting fractures and (iii) Tang et al. [43] and Li et al. [44, 45] where the boundary element method is combined with the displacement discontinuity approach to propagate fractures which are loosely coupled to the mechanical problem using EDFM[46]. However, in all these approaches, the computation of crack front advancements still relies on phenomenological relations between the computed SIFs and some type of crack front velocity. They also have limitations when dealing with merging cracks (for example, when a hydraulic fracture approaches a natural fracture), as the formulations do not account for the possibility of a propagating crack to arrest in these cases.

All these approaches can be grouped together in the broad category of sharp interface models, where the fracture surface is explicitly modelled. These tend to be particularly advantageous when the fracture configuration is relatively simple, but face the aforementioned challenges when complex geometric evolution is involved.

Some of these challenges tend to be alleviated with the use of diffuse crack models, such as the phase-field model for fracture [47, 48, 49]. These offer more flexibility for representing complex fracture evolution, and, in many cases, have propagation fully

governed by energetic principles, being, in some sense, a generalization of Griffiths' law [50]. On the other hand, they introduce other challenges such as the lack of a well-defined fracture surface and an increased computational expense[51].

The first attempts towards a phase-field model for hydraulic fracture began with extensions of the traditional phase-field model [47, 48] to pressurized cracks, as in Bourdin et al. [1] and Wheeler et al. [52]. Subsequently, fluid flow in the fractures, and also poromechanics were considered. Miehe et al. [53, 54] developed a thermodynamically consistent framework, from minimization principles, to couple poromechanics, fluid-flow and phase-field fracture. The flow problem was modeled via the Darcy's equation, containing a permeability coefficient that used the phase-field variable and the crack opening to mimic the cubic relationship from the lubrication theory in the crack region. Mikelic et al. [55, 56] developed a model that separated the domain into fracture and reservoir, by using the phase-field variable as an indicator function. They also considered the flow inside the fracture as a Darcy flow, but their model treated the fracture as a three-dimensional entity, which led to a different permeability tensor compared to [53, 54]. Yet another approach concerns the work of Wilson and Landis [57], who proposed a model that included fluid velocities as primary variables. This allowed for a more detailed description of the flow within the fracture, which was modeled by a Brinkman-type equation [58]. The phase-field parameter acted as an indicator of the flow regime, between Darcy flow (away from cracks) and Stokes flow (inside cracks). Finally, the recent work of Chukwudzie et al. [59] presented a different model, wherein the lubrication theory equations were included in the weak form by means of a  $\Gamma$ -convergent regularization. These various formulations exhibit real differences in terms of their structure, mainly due to the different forms of incorporating the pressure loads and extracting an aperture value over diffuse fracture surfaces. Therefore, comparative investigations such as [60] and [61] are still needed for a better understanding of the

strengths and weakness of these models.

The use of a phase-field to represent a fracture network in a diffuse manner certainly facilitates the representation of complex geometric evolution, including crack branching and merging. However, it also requires the use of meshes or grids that are capable of resolving the regularization length, making these approaches computationally expensive. One approach to improving the efficiency of the method is the use of adaptive mesh refinement, such as in [62, 63, 64, 65]. In the specific case of hydraulic fracturing, another challenge concerns the crack opening or aperture, a field that is tightly coupled with the fluid pressure within fractures. In a phase-field setting, due to the lack of an explicit crack surface, extracting the aperture or accounting for its effects requires additional considerations. All the aforementioned works present some way to account for the aperture within a diffuse setting, but the robustness of these approaches remains unclear [66].

Outside the context of hydraulic fracturing, some researchers in the phase-field community have developed “hybrid” approaches, wherein the phase-field formulation was combined with a sharp crack representation. The motivation for these approaches varies, from “cutting” the mesh to remove artificial traction transmission and circumvent element distortion [67] to reducing the overall computational cost [68, 69, 70]. In the work of Giovanardi et al.[68], phase-field subproblems in the vicinity of crack tips were used to propagate a global, discrete crack. The eXtended Finite Element Method (XFEM)[71] was used to place fracture discontinuities in the displacement field within the background global mesh. More recently, Muixi et al.[69] created an approach that uses the phase-field method only at the crack tips, and XFEM in the rest of the domain. In contrast to [68], there is no overlap of the representations in crack tip areas. In Li et al. [70], the shifted boundary method is employed to represent the discrete fracture without mesh cutting techniques. This method preserves mesh independence of the crack path, which is governed by a

phase-field subproblem near the fracture process zones. This subproblem is blended to global one similarly to [68]. Interestingly, the authors are able to take advantage of the phase-field approach to solve problems involving crack branching and merging in 2D.

The success of these hybrid approaches for purely mechanical cases opens the door for their extension to hydraulic fracturing. Such approaches are appealing because in principle they can circumvent the need for a complicated reconstruction of the crack opening from the phase-field. This area began to gain traction in the past few years. In Sun et al. [72] the authors developed a Finite Element-Meshfree method to represent the crack surfaces in a discrete fashion. The computed displacement field was used to obtain a driving force which was employed within the phase-field equation. This approach eliminated the need for the reconstruction of crack openings from the diffuse crack representation, but it also largely decoupled the phase field from the equations governing the force balance and did not address the computational expense associated with the fine discretization needed to represent the phase-field. More recently, Burbulla et al. [73] devised a similar hybrid algorithm, with improved coupling between the damage and displacement fields, but they also did not attempt to circumvent the elevated computational cost incurred by the phase-field approach. That was only investigated by [74], where the phase-field problem is restricted to a small portion of the domain, with the goal of reducing the overall problem size. In their work, only two-dimensional problems are studied.

### 1.3 Research contributions

This dissertation revisits the computational modeling of hydraulic fracturing with emphasis in the phase-field approach and proposes a new hybrid scheme that overcomes the two main limitations of pure phase-field formulations. Namely, the computation of the fracture aperture and the expensive computational cost. On a different

take, this new scheme, when compared to standard discrete fracture models, removes the need for a phenomenological criterion for crack propagation by relying on the minimization of an energy functional to drive fracture growth. Fundamental modeling aspects, related to the phase-field description of fluid-driven fracture are also discussed. The main contributions of each chapter are summarized below.

- In Chapter 2, we present a new phase-field formulation for including crack-face pressure loads and discuss how this formulation can be achieved by modifying the trial space in the traditional variational principle or by introducing a new functional dependent on the rates of the primary variables. The key differences between the new formulation and existing models for pressurized cracks in a phase-field setting are emphasized. Model-based simulations developed with discretized versions of the new formulation and existing models are then used to illustrate the advantages and differences. In order to analyze the results, a domain form of the J-Integral is developed for diffuse cracks subjected to pressure loads.
- In Chapter 3, we propose a multi-resolution approach for constructing model-based simulations of fluid-driven fracture. The approach consists of a hybrid scheme that couples a discrete crack representation in a global domain to a phase-field representation in a local subdomain near the crack tip. The multi-resolution approach addresses issues such as the computational expense of accurate hydraulic fracture simulations and the difficulties associated with reconstructing crack apertures from diffuse fracture representations. The efficacy of the method is illustrated through various benchmark problems in hydraulic fracturing, as well as a new study of fluid-driven crack growth around a stiff inclusion.
- In Chapter 4, we present an extension of the multi-resolution approach to

three dimensions, which involves a modification to the propagation scheme used in Chapter 3. First the extension to planar cracks in 3D is explored. The new algorithm is detailed and an efficient implementation in the HPC solver GEOS is developed. Some preliminary results are presented, involving multiple cracks are presented. Finally, the extension to non-planar fracture geometries is discussed. An algorithm with further modifications is presented. A simplified version of it is implemented and tested for a very simple. Further steps are discussed, building on the main limitations observed.

# 2

## Revisiting the Pressure Loading of Phase-Field Fractures<sup>1</sup>

### 2.1 Introduction

In this Chapter, a new formulation for the study of pressurized fractures, first proposed in the thesis of Hu [76] is examined. In particular, it is studied in combination with a cohesive version of the phase-field for fracture method, which was proposed in the recent works of [77, 78, 79]. This facilitates the study of pressurized fracture in quasi-brittle materials and reduces the sensitivity of the effective strength to the regularization length. To ensure that the cohesive fracture behavior is preserved, the implicit traction-separation law is evaluated for a simple one-dimensional problem and shown to be insensitive to the applied pressure with the new formulation. Fracture initiation and propagation examples are also examined to highlight advantages and limitations of the model, which is compared to other formulations for treating pressure-loaded fractures. This comparison also aids in understanding the implications of different modeling choices that have been widely used in the literature [1, 52, 80, 81, 82].

---

<sup>1</sup> This chapter's content is derived from Costa *et al.*[75]

As part of the analysis conducted to evaluate the various formulations, the J-Integral is used to verify the extent to which mode-I crack propagation occurs when the energy release rate reaches the critical fracture energy. The contour form of the J-Integral and its modifications for some common cases of phase-field fracture has been examined by others, see e.g. the work of [83], [84] and [85]. In the case of pressurized cracks, the contour version of the J-Integral is not path independent. Many prior works have focused on developing domain forms of the J-Integral for sharp cracks that are domain independent [86, 87]. In this work, a domain form of the J-Integral that is suitable for pressurized phase-field cracks is developed for the first time.

The Chapter is organized as follows. In Section 2.2, a simple model for pressure-induced fracturing is presented and the new phase-field formulation is derived in two different ways. Section 2.3 provides the derivation of the domain form of the J-Integral for pressurized phase-field cracks. In Section 2.4, the discretization scheme using finite elements is presented. Then, in Section 2.5 some fundamental examples involving crack nucleation and propagation are used to illustrate the performance of the various models and choices of indicator functions.

## 2.2 Model

The formulation for treating pressurized cracks in a phase-field setting, first introduced by Hu [76], can be derived in two different ways. In what follows, it is first derived based on energy minimization in quasi-static conditions in subsection 2.2.1. This illustrates the main difference in the underlying hypothesis for this new model compared to the widely used formulations of [1] and [80], for example. A second derivation based on a maximum dissipation principle is then provided in subsection 2.2.2.

The following assumptions are invoked for both derivations. A linear elastic body

$\Omega \in \mathbb{R}^n$  ( $n = 2$  or  $3$ ), containing cracks denoted by  $\Gamma$  is considered (Figure 2.1). The boundary  $\partial\Omega$  is partitioned as  $\partial\Omega = \partial\Omega_D \cup \partial\Omega_N$ , where  $\partial\Omega_D$  represents the portion of the boundary where displacements are prescribed and  $\partial\Omega_N$  the portion where tractions are applied. Deformations and rotations are assumed to be small, so that a small-strain formulation is appropriate. For simplicity, body forces are neglected.

### 2.2.1 Quasi-static derivation

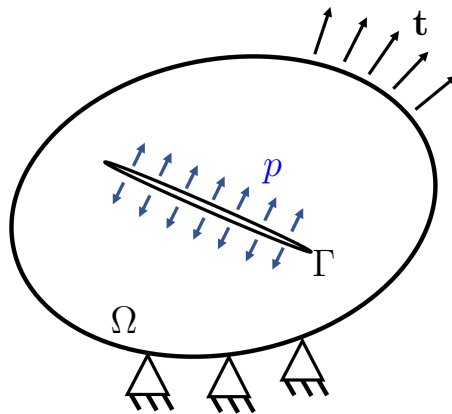


FIGURE 2.1. Generic body containing cracks loaded in pressure.

The quasi-static derivation of the formulation begins by considering the potential energy of a body with cracks which are internally loaded with a pressure  $p$ . Crack propagation is associated with a critical fracture energy density,  $G_c$ . The total potential energy is given by

$$U(\boldsymbol{\epsilon}(\mathbf{u})) = \int_{\Omega} \psi_e(\boldsymbol{\epsilon}(\mathbf{u})) \, dV + \int_{\Gamma} G_c \, dA - \int_{\Gamma} p \mathbf{n} \cdot \mathbf{u} \, dA - \int_{\partial\Omega_N} \mathbf{t} \cdot \mathbf{u} \, dA, \quad (2.1)$$

in which  $\mathbf{u}$  are the displacements,  $\boldsymbol{\epsilon}(\mathbf{u}) = \nabla^s \mathbf{u}$  denotes the infinitesimal strain,  $\psi_e$  the strain energy density,  $\mathbf{t}$  the externally applied tractions and  $\mathbf{n}$  the unit normals of the crack set  $\Gamma$  (oriented outwards from  $\Omega$ ).

In a phase-field for fracture setting, the crack surface  $\Gamma$  is regularized with the aid of a scalar phase (or damage) field  $d(\mathbf{x}) \in [0, 1]$ . In this work,  $d = 0$  represents intact

material (away from the crack surface) and  $d = 1$  fully-damaged material (inside the crack). The damage field is employed in the approximation of the surface integrals in (2.1) as volume integrals. For the energy associated with fracture, several common formulations are encapsulated by the approximation

$$\int_{\Gamma} G_c dA \approx \int_{\Omega} \frac{G_c}{c_0 \ell} \left( \alpha(d) + \ell^2 \nabla d \cdot \nabla d \right) dV, \quad (2.2)$$

where  $\alpha(d)$  denotes a local dissipation term,  $\ell$  is the regularization length, and  $c_0$  is a normalization constant given by  $c_0 = 4 \int_0^1 \sqrt{\alpha(s)} ds$ .

Such a regularization implies that the distinct crack surface  $\Gamma$  is no longer defined. As such, the second integral on the right of (2.1) also needs to be approximated as a volume integral in some manner. This is effected with the use of an indicator function  $I(d)$ . The surface integral involving the pressure is then approximated as

$$\int_{\Gamma} p \mathbf{n} \cdot \mathbf{u} dA \approx \int_{\Omega} p \left( -\frac{\nabla d}{\|\nabla d\|} \right) \cdot \mathbf{u} \|\nabla I(d)\| dV. \quad (2.3)$$

Note that the crack surface normal  $\mathbf{n}$  is approximated as  $-\nabla d / \|\nabla d\|$ , whereas the differential surface element  $dA$  becomes  $\|\nabla I\| dV$ . The indicator function must satisfy  $I(0) = 0$ ,  $I(1) = 1$  and be monotonically increasing. In Bourdin et al. [1],  $I(d) = d$  was firstly proposed. Wheeler et al. [52] provide a derivation that avoids an explicit approximation of the normal, such as (2.3), but is in fact equivalent to using the indicator function  $I(d) = 2d - d^2$ . In Peco et al. [81] and Jiang et al. [82],  $I(d) = d^2$  is used, with the motivation that  $I'(0) = 0$  is required to avoid the effects of pressure in undamaged areas.

Combining the approximation in (2.3) with the traditional phase-field approximation of fracture based on the Ambrosio-Tortorelli functional [48] and applying the

chain rule, the regularized counterpart of (2.1) is given by

$$\begin{aligned} U(\boldsymbol{\epsilon}, d) = & \int_{\Omega} \psi_e(\boldsymbol{\epsilon}, d) \, dV + \int_{\Omega} p \nabla d \cdot \mathbf{u} \, I'(d) \, dV \\ & + \int_{\Omega} \frac{G_c}{c_0 \ell} \left( \alpha(d) + \ell^2 \nabla d \cdot \nabla d \right) \, dV - \int_{\partial\Omega_N} \mathbf{t} \cdot \mathbf{u} \, dA, \end{aligned} \quad (2.4)$$

where the explicit dependence of the strain on the displacements has been dropped.

Often, the strain energy density is split and part of it is degraded with the damage, i.e.

$$\psi_e(\boldsymbol{\epsilon}(\mathbf{u}), d) = g(d) \psi_e^+(\boldsymbol{\epsilon}(\mathbf{u})) + \psi_e^-(\boldsymbol{\epsilon}(\mathbf{u})), \quad (2.5)$$

where  $g(d)$  denotes the degradation function, and  $\psi_e^+(\boldsymbol{\epsilon}(\mathbf{u}))$  and  $\psi_e^-(\boldsymbol{\epsilon}(\mathbf{u}))$  denote the “active” and “inactive” parts of the energy. The above form encapsulates most of the strain decompositions used in the literature [88],[89] to introduce asymmetry in the fracture behavior in tension and compression.

Typically, a minimization principle is applied to (2.4) to extract the governing equations for the displacements  $\mathbf{u}$  and the damage  $d$ . According to this principle, a pair  $(\mathbf{u}, d)$  is a valid state if and only if all neighboring states  $(\mathbf{u} + \delta\mathbf{u}, d + \delta d)$  have a greater potential energy. In the case of pressurized cracks, a subtle consideration leads to the formulation proposed herein. Consider the two scenarios indicated in Figure 2.2 where  $a$  denotes the crack length and  $da$  an infinitesimal crack increment. In the situation depicted in Figure 2.2b, the pressure load (applied in the areas colored in blue), is assumed to accompany any crack propagation. Therefore, in an energetic analysis, the virtual crack extension  $da$  is assumed pressurized. By contrast, in Figure 2.2a, the pressure load is assumed to remain confined to the original crack geometry during propagation. As a result, the virtual crack extension  $da$  is not subject to any surface load.

In terms of the resulting formulation, the difference between the two scenarios

shown in Figure 2.2 translate into the question of whether or not the damage variation  $\delta d$  should enter the pressure work contribution (2.3).

For the family of formulations that derived from [1] and [52], the scenario depicted in Figure 2.2b is assumed as a consequence of including the damage variation  $\delta d$  in (2.3). The proposed model in this work, by contrast, assumes the case indicated by Figure 2.2a. While in a discrete crack model these competing views may lead to the same energy release rate when taking the limit  $da \rightarrow 0$ , their phase-field regularizations give rise to different sets of governing equations. As demonstrated in the numerical examples in Section 5, this can translate into significant differences in the results from model-based simulations.

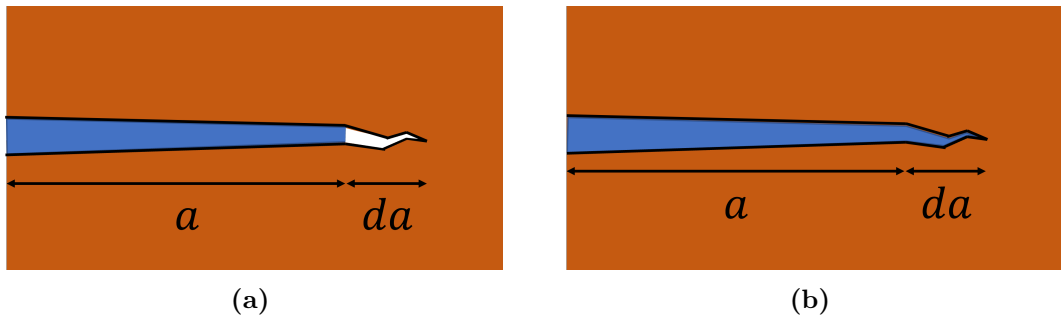


FIGURE 2.2. (a) Unloaded virtual crack. (b) Pressure loaded virtual crack;

In what follows, the formulation associated with Figure 2.2a will be referred to as the Unloaded Virtual Crack formulation, or UVC for short. In the UVC, the variation of the pressure work is simply<sup>2</sup>,

---

<sup>2</sup> On the other hand, if the assumption of Figure 2.2b is chosen, as in [1], two additional terms have to be accounted for,

$$\delta \left( \int_{\Omega} p \nabla d \cdot \mathbf{u} I'(d) dV \right) = \int_{\Omega} p \nabla d \cdot \delta \mathbf{u} I'(d) dV + \underbrace{\int_{\Omega} p \nabla \delta d \cdot \mathbf{u} I'(d) dV}_{\text{additional terms}} + \int_{\Omega} p \nabla d \cdot \mathbf{u} \delta d I''(d) dV.$$

$$\delta \left( \int_{\Omega} p \nabla d \cdot \mathbf{u} I'(d) dV \right) = \int_{\Omega} p \nabla d \cdot \delta \mathbf{u} I'(d) dV. \quad (2.6)$$

The variation of the potential energy  $\delta U$  can then be written as,

$$\begin{aligned} \delta U(\boldsymbol{\epsilon}, d) &= \int_{\Omega} \frac{\partial \psi_e}{\partial \boldsymbol{\epsilon}} : \delta \boldsymbol{\epsilon} dV + \int_{\Omega} p \nabla d \cdot \delta \mathbf{u} I'(d) dV - \int_{\partial \Omega_N} \mathbf{t} \cdot \delta \mathbf{u} dA \\ &\quad + \int_{\Omega} g'(d) \psi_e^+(\boldsymbol{\epsilon}) \delta d dV + \int_{\Omega} \frac{G_c}{c_0 \ell} \left( \alpha'(d) \delta d + 2\ell^2 \nabla d \cdot \nabla \delta d \right) dV, \end{aligned} \quad (2.7)$$

and, with the help of the divergence theorem,

$$\begin{aligned} \delta U(\boldsymbol{\epsilon}, d) &= \int_{\Omega} \left( -\nabla \cdot \frac{\partial \psi_e}{\partial \boldsymbol{\epsilon}} + p I'(d) \nabla d \right) \cdot \delta \mathbf{u} dV \\ &\quad + \int_{\Omega} \left( g'(d) \psi_e^+(\boldsymbol{\epsilon}) + \frac{G_c}{c_0 \ell} \alpha'(d) - \nabla \cdot \frac{2G_c \ell}{c_0} \nabla d \right) \delta d dV \\ &\quad + \int_{\partial \Omega_N} \left( \frac{\partial \psi_e}{\partial \boldsymbol{\epsilon}} \cdot \mathbf{n} - \mathbf{t} \right) \cdot \delta \mathbf{u} dA + \int_{\partial \Omega} \frac{2G_c \ell}{c_0} (\mathbf{n} \cdot \nabla d) \delta d dA. \end{aligned} \quad (2.8)$$

The local minimization principle requires the variation of the potential energy  $\delta U$  to be non-negative for any admissible state  $\mathbf{u}, d$ . In other words,  $\delta U(\boldsymbol{\epsilon}, d) \geq 0$ , giving rise to the following equation and boundary condition for  $\mathbf{u}$ , since the variation of the displacement field  $\delta \mathbf{u}$  is arbitrary:

$$-\nabla \cdot \boldsymbol{\sigma} + p I'(d) \nabla d = \mathbf{0} \text{ in } \Omega, \quad (2.9)$$

$$\boldsymbol{\sigma} \cdot \mathbf{n} - \mathbf{t} = \mathbf{0} \text{ in } \partial \Omega_N. \quad (2.10)$$

In the above,  $\boldsymbol{\sigma}$  denotes the Cauchy stress, defined as  $\boldsymbol{\sigma} = \frac{\partial \psi_e}{\partial \boldsymbol{\epsilon}}$ .

For the damage variable, it is assumed that the process is irreversible, such that  $\dot{d} \geq 0$ . As such, only positive variations in the damage are admissible, and  $\delta U(\boldsymbol{\epsilon}, d) \geq 0$  implies

$$g'(d)\psi_e^+(\boldsymbol{\epsilon}) + \frac{G_c}{c_0\ell}\alpha'(d) - \nabla \cdot \frac{2G_c\ell}{c_0}\nabla d \geq 0 \text{ in } \Omega, \quad (2.11)$$

$$\frac{2G_c\ell}{c_0}\mathbf{n} \cdot \nabla d \geq 0 \text{ on } \partial\Omega. \quad (2.12)$$

Equations (2.11) and (2.12) are identical to those in the standard phase-field model for traction-free cracks. This is the main difference between the new formulation and existing ones derived from deriving from [1] and [52], in which the governing equation for the damage field contains additional terms to account for the pressure loads on the virtual cracks. In what follows, we refer to that as the Loaded Virtual Crack formulation, or LVC. In the boxes below, the governing equations for the UVC are compared to those of the LVC.

#### Unloaded Virtual Crack Formulation (UVC)

$$-\nabla \cdot \boldsymbol{\sigma} + pI'(d)\nabla d = \mathbf{0} \text{ in } \Omega, \quad (2.13)$$

$$\boldsymbol{\sigma} \cdot \mathbf{n} - \mathbf{t} = \mathbf{0} \text{ in } \partial\Omega_N. \quad (2.14)$$

$$g'(d)\psi_e^+(\boldsymbol{\epsilon}) + \frac{G_c}{c_0\ell}\alpha'(d) - \nabla \cdot \frac{2G_c\ell}{c_0}\nabla d \geq 0 \text{ in } \Omega, \quad (2.15)$$

$$\frac{2G_c\ell}{c_0}\mathbf{n} \cdot \nabla d \geq 0 \text{ on } \partial\Omega. \quad (2.16)$$

## Loaded Virtual Crack Formulation

(LVC)

$$-\nabla \cdot \boldsymbol{\sigma} + pI'(d)\nabla d = \mathbf{0} \text{ in } \Omega, \quad (2.17)$$

$$\boldsymbol{\sigma} \cdot \mathbf{n} - \mathbf{t} = \mathbf{0} \text{ in } \partial\Omega_N. \quad (2.18)$$

$$\begin{aligned} g'(d)\psi_e^+(\boldsymbol{\epsilon}) + \frac{G_c}{c_0\ell}\alpha'(d) - \nabla \cdot \frac{2G_c\ell}{c_0}\nabla d \\ - \nabla \cdot [p\mathbf{u} I'(d)] + p\nabla d \cdot \mathbf{u} I''(d) \geq 0 \text{ in } \Omega, \end{aligned} \quad (2.19)$$

$$\mathbf{n} \cdot \left( \frac{2G_c\ell}{c_0}\nabla d + pI'(d)\mathbf{u} \right) \geq 0 \text{ on } \partial\Omega. \quad (2.20)$$

It is readily apparent that the governing equations for the displacements are identical in the UVC and the LVC. The main difference is in the absence of the additional pressure-dependent terms in the evolution for the damage field and the accompanying boundary condition.

In Appendix A, an analytical study of the energy release rate of a crack propagating under an arbitrary pressure load  $p(x)$  is provided, under the assumptions of the UVC formulation and linear elastic fracture mechanics. The results of the study show that it is possible to recover the classic relationship between the energy release rate and the stress intensity factor with the UVC formulation. This ensures the consistency of the proposed formulation (UVC) with many theoretical works [90, 25, 26, 30, 91] in the field of hydraulic fracture, where the stress intensity factor is used as the propagation criterion.

### 2.2.2 Derivation using the maximum dissipation principle

In this subsection, an alternative approach to derive the (UVC) formulation is presented. It is based on the construction of a total potential functional which depends on the rates of the internal variables  $\dot{\boldsymbol{\epsilon}}, \dot{d}$  and accounts for the work of the pressure

load as an external dissipation mechanism. This approach is described in more detail in [92] and [76], where it is used to derive a variationally consistent phase-field model for ductile fracture.

The total potential is postulated as,

$$L(\dot{\epsilon}, \dot{d}) = \int_{\Omega} \dot{u}(\dot{\epsilon}, \dot{d}) dV - \mathcal{P}^{ext}, \quad (2.21)$$

where  $u$  is the material internal energy, which relates to the Helmholtz free-energy  $\psi$  through  $\dot{u} = \dot{\psi} + \dot{T}s$ , where  $T$  is the temperature and  $s$  the entropy. In this work, only isothermal processes are considered, therefore,  $\dot{u} = \dot{\psi}$ . The term  $\mathcal{P}^{ext}$  denotes the external power expenditure. If cracks were represented by internal boundaries  $\Gamma$  instead of a damage field, one could write,

$$\mathcal{P}^{ext} = \int_{\partial\Omega \cup \Gamma} \mathbf{t} \cdot \dot{\mathbf{u}} dA = \int_{\partial\Omega} \mathbf{t} \cdot \dot{\mathbf{u}} dA + \int_{\Gamma} p \mathbf{n} \cdot \dot{\mathbf{u}} dA. \quad (2.22)$$

However, in a regularized setting this integral over  $\Gamma$  is once again transformed into a volume integral over  $\Omega$ , as in (2.3),

$$\int_{\Gamma} p \mathbf{n} \cdot \dot{\mathbf{u}} dA \approx \int_{\Omega} p \left( -\frac{\nabla d}{\|\nabla d\|} \right) \cdot \dot{\mathbf{u}} \|\nabla I(d)\| dV = - \int_{\Omega} p \nabla d \cdot \dot{\mathbf{u}} I'(d) dV. \quad (2.23)$$

Recalling the equivalence between the internal energy and the Helmholtz free-energy, the Coleman-Noll procedure can be applied and, in combination with (2.22) and (2.23), leads to the following expression for  $L$  as a function of  $\psi$ :

$$L(\dot{\epsilon}, \dot{d}) = \int_{\Omega} \left( \frac{\partial \psi}{\partial \epsilon} : \dot{\epsilon} + \frac{\partial \psi}{\partial d} \dot{d} + \frac{\partial \psi}{\partial \nabla d} \cdot \nabla \dot{d} + p \nabla d \cdot \dot{\mathbf{u}} I'(d) \right) dV - \int_{\partial\Omega} \mathbf{t} \cdot \dot{\mathbf{u}} dA. \quad (2.24)$$

The evolution process is postulated to follow the minimizers of this total potential, with the supplemental conditions that damage is an irreversible process and that the displacements  $\mathbf{u}$  are prescribed over a subset  $\partial\Omega_D$  of the boundary. In other words,

$$\dot{\boldsymbol{\epsilon}}, \dot{d} = \underset{\dot{\boldsymbol{\epsilon}}, \dot{d}}{\operatorname{argmin}} L(\dot{\boldsymbol{\epsilon}}, \dot{d}), \text{ subject to } \dot{d} \geq 0 \text{ and } \mathbf{u} = \mathbf{g} \text{ on } \partial\Omega_D. \quad (2.25)$$

Using the Euler-Lagrange equations, the following general evolution equations can then be obtained in terms of the free-energy function  $\psi$ :

$$\nabla \cdot \frac{\partial \psi}{\partial \boldsymbol{\epsilon}} - pI'(d)\nabla d = \mathbf{0} \text{ in } \Omega, \quad (2.26)$$

$$\nabla \cdot \frac{\partial \psi}{\partial \nabla d} - \frac{\partial \psi}{\partial d} \geq \mathbf{0} \text{ in } \Omega, \quad (2.27)$$

with the boundary conditions

$$\frac{\partial \psi}{\partial \boldsymbol{\epsilon}} \cdot \mathbf{n} - \mathbf{t} = \mathbf{0} \text{ on } \partial\Omega \setminus \partial\Omega_D \quad (2.28)$$

$$\mathbf{n} \cdot \frac{\partial \psi}{\partial \nabla d} \geq 0 \text{ on } \partial\Omega. \quad (2.29)$$

To be consistent with the derivation in subsection 2.2.1, the Helmholtz free-energy is postulated as,

$$\psi(\boldsymbol{\epsilon}, d) = \psi_e(\boldsymbol{\epsilon}, d) + \frac{G_c}{c_0 \ell} \left( \alpha(d) + \ell^2 \nabla d \cdot \nabla d \right), \quad (2.30)$$

following the regularization based on the Ambrosio-Tortorelli functional. In this case, the general equations (2.26)-(2.29) take the form

$$-\nabla \cdot \boldsymbol{\sigma} + pI'(d)\nabla d = \mathbf{0} \text{ in } \Omega, \quad (2.31)$$

$$g'(d)\psi_e^+(\boldsymbol{\epsilon}) + \frac{G_c}{c_0\ell}\alpha'(d) - \nabla \cdot \frac{2G_c\ell}{c_0}\nabla d \geq 0 \text{ in } \Omega, \quad (2.32)$$

with the boundary conditions

$$\boldsymbol{\sigma} \cdot \mathbf{n} - \mathbf{t} = \mathbf{0} \text{ on } \partial\Omega_N, \quad (2.33)$$

$$\mathbf{n} \cdot \nabla d \geq 0 \text{ on } \partial\Omega. \quad (2.34)$$

By inspection, (2.31)-(2.34) are identical to (2.9)-(2.12).

### 2.2.3 Constitutive choices of the phase-field formulation

In the previous subsection, the proposed model for pressurized cracks was developed for a general phase-field regularization of the variational approach to fracture [47], with a free-energy of the form

$$\psi(\boldsymbol{\epsilon}, d) = \underbrace{g(d)\psi_e^+(\boldsymbol{\epsilon}) + \psi_e^-(\boldsymbol{\epsilon})}_{\psi_e} + \underbrace{\frac{G_c}{c_0\ell}\left(\alpha(d) + \ell^2\nabla d \cdot \nabla d\right)}_{\psi_f}. \quad (2.35)$$

where  $\psi_f$  is used to indicate the part of the free-energy associated with fracture.

In what follows, the constitutive choices used in the example problems provided in Section 2.5 are described.

#### 2.2.3.1 Elastic energy and decomposition

First, in terms of the solid bulk response, an elastic energy of the type (2.5) is assumed. When the material is undamaged, it reduces to a purely linear elastic energy, that is,

$$\psi_e(\boldsymbol{\epsilon}(\mathbf{u}), 0) = \psi_e^+(\boldsymbol{\epsilon}(\mathbf{u}), 0) + \psi_e^-(\boldsymbol{\epsilon}(\mathbf{u}), 0) = \frac{1}{2}\boldsymbol{\epsilon}(\mathbf{u}) : \mathbb{C} : \boldsymbol{\epsilon}(\mathbf{u}), \quad (2.36)$$

where  $\mathbb{C}$  is the elasticity tensor.

When damage is present, a decomposition of the energy is often assumed. In many cases, when the applied load to a fracturing body is predominately tensile, the “no-split” case given by,

$$\psi_e^-(\boldsymbol{\epsilon}(\mathbf{u}), d) = 0 \rightarrow \psi_e(\boldsymbol{\epsilon}(\mathbf{u}), d) = \frac{1}{2}g(d)\boldsymbol{\epsilon}(\mathbf{u}) : \mathbb{C} : \boldsymbol{\epsilon}(\mathbf{u}), \quad (2.37)$$

is capable of correctly predicting the material response, while leading to a simpler set of governing equations. However, in a wide range of scenarios, compressive forces are present, and an energy split is needed to prevent crack formation in zones of high compression, as well as to allow for transmission of compressive forces across fractured faces.

In Section 2.5, one of the example problems will employ the spectral split of Miehe et al. [89], given by,

$$\psi_e^+(\boldsymbol{\epsilon}(\mathbf{u}), d) = \frac{1}{2}\lambda \langle \text{Tr } \boldsymbol{\epsilon} \rangle_+^2 + \mu \boldsymbol{\epsilon}^+ : \boldsymbol{\epsilon}^+ \text{ and } \psi_e^-(\boldsymbol{\epsilon}(\mathbf{u}), d) = \frac{1}{2}\lambda \langle \text{Tr } \boldsymbol{\epsilon} \rangle_-^2 + \mu \boldsymbol{\epsilon}^- : \boldsymbol{\epsilon}^-. \quad (2.38)$$

Here,  $\langle \cdot \rangle_+$  and  $\langle \cdot \rangle_-$  denote the positive and negative parts of a number respectively, while  $\boldsymbol{\epsilon}^+$  and  $\boldsymbol{\epsilon}^-$  are the positive and negative parts of an additive decomposition of the strain tensor based on the signs of its eigenvalues. A more detailed description, including the derivation of the stiffness matrix in this case, is provided by Jiang et al. [93].

### 2.2.3.2 Brittle fracture

The first and more traditional phase-field model with an energy of the type (2.35) was proposed in [48]. It was developed to approximate the brittle fracture process of linear elastic materials in the limit of vanishing  $\ell$ . In its original form, the degradation

function

$$g(d) = \xi + (1 - \xi)(1 - d)^2, \quad (2.39)$$

is used in combination with a quadratic local dissipation  $\alpha(d) = d^2$ , in what is now called the AT-2 formulation. However, the use of,  $\alpha(d) = d$ , (widely referred as the AT-1) comes with the advantage of a purely elastic response before the onset of damage and a compactly supported damage field. Therefore, it will be employed in the example in Section 2.5 where brittle fracture is investigated. The parameter  $\xi$  in (2.39) is the residual stiffness, a very small numerical parameter that avoids the loss of ellipticity in fully damaged material.

#### 2.2.3.3 Cohesive fracture

The phase-field model for cohesive fracture was first proposed by Lorentz et al. [77, 94]. In this model, the use of a quasi-quadratic degradation function, given by

$$g(d) = \xi + (1 - \xi) \frac{(1 - d)^2}{(1 - d)^2 + md(1 + pd)}, \quad (2.40)$$

is combined with a linear local dissipation function  $\alpha(d) = d$ . The parameter  $m$  is defined as  $m = \frac{G_c}{c_0 \ell \psi_c}$ , where  $\psi_c$  is the nucleation energy, below which no damage is expected to form. The parameter  $p$  is a shape parameter that can be used to adjust the traction-separation response. In this work,  $p = 1$  is used.

## 2.3 A J-Integral for pressurized cracks in a phase-field setting

This Section presents a modified J-Integral, capable of retrieving the energy release rate, denoted here by  $G$  in the case of pressurized cracks in a phase-field for fracture setting. The resulting integral is then re-cast into a domain-independent form that is more amenable to finite-element calculations.

A common form of the J-Integral, derived for phase-field fracture and applicable to traction-free cracks is given by [83, 84]

$$J = \mathbf{r} \cdot \int_{\zeta} \left( \psi(\boldsymbol{\epsilon}, d) \mathbb{I} - \nabla \mathbf{u}^T \boldsymbol{\sigma} - \nabla d \otimes \boldsymbol{\omega} \right) \mathbf{n} ds, \quad (2.41)$$

where  $\psi(\boldsymbol{\epsilon}, d)$  is given by equation (2.35). In the above, the vector  $\mathbf{r}$  denotes the crack propagation direction,  $\zeta$  is a closed path around the crack tip,  $\mathbb{I}$  is the second-order identity tensor,  $\mathbf{n}$  is the normal to the closed path  $\zeta$  and  $\boldsymbol{\omega} = \partial \psi / \partial \nabla d = (G_c \ell / c_0) \nabla d$ . Compared to the original form of the J-Integral proposed by Rice [95, 96], this expression contains additional terms to account for the phase-field parameter  $d$ .

Importantly, Sicsic and Marigo [83] show that, under certain conditions, the standard form of the J-Integral widely employed for sharp cracks, viz.

$$J = \mathbf{r} \cdot \int_{\zeta} \left( \psi_e(\boldsymbol{\epsilon}, d) \mathbb{I} - \nabla \mathbf{u}^T \boldsymbol{\sigma} \right) \mathbf{n} ds, \quad (2.42)$$

can be used in a regularized phase-field setting. These conditions are:

**H1** : The regularization length is sufficiently small, so that a separation of scales between the solution in the damage band and the outer solution can be achieved;

**H2** : The path  $\zeta$  intersects the crack plane at a ninety-degree angle;

**H3** : The path  $\zeta$  intersects the crack plane sufficiently far from the crack tip, so that the damage field only varies in a direction perpendicular to the crack plane.

In what follows, these same conditions are assumed, as they facilitate a simpler derivation of a modified J-Integral capable of retrieving the energy release rate even

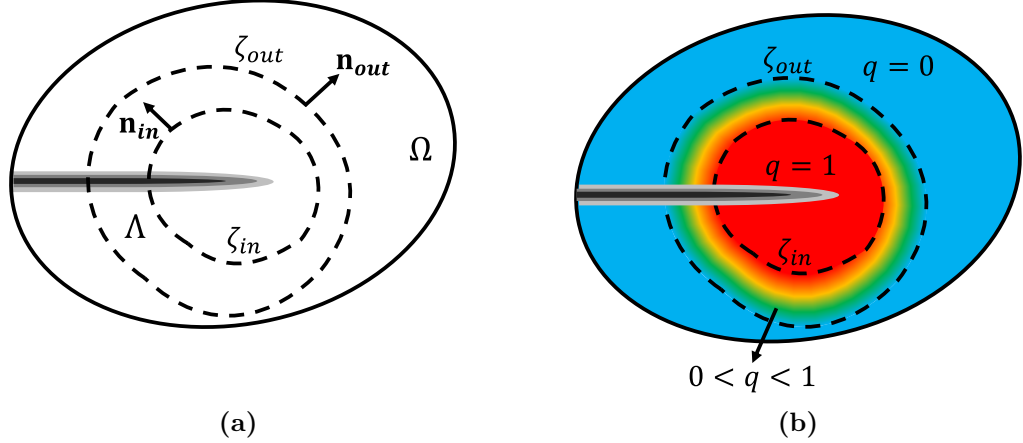


FIGURE 2.3. (a) The contour paths  $\zeta_{in}$  and  $\zeta_{out}$  and subdomain  $\Lambda$ , in the vicinity of a regularized crack.; (b) Color contour plot indicating the assumed variation in the function  $q$ .

in the presence of pressure loads on the crack faces. The main result of this section can then be stated in the following way.

**Claim:** Consider a domain  $\Omega \in \mathbb{R}^2$  with a straight phase-field crack and two closed, non-intersecting paths  $\zeta_{in}$  and  $\zeta_{out}$  around the crack tip, enclosing an area  $\Lambda$  as shown in Figure 2.3a. Let  $q(x)$  be a sufficiently smooth function satisfying  $q = 1$  on  $\zeta_{in}$  and  $q = 0$  on  $\zeta_{out}$ . Further, assume that  $q = 1$  for all points inside  $\zeta_{in}$  and  $q = 0$  for all points outside  $\zeta_{out}$ , as shown in Figure 2.3b. Finally, assume that the fracture is loaded by a constant pressure  $p$ , and that one of the formulations described in Section 2.2 holds. Then, if conditions **H1**, **H2** and **H3** hold for  $\zeta_{in}$  and  $\zeta_{out}$ , the energy release rate can be approximated by the integral

$$J = \mathbf{r} \cdot \int_{\Lambda} \left( \psi_e(\boldsymbol{\epsilon}, d)\mathbb{I} - p\nabla d \cdot \mathbf{u} I'(d)\mathbb{I} - \nabla \mathbf{u}^T \boldsymbol{\sigma} \right) \cdot \nabla q \, dA, \quad (2.43)$$

with an error that vanishes as  $\ell \rightarrow 0$ . The proof can be established in three steps, as detailed below.

**Proof:** Define  $\mathbf{T}_p = \psi_e(\boldsymbol{\epsilon}, d)\mathbb{I} - p\nabla d \cdot \mathbf{u} I'(d)\mathbb{I} - \nabla \mathbf{u}^T \boldsymbol{\sigma}$ . Using the divergence theorem,

one can show that

$$\int_{\Lambda} \nabla \cdot (q \mathbf{T}_p) dA = \int_{\zeta_{in} \cup \zeta_{out}} q \mathbf{T}_p \cdot \mathbf{n} ds = 0 - \int_{\zeta_{in}} \mathbf{T}_p \cdot \mathbf{n} ds, \quad (2.44)$$

because  $q$  vanishes on  $\zeta_{out}$  and the normal  $\mathbf{n}$  to  $\zeta_{in}$  points inward to  $\Lambda$ , as shown in Figure 2.3a. Multiplying both sides by the crack direction  $\mathbf{r}$  and applying the chain rule yields

$$-\mathbf{r} \cdot \int_{\Lambda} \left( \mathbf{T}_p \cdot \nabla q + q \nabla \cdot \mathbf{T}_p \right) dA = \mathbf{r} \cdot \int_{\zeta_{in}} \mathbf{T}_p \cdot \mathbf{n} ds, \quad (2.45)$$

which completes the first step of the proof.

The second step consists of showing that the term  $R = \mathbf{r} \cdot \int_{\Lambda} q \nabla \cdot \mathbf{T}_p dA$  is zero.

Expanding the expression for  $\mathbf{T}_p$  and using the chain rule yields

$$\begin{aligned} R &= \mathbf{r} \cdot \int_{\Lambda} q \nabla \cdot \left( \psi_e(\boldsymbol{\epsilon}, d) \mathbb{I} - p \nabla d \cdot \mathbf{u} I'(d) \mathbb{I} - \nabla \mathbf{u}^T \boldsymbol{\sigma} \right) dA \\ &= \int_{\Lambda} q \left( \frac{\partial \psi_e(\boldsymbol{\epsilon}, d)}{\partial \nabla^s \mathbf{u}} \cdot (\nabla (\nabla^s \mathbf{u}) \mathbf{r}) + \frac{\partial \psi_e(\boldsymbol{\epsilon}, d)}{\partial d} \nabla d \cdot \mathbf{r} - (\nabla \cdot \boldsymbol{\sigma}) \cdot (\nabla \mathbf{u} \mathbf{r}) \right. \\ &\quad \left. - \boldsymbol{\sigma} (\nabla (\nabla \mathbf{u}) \mathbf{r}) - p \nabla d \cdot (\nabla \mathbf{u} \mathbf{r}) I'(d) - p \mathbf{u} \nabla (I'(d) \nabla d) \mathbf{r} \right) dA. \end{aligned} \quad (2.46)$$

Re-arranging some terms, one can write,

$$\begin{aligned} R &= \int_{\Lambda} q \left[ \left( \frac{\partial \psi_e(\boldsymbol{\epsilon}, d)}{\partial \nabla^s \mathbf{u}} - \boldsymbol{\sigma} \right) \cdot (\nabla (\nabla^s \mathbf{u}) \mathbf{r}) - \left( \nabla \cdot \boldsymbol{\sigma} - p I'(d) \nabla d \right) \cdot (\nabla \mathbf{u} \mathbf{r}) \right. \\ &\quad \left. + \frac{\partial \psi_e(\boldsymbol{\epsilon}, d)}{\partial d} \nabla d \cdot \mathbf{r} - p \mathbf{u} \nabla (I'(d) \nabla d) \mathbf{r} \right] dA. \end{aligned} \quad (2.47)$$

For any elastic material, the definition of stress implies  $\frac{\partial \psi_e(\boldsymbol{\epsilon}, d)}{\partial \nabla^s \mathbf{u}} = \boldsymbol{\sigma}$ , and due to equation (2.26),  $\nabla \cdot \boldsymbol{\sigma} - p \nabla d = \mathbf{0}$ , so, the expression above reduces to

$$R = \int_{\Lambda} q \left( \frac{\partial \psi_e(\boldsymbol{\epsilon}, d)}{\partial d} \nabla d \cdot \mathbf{r} - p \mathbf{u} \nabla (I'(d) \nabla d) \mathbf{r} \right) dA. \quad (2.48)$$

Assuming a separation of scales, the domain  $\Lambda$  can be separated into two regions: (i)  $\Lambda_{band}$ , which consists of the intersection between  $\Lambda$  and the support of the damage field representing the crack and (ii)  $\Lambda_{outer}$ , which denotes the remainder of  $\Lambda$ , outside of the damage band. In the asymptotic limit as  $\ell \rightarrow 0$ , the material in  $\Lambda_{outer}$  behaves as purely elastic. Within  $\Lambda_{outer}$ , one has  $d \approx \nabla d \approx 0$ , and therefore,

$$R_{outer} = \int_{\Lambda_{outer}} q \left( \frac{\partial \psi_e(\boldsymbol{\epsilon}, d)}{\partial d} \nabla d \cdot \mathbf{r} - p \mathbf{u} \nabla(I'(d) \nabla d) \mathbf{r} \right) dA \approx 0. \quad (2.49)$$

For the  $\Lambda_{band}$  region, by condition **H3**,  $\nabla d$  is purely perpendicular to the crack direction, so,  $\nabla d \cdot \mathbf{r} \approx 0$ . Therefore,

$$R_{band} = \int_{\Lambda_{band}} q \left( \frac{\partial \psi_e(\boldsymbol{\epsilon}, d)}{\partial d} \nabla d \cdot \mathbf{r} - p \mathbf{u} \nabla(I'(d) \nabla d) \mathbf{r} \right) dA \approx 0. \quad (2.50)$$

Since  $\Lambda = \Lambda_{band} \cup \Lambda_{outer}$ , we must have

$$R = R_{outer} + R_{band} \approx 0. \quad (2.51)$$

This completes the second step.

The final step of the proof begins by invoking the separation of scales to decompose the contour integral in (2.45) via

$$\mathbf{r} \cdot \int_{\zeta_{in}} \mathbf{T}_p \cdot \mathbf{n} ds = \mathbf{r} \cdot \left( \int_{\zeta_{in}^{band}} \mathbf{T}_p \cdot \mathbf{n} ds + \int_{\zeta_{in}^{outer}} \mathbf{T}_p \cdot \mathbf{n} ds \right). \quad (2.52)$$

On the  $\zeta_{in}^{outer}$  portion of the path, damage effects can be neglected and the integral simplifies to the standard (sharp) J-Integral. In the case of a uniformly pressurized crack [97], this gives

$$\int_{\zeta_{in}^{outer}} \mathbf{T}_p \cdot \mathbf{n} ds = G - pw, \quad (2.53)$$

where  $w$  denotes the crack aperture at the intersection of the crack and the contour  $\zeta_{in}$ .

The other portion of the integral can be re-written as

$$\mathbf{r} \cdot \int_{\zeta_{in}^{band}} \mathbf{T}_p \cdot \mathbf{n} \, ds = \mathbf{r} \cdot \int_{-B}^B (\psi_e \mathbb{I} - \nabla \mathbf{u}^T \boldsymbol{\sigma}) \cdot \mathbf{n} dx - \mathbf{r} \cdot \int_{-B}^B p(\nabla d \cdot \mathbf{u} I'(d)) \cdot \mathbf{n} dx, \quad (2.54)$$

where  $B$  is the half-length of the damage band and condition **H2** is used to transform the integral over  $\zeta_{in}^{band}$  to a simple real integral from  $-B$  to  $B$ . Here, both  $\mathbf{r}$  and  $\mathbf{n}$  are unit vectors that point in opposite directions, and therefore,  $\mathbf{r} \cdot \mathbf{n} = -1$ , so,

$$\mathbf{r} \cdot \int_{\zeta_{in}^{band}} \mathbf{T}_p \cdot \mathbf{n} \, ds = \int_{-B}^B (\psi_e \mathbb{I} - \nabla \mathbf{u}^T \boldsymbol{\sigma}) dx + p \int_{-B}^B (\nabla d \cdot \mathbf{u} I'(d)) dx. \quad (2.55)$$

Following [1], the second integral on the right approaches the crack aperture  $w$  as the regularization length decreases, while the first integrand on the right is bounded [83], and therefore this term is  $O(B)$ , so,

$$\mathbf{r} \cdot \int_{\zeta_{in}^{band}} \mathbf{T}_p \cdot \mathbf{n} \, ds = O(B) + pw = O(\ell) + pw, \quad (2.56)$$

since the damage band half-length  $B$  scales with the regularization length  $\ell$ . One can now go back to (2.52), and substitute (2.53) and (2.56) to obtain,

$$\mathbf{r} \cdot \int_{\zeta_{in}} \mathbf{T}_p \cdot \mathbf{n} \, ds = G + pw - pw + O(\ell). \quad (2.57)$$

Finally, combining (2.45), (2.51) and (2.57), one obtains

$$-\mathbf{r} \cdot \int_{\Lambda} \mathbf{T}_p \cdot \nabla q \, dA = G + O(\ell), \quad (2.58)$$

which concludes the proof.

## 2.4 Finite Element Implementation

In this Section, the details of the finite element discretization used to obtain approximations to the solution of the proposed model (UVC) are described. For analogous equations for the model (LVC), the reader is referred to [82]. First, the strong form of the governing equations, derived from the general free-energy (2.35) using the KKT[98, 99] conditions is presented.

### Strong form

Linear momentum balance:

$$\nabla \cdot \boldsymbol{\sigma} - p \nabla d + \mathbf{b} = \mathbf{0}, \quad \forall x \in \Omega, \quad (2.59)$$

$$\boldsymbol{\sigma} = \frac{\partial \psi_e}{\partial \boldsymbol{\epsilon}}, \quad \forall x \in \Omega, \quad (2.60)$$

$$\boldsymbol{\sigma} \cdot \mathbf{n} = \mathbf{t}, \quad \partial_t \Omega, \quad (2.61)$$

$$\mathbf{u} = \mathbf{u}_g, \quad \partial_u \Omega, \quad (2.62)$$

Fracture evolution:

$$\dot{d} \left( \nabla \cdot \frac{2G_c \ell}{c_0} \nabla d - \frac{G_c}{c_0 \ell} \alpha'(d) - g'(d) \psi_e^+(\boldsymbol{\epsilon}) \right) = 0, \quad \forall x \in \Omega, \quad (2.63)$$

$$\nabla \cdot \frac{2G_c \ell}{c_0} \nabla d - \frac{G_c}{c_0 \ell} \alpha'(d) - g'(d) \psi_e^+(\boldsymbol{\epsilon}) \leq 0, \quad \forall x \in \Omega, \quad (2.64)$$

$$\dot{d} \geq 0, \quad \forall x \in \Omega, \quad (2.65)$$

$$\nabla d \cdot \mathbf{n} = 0, \quad \partial \Omega, \quad (2.66)$$

$$d(0, \mathbf{x}) = d_0, \quad \Omega. \quad (2.67)$$

For the derivation of an equivalent weak form, trial spaces for  $\mathbf{u}$  and  $d$  are first defined. Although the derivation is confined to quasi-static loadings, the spaces are indexed by a discrete load step parameter  $t$ . The trial spaces are given by

$$\mathcal{U}_t = \{\mathbf{u} \in \mathcal{H}^1(\Omega)^d \mid \mathbf{u} = \bar{\mathbf{u}}_t \text{ on } \partial_u \Omega\}, \quad (2.68)$$

$$\mathcal{D}_t = \{d \in \mathcal{H}^1(\Omega) \mid d_{t-1}(x) \leq d_t(x) \leq 1, \forall x \in \Omega\}, \quad (2.69)$$

and the accompanying weighting spaces  $\mathcal{V}$  and  $\mathcal{C}$  are

$$\mathcal{V} = \{\mathbf{w} \in \mathcal{H}^1(\Omega)^d \mid \mathbf{w} = \mathbf{0} \text{ on } \partial_u \Omega\}, \quad (2.70)$$

$$\mathcal{C} = \{c \in \mathcal{H}^1(\Omega) \mid c(x) \geq 0, \forall x \in \Omega\}. \quad (2.71)$$

The condition of monotonicity in the space  $\mathcal{D}_t$  is used to prevent damage healing and is the weak enforcement of the condition  $\dot{d} \geq 0$ , in a time discrete setting. Denoting the inner product in  $\mathcal{H}^1(\Omega)$  and  $\mathcal{H}^1(\Omega)^d$  by  $(\cdot, \cdot)$  and its restriction in the boundary by  $\langle \cdot, \cdot \rangle$ , the weak form of the problem can be written as

### Weak form

Find  $\mathbf{u} \in \mathcal{U}_t$  and  $d \in \mathcal{D}_t$ , such that  $\forall \mathbf{w} \in \mathcal{V}$  and  $\forall c \in \mathcal{C}$ ,

$$(\nabla \mathbf{w}, \boldsymbol{\sigma}) - (\mathbf{w}, p \nabla d) - (\mathbf{w}, \mathbf{b}) - \langle \mathbf{w}, \mathbf{t} \rangle_{\partial_t \Omega} = 0, \quad (2.72)$$

$$\frac{2\ell}{c_0} (\nabla c, G_c \nabla d) + \frac{1}{c_0 \ell} (c, G_c \alpha'(d)) + (c, g'(d) \psi_e^+(\boldsymbol{\epsilon}(\mathbf{u}))) = 0, \quad (2.73)$$

with the initial damage condition,

$$(c, d(0, \mathbf{x}) - d_0) = 0. \quad (2.74)$$

Observe that (2.73) is an equality rather than an inequality, such as (2.64). This reflects a view ahead, toward discretization, where in the present work the irreversibility constraint is enforced with an active-set strategy. The active set strategy effectively partitions the domain into active (where  $\dot{d} = 0$ ) and inactive (where  $\dot{d} > 0$ ) parts. Only the inactive part requires a discretization of the damage condition (2.64), where it is indeed treated as an equality. A detailed description of this constrained optimization algorithm is given by Heister et al. in [62], and some additional details pertinent to phase-field for fracture discretizations can be found in Hu et al. [100].

Finally, these function spaces can be discretized over a finite element mesh, that give rise to the discrete function spaces  $\mathcal{U}_t^h \subset \mathcal{U}_t$ ,  $\mathcal{V}^h \subset \mathcal{V}$ ,  $\mathcal{D}_t^h \subset \mathcal{D}_t$ ,  $\mathcal{C}^h \subset \mathcal{C}$ . These are then used to construct the discrete form of the problem using the Galerkin method:

### Spatially discretized form

Find  $\mathbf{u}^h \in \mathcal{U}_t^h$  and  $d^h \in \mathcal{D}_t^h$ , such that  $\forall \mathbf{w}^h \in \mathcal{V}^h$  and  $\forall q^h \in \mathcal{C}^h$ ,

$$(\nabla \mathbf{w}^h, \boldsymbol{\sigma}^h) - (\mathbf{w}^h, p \nabla d^h) - (\mathbf{w}^h, \mathbf{b}) - \langle \mathbf{w}^h, \mathbf{t} \rangle_{\partial_t \Omega} = 0, \quad (2.75a)$$

$$\frac{2\ell}{c_0} (\nabla c^h, G_c \nabla d^h) + \frac{1}{c_0 \ell} (c^h, G_c \alpha'(d^h)) + (c^h, g'(d^h) \psi_e^+(\boldsymbol{\epsilon}(\mathbf{u}^h))) = 0, \quad (2.75b)$$

with the initial damage condition,

$$(c^h, d^h(0, \mathbf{x}) - d_0) = 0. \quad (2.76a)$$

In this work, bilinear finite elements are used to approximate the damage and displacement fields.

The coupling between the two discrete equations (2.75a) and (2.75b) is handled by an alternating minimization scheme. A detailed description of this scheme is given in [100]. This solution scheme is implemented using RACCOON [101], a parallel finite element code specializing in phase-field fracture problems. RACCOON is built upon the MOOSE framework [102, 103] developed and maintained by Idaho National Laboratory.

## 2.5 Results

We now present results for a set of problems that highlight the advantages, as well as some limitations, of the various models for pressurized cracks in a phase-field for fracture setting. In the first problem, the cohesive fracture of an uniaxial specimen in a pressurized environment is analyzed. We then consider the problem of crack nucleation from a pressurized hole in a medium subjected to far-field, biaxial com-

pression. Finally, a crack propagation example is studied to verify that in the limit of a vanishing regularization length Griffith-like behavior is recovered with the new model. In all cases, plane-strain conditions are assumed to hold.

In the course of explaining the results obtained with the cohesive phase-field model, it will be useful to characterize the effective cohesive strength  $\sigma_c$  of the material. To that end we will rely on the following relationship between the cohesive strength and the nucleation energy:

$$\sigma_c = \sqrt{\frac{2E\psi_c}{(1-\nu^2)}}, \quad (2.77)$$

where  $E$  denotes Young's modulus and  $\nu$  Poisson's ratio. This equation results from the analysis of a one-dimensional system subjected to uniaxial loading [78], and should be viewed as an approximation to the cohesive strength in more general loading conditions.

### 2.5.1 Uniaxial bar under traction in a pressurized environment

We consider the fracture behavior of a cohesive material with pressure loading on the crack faces. The example is intended to examine the extent to which the pressure loading can artificially influence the apparent traction-separation law on the crack surface.

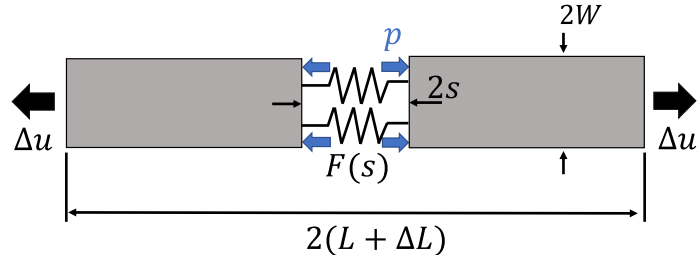


FIGURE 2.4. Uniaxial cohesive bar.

The problem consists of a bar under a displacement controlled load in a pressurized chamber, as shown in Figure 2.4. The bar is assumed to be made of a

	Value	Unit
Young's modulus ( $E$ )	$4.0 \times 10^5$	MPa
Poisson's ratio ( $\nu$ )	0.2	–
Nucleation energy ( $\psi_c$ )	$5.6 \times 10^{-5}$	$\text{mJ mm}^{-3}$
Critical fracture energy ( $G_c$ )	0.12	$\text{mJ mm}^{-2}$
Residual stiffness ( $\xi$ )	$1.0 \times 10^{-8}$	–

**Table 2.1.** Material properties for uniaxial bar

linear elastic material that undergoes cohesive fracture, with a traction-separation law  $F(s)$ . The bar has an undeformed length  $2L = 400$  mm and width  $2W = 2$  mm. The material properties are given in Table 2.1. Symmetry boundary conditions are invoked to reduce the computational domain to the top-right quarter of the bar. The applied load is modeled as a displacement boundary condition on the right end of the domain. The mesh consists of rectangular elements of size  $h$  along the length direction and size 1 mm in the width direction. The initial applied displacement increment is  $\Delta u = 5 \times 10^{-4}$  mm. The displacement increment is adaptively refined when convergence is not obtained within a fixed set of iterations. A more detailed description of the adaptive stepping procedure is provided in [102, 103, 104].

Damage localization is triggered by introducing a small initial defect ( $d = \mathcal{O}(\epsilon)$ ) on the left side of the domain. In what follows, results are reported using  $\ell = L/20 = 10$  mm and  $h = \ell/10 = 1$  mm. This choice of regularization length and mesh spacing was found to yield spatially-converged results. Different values of pressure, ranging from 0 to  $\sigma_c/3$  are considered.

The problem is simulated using discretized versions of both the UVC and (LVC) formulations. For the indicator function  $I(d)$ , results are reported for: (1)  $I(d) = d$ , used for example in [1]; (2)  $I(d) = d^2$ , used in [82] and (3)  $I(d) = 2d - d^2$ , used in [52]. The effective traction-separation laws extracted from the set of simulations are shown in Figure 2.5. To generate these curves, the traction is computed as the internal force measured in the center of the bar. The separation  $s$  is the opening of

the crack, calculated as  $s = - \int_{-\infty}^{\infty} \mathbf{u} \cdot \nabla I(d) dx$  [1].

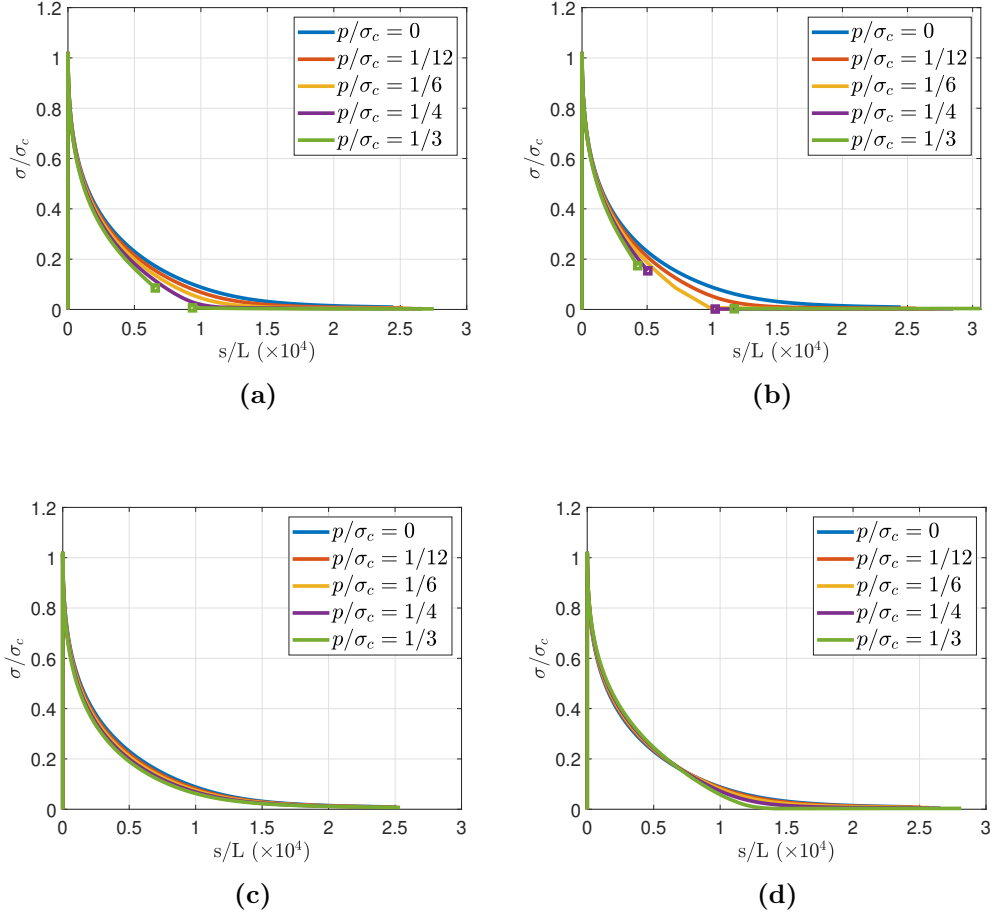


FIGURE 2.5. Traction-separation curves for pressurized uniaxial cohesive bar problem, obtained with various phase-field models: (a) (LVC) with linear indicator function; (b) (LVC) with quadratic indicator function; (c) (LVC) with  $2d - d^2$  indicator function; and (d) Proposed approach (UVC) with linear indicator function.

The results for the various models are shown in Figure 2.5, with tractions and pressures normalized by the critical stress  $\sigma_c$  from (2.77). As shown in Figure 2.5, the proposed model (UVC) exhibits minimal sensitivity to the pressure magnitude in the traction-separation behavior. By contrast, with the (LVC) formulation, only the case with  $I(d) = 2d - d^2$  exhibits comparable results. In the other two cases (Figures 2.5a and 2.5b), the apparent traction-separation law shows a spurious dependence

to the applied pressure. This is evident in the variations in the results as well as the presence of jumps in the aperture at sufficiently high pressures. The latter occur due to an instability of the partially damaged solutions as  $d$  approaches 1. More precisely, shortly after the damage at the center of the bar reaches  $d \approx 0.8$ , it jumps to  $d = 1$ , which in turns lead to a jump in the aperture. This jump is indicated via the squares that appear on selected curves in Figures 2.5a and 2.5b. The use of smaller displacement increments was not observed to significantly impact these results. By contrast, such instabilities were not observed for the simulations reported in Figures 2.5c and 2.5d.

### 2.5.2 Crack nucleation from a pressurized hole

Consider a square plate of dimensions  $L \times L$ , with a circular hole in the center subjected to an internal pressure  $p$ , as shown in Figure 2.6a. This problem is motivated by oil and gas wellbore systems. Far field stresses  $\sigma_V$  and  $\sigma_H$  are applied as tractions on the boundaries as shown. The pressure is increased until it reaches a “break-down pressure”  $p_b$ . When that happens, cracks initiate in the direction parallel to the maximum *in-situ* stress. Assuming  $\sigma_H > \sigma_V$ , this is expected to occur along a horizontal axis passing through the center of the hole. In this work, the pressure in the hole is assumed to follow the crack faces as the fracture grows into the interior of the domain.

The material properties selected for this problem, along with the dimensions and loading parameters are listed in Table 2.2. The material properties are taken to be representative of a Bebertal sandstone, as inspired by the experiments of [105]. The symmetry of the problem is exploited to reduce the computational domain to the top-left quarter. An unstructured triangular mesh is used, with local refinement along the  $x$ -axis, as shown in Figure 2.6b. The element size in the refined area is 10mm, whereas the phase-field regularization length is  $\ell = 40$ mm. For the results reported

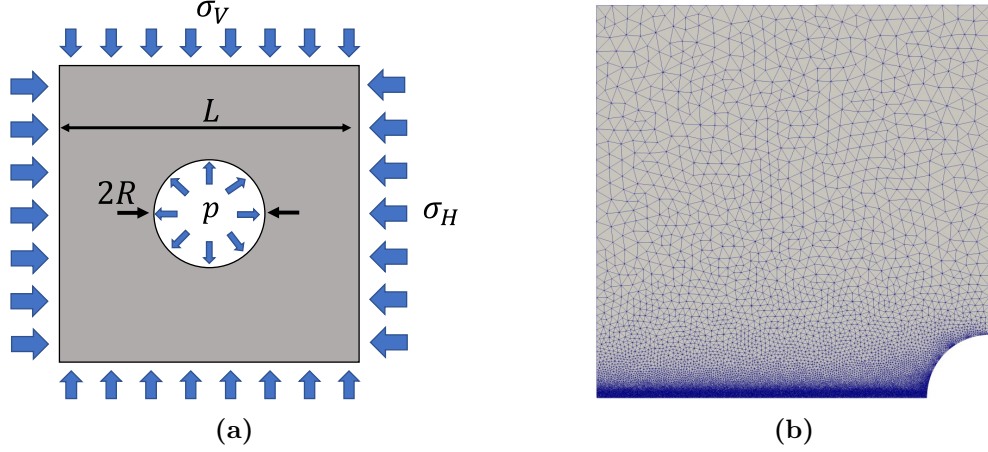


FIGURE 2.6. (a) Problem schematic; (b) Mesh used in the computations, exploiting symmetry.

	Value	Unit
Young's modulus ( $E$ )	$19.0 \times 10^3$	MPa
Poisson's ratio ( $\nu$ )	0.2	—
Nucleation energy ( $\psi_c$ )	$7.96 \times 10^{-4}$	$\text{mJ mm}^{-3}$
Critical fracture energy ( $G_c$ )	$7.70 \times 10^{-2}$	$\text{mJ mm}^{-2}$
Cavity radius ( $R$ )	400	mm
Specimen length ( $L$ )	$5.0 \times 10^3$	mm
Horizontal stress ( $\sigma_H$ )	5.0	MPa
Vertical stress ( $\sigma_V$ )	2.5	MPa

**Table 2.2.** Material properties, geometric parameters and applied loads for crack initiation problem

in this section, the phase-field model employs the cohesive formulation[77, 78] using the degradation function (2.40) and the spectral split of [89].

Intuitively, the magnitude of the pressure load required to initiate fracture in this problem is expected to be independent of whether or not the pressure follows the crack evolution. After initiation, the pressure effects become important and the fracture propagates unstably. Due to this unstable behavior, it is very difficult to numerically capture the crack path after the pressure  $p_b$  is reached. In order to have a glimpse into what this path looks like, a viscous term  $\eta \dot{d}$  is added to the phase-field equation, as in [89], with  $\eta = 10^{-3} \text{ mJ} \cdot \text{mm}^{-3} \cdot \text{s}$ .

It bears emphasis that the equations (2.9) and (2.11) indicate that, in the absence of any damage, the proposed model for pressurized cracks reduces to the standard phase-field fracture model for traction-free cracks. Therefore, one should expect the proposed model to capture fracture initiation properly in this scenario. On the other hand, for the (LVC) formulation, this only occurs if the indicator function satisfies  $I'(0) = 0$ . Among the many works which use the (LVC) formulation, only a few such as [82, 81] used an indicator function satisfying this condition. In [82], the authors were indeed able to predict fracture initiation from pressurized holes. To highlight the implications of having  $I'(0) \neq 0$  in the model (LVC), the results for this problem will also be presented using the (LVC) formulation with the indicator function  $I(d) = d$ .

The final damage patterns obtained using the (UVC) formulation and the (LVC) formulation are shown in Figure 2.7. With the (UVC) formulation, damage localizes along the midplane when the hoop stress is approximately 85% of  $\sigma_c$ . This is not unexpected, as the expression (2.77) is based on a one-dimensional state of stress and strain which differs significantly from the state near the corner of the hole. The same comparison is not performed for the simulation using the model (LVC), since damage forms only on the boundary in the first steps leading to spurious rigid body motion.

The main takeaway is that the proposed model (UVC) allows one to study crack nucleation and subsequent propagation under a pressure load, whereas formulation (LVC) leads to spurious damage formation if  $I'(0) \neq 0$ . The presence of the term  $p\nabla \cdot \mathbf{u}I'(d)$  in the damage equation (2.19) drives crack formation in areas which are not stressed. For this specific problem, this issue can be circumvented using for example  $I(d) = d^2$ , as shown in [82], but this option introduces a spurious dependence of the cohesive response of the material on the applied pressure, as indicated in the last section (Figure 2.5b).

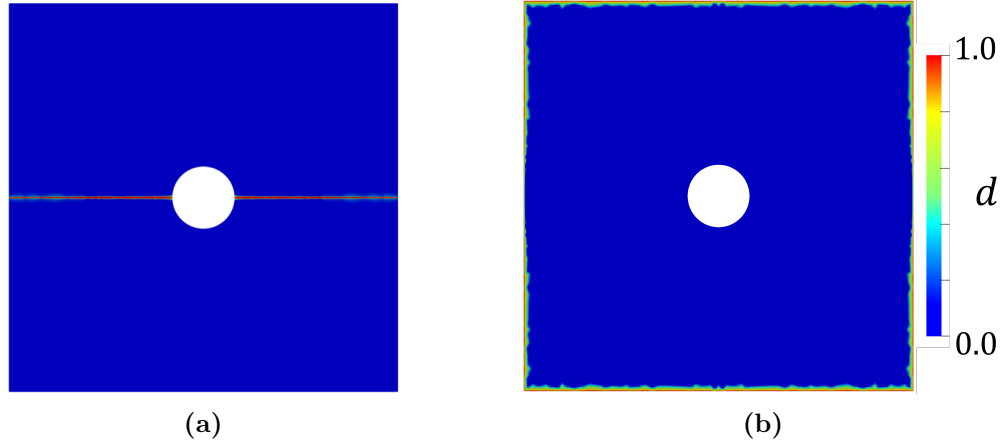


FIGURE 2.7. (a) Final crack pattern using proposed model; (b) Damage field using the model from [1].

### 2.5.3 Stable propagation of a pre-existing crack

Consider a strip of material with a pressurized crack, as shown in Figure 2.8a. The rectangular strip has a width  $W$ , height  $H$  and a crack with initial size  $a$  (values provided in Table 2.3), and is loaded by the “surfing” boundary condition  $\widetilde{U}_y(x, y, t)$  on its top and bottom surfaces [85]. The boundary condition is given by

$$\widetilde{U}_y(x, y, t) = U_y(x - Vt, y), \quad (2.78)$$

where

$$U_y(x, y) = \hat{U}_y(r, \theta) = \frac{\sqrt{G_c E'}}{2\mu} \sqrt{\frac{r}{2\pi}} (\kappa - \cos \theta) \sin \frac{\theta}{2}, \quad (2.79)$$

and where  $r$  and  $\theta$  are polar coordinates with respect to the origin, taken to be the midpoint of the left edge of the domain. The constant  $V > 0$  is the target crack speed, prescribed by moving the boundary condition following (2.78). The Kolosov constant is defined as  $\kappa = 3 - 4\nu$  in plane strain and the shear modulus  $\mu = E/(2 + 2\nu)$ . The pressure  $p$  applied to the crack faces as the crack evolves is

given by

$$p = \frac{1}{2} \sqrt{\frac{G_c E'}{\pi a}}, \quad (2.80)$$

in which  $a$  denotes the initial crack length. This value corresponds to half the critical pressure for an infinite plate with a pressurized crack of size  $a$ . This magnitude ensures that the applied pressure is considerably large, but not so large as to drive the problem beyond the stable propagation regime.

To calculate the energy release rate, the domain form of the J-Integral (2.43) developed in Section 2.3 is used. The function  $q$  is constructed by taking advantage of the finite element interpolation. In essence, the domain for the J-Integral is taken to be a single rectangular region of dimensions  $a \times H/2$ , centered on the initial crack tip. The value of  $q$  for all nodes outside of this region is set to 0, while  $q = 1$  for all nodes inside. Using the finite element interpolation, this gives rise to a  $q$  function whose value changes continuously from 0 to 1 on the elements cut by the rectangular path. This function is illustrated in Figure 2.8b<sup>3</sup>.

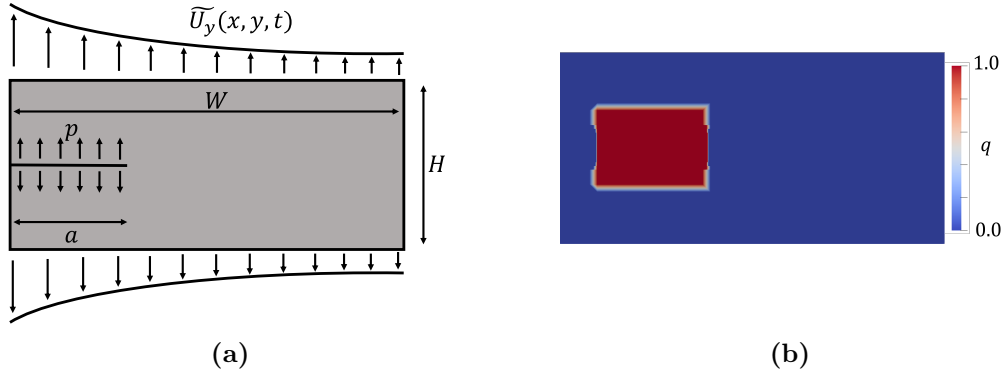


FIGURE 2.8. (a) Geometry and boundary conditions for pressurized crack propagation problem; (b) J-Integral domain function  $q$ .

---

<sup>3</sup> Due to mesh refinement near the crack surface, the width of the band where  $0 < q < 1$  diminishes near the horizontal centerline of the domain.

	Value	Unit
Young's modulus ( $E$ )	$3.0 \times 10^4$	MPa
Poisson's ratio ( $\nu$ )	0.2	—
Critical fracture energy ( $G_c$ )	0.12	$\text{mJ mm}^{-2}$
Initial crack length ( $a$ )	1.6	m
Specimen width ( $W$ )	8.0	m
Specimen height ( $H$ )	4.0	m
Target crack speed ( $V$ )	0.4	$\text{m/s}$

**Table 2.3.** Parameters used for pressurized crack propagation problem

In order to verify that Griffith's law is approached as  $\ell \rightarrow 0$ , simulations are performed for this problem using a sequence of decreasing regularization lengths, ranging from  $\ell = a/20$  to  $\ell = a/160$ . The mesh is locally refined along the  $x$ -axis, where the element size is set to  $h = \ell/4$ . The symmetry of the problem is exploited and only the response in the top half of the domain is simulated. In terms of constitutive choices of the phase-field model, the AT-1 formulation is employed without any decomposition of the strain. As in the previous examples, this problem is analyzed using the formulations (LVC) and (UVC), and the following choices of indicator function  $I(d)$ :

- $I(d) = d$
- $I(d) = d^2$
- $I(d) = 2d - d^2$

To evaluate how well the models approach Griffith's law, the ratio between the energy release rate measured by the J-Integral and the effective critical fracture energy  $G_c^{eff} = (1 + 2h/c_0\ell)G_c$ <sup>4</sup> is plotted in Figures 2.9 and 2.10. In all figures, the time is scaled by a characteristic time  $\tau$ , defined as  $\tau = a/V$ . The results

---

<sup>4</sup> in fact, phase-field cracks actually dissipated a slightly larger energy per unit length in numerical models. A correction factor of  $\left(1 + \frac{2h}{c_0\ell}\right)$  is then applied to  $G_c$ , following [61]. The factor of 2 here comes from the symmetry boundary condition employed.

using the traditional (LVC) formulation are presented in Figure 2.9. They indicate convergence towards  $J/G_c^{eff} = 1$  as the regularization length is reduced, especially when the indicator function  $I(d) = d$  is used. This is expected given the results obtained in [1]. Nevertheless, these results serve to verify the implementation of the J-Integral presented in Section 2.3. They also provide an estimate for how small the regularization length has to be in order to achieve a certain level of accuracy with these types of phase-field models.

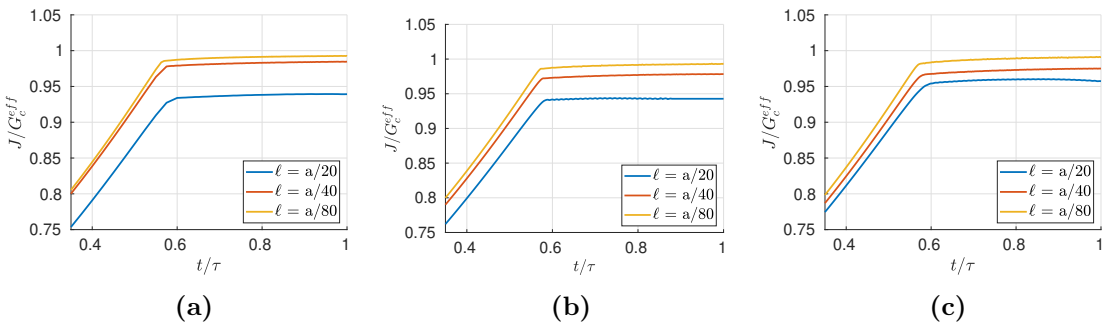


FIGURE 2.9. Reference results with the LVC formulation. Curves with  $\ell = a/160$  are not shown, as they are almost identical to the ones with  $\ell = a/80$ . (a)  $I(d) = d$ ; (b)  $I(d) = d^2$ ; (c)  $I(d) = 2d - d^2$

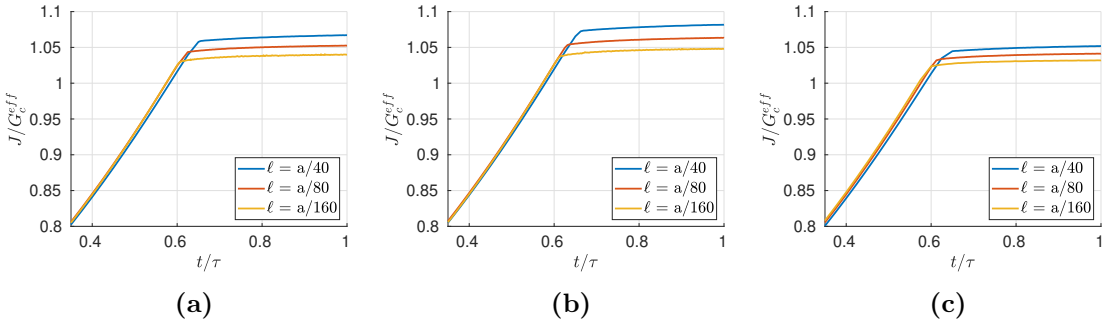


FIGURE 2.10. Results with the proposed formulation (UVC) (a)  $I(d) = d$ ; (b)  $I(d) = d^2$ ; (c)  $I(d) = 2d - d^2$

For the case of proposed formulation (UVC), the results shown in Figure 2.10 indicate a slower convergence towards a  $J/G_c^{eff} = 1$  response. In contrast with the (LVC) formulation, the curves converge from above, and therefore, the fracture

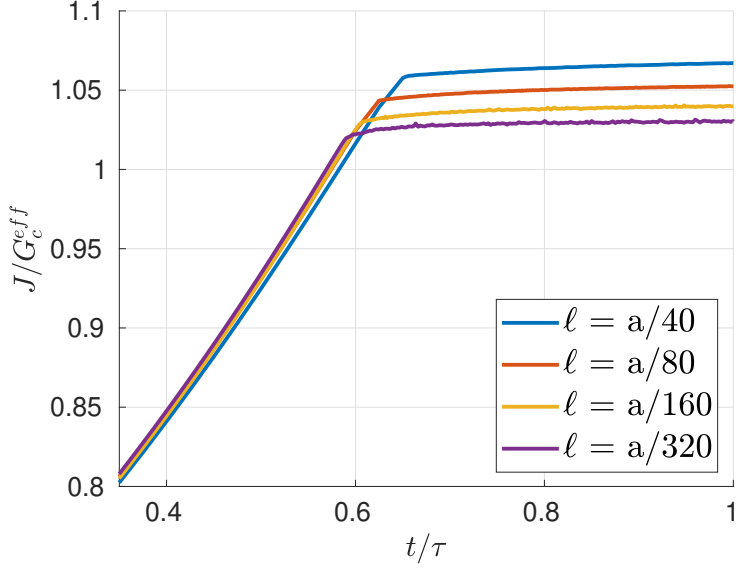


FIGURE 2.11. Convergence of the proposed formulation with  $I(d) = d$ .

$\ell/a$	Error	Error <sub>k+1</sub> /Error <sub>k</sub>
1/40	0.067	—
1/80	0.052	0.78
1/160	0.040	0.77
1/320	0.031	0.77

**Table 2.4.** Absolute error in  $J$  vs.  $G_c^{eff}$  for the pressurized crack propagation problem, as a function of regularization length.

toughness is slightly overestimated when larger regularization lengths are used. Nevertheless, they all seem to approach a Griffith-like response in the limit  $\ell \rightarrow 0$ . In Figure 2.11, an even finer result, using (UVC) with  $I(d) = d$  and  $\ell = a/320$  is added, to ensure that the convergence rates indicated in Figure 2.10 persist. In Table 2.4, the relative errors are provided, indicating a convergence rate of approximately 0.4 with respect to  $\ell$ .

One potential explanation for the slower convergence rate is related to the different assumptions regarding the trial cracks, as discussed in Section 2.2. Although the different assumptions converge to the same propagation rule in the limit of an infinitesimal crack increment, in the discretized case, the minimal crack increment is

finite and related to the mesh spacing  $h$  and regularization length  $\ell$ . In this case, a slightly different propagation behavior, resulting in slower convergence rates towards  $J/G_c^{eff} = 1$  is not surprising.

# 3

## A Multi-Resolution Approach for Hydraulic Fracture Simulation<sup>1</sup>

### 3.1 Introduction

The approach presented in this Chapter, which constitutes the core of this work, is referred to as a multi-resolution method. It extends the concept of a hybrid phase-field method [68, 67, 69] to hydraulic fracturing. The method discretizes the problem at a global level using a sharp interface approach based on the Embedded Finite Element Method of Cusini et al. [5]. It then approaches the simulation of fracture evolution by coupling the global fields with a phase-field fracture problem posed over a subdomain in the vicinity of the crack front, which brings several advantages. The crack aperture and flow inside the fracture are handled at the global scale using techniques that work well and are efficient when the crack geometry is known. Then the phase-field model is employed in the subdomain to effectively update the crack geometry. This framework lends itself to incorporation with a wide range of existing hydraulic fracturing solvers, as the phase-field sub-problem is agnostic about the type of numerical treatment used in the global domain.

---

<sup>1</sup> This chapter's content is derived from Costa *et al.*[106]

The Chapter is structured as follows. In Section 3.2, we present the governing equations and constitutive assumptions for both hydraulic fracturing and phase-field for fracture. In Section 3.3, we propose our multi-resolution framework and present numerical schemes to discretize both the hydrofracture and the phase-field subproblems. In Section 3.4, we apply our method to study hydraulic fracturing in some simple scenarios, in order to verify its accuracy. These include the well-known KGD[20, 19] problems and a case of non-planar fracture propagation around a stiff inclusion.

## 3.2 Model formulation

In this section, we describe the models that are used to develop our multi-resolution scheme. We start by presenting the governing equations to model hydraulic fracture in poroelastic rock that forms the basis for the solver at the global scale. We then describe a phase-field model for fracture that forms the basis for the solver used in local subdomains near the crack tips.

### 3.2.1 Governing equations for hydraulic fracture

We consider a model that couples flow and elastic deformation in a porous media with evolving fracture surfaces. Consider the domain  $\Omega$  consisting of a porous rock, that is fully saturated with a single-phase Newtonian fluid. The external boundary is composed of both traction  $\partial\Omega_t$  and displacement  $\partial\Omega_u$  surfaces, viz.  $\partial\Omega = \partial\Omega_t \cup \partial\Omega_u$ .

The domain contains fractures  $\Gamma$ , as shown in Figure 3.1. For simplicity, we assume quasi-static conditions and small-strain kinematics. Neglecting inertial effects, the balance of linear momentum reads

$$\nabla \cdot \boldsymbol{\sigma} + \mathbf{b} = \mathbf{0} \text{ on } \Omega \setminus \Gamma, \quad (3.1)$$

where  $\boldsymbol{\sigma}$  denotes the total Cauchy stress and  $\mathbf{b}$  the body force. The mechanical

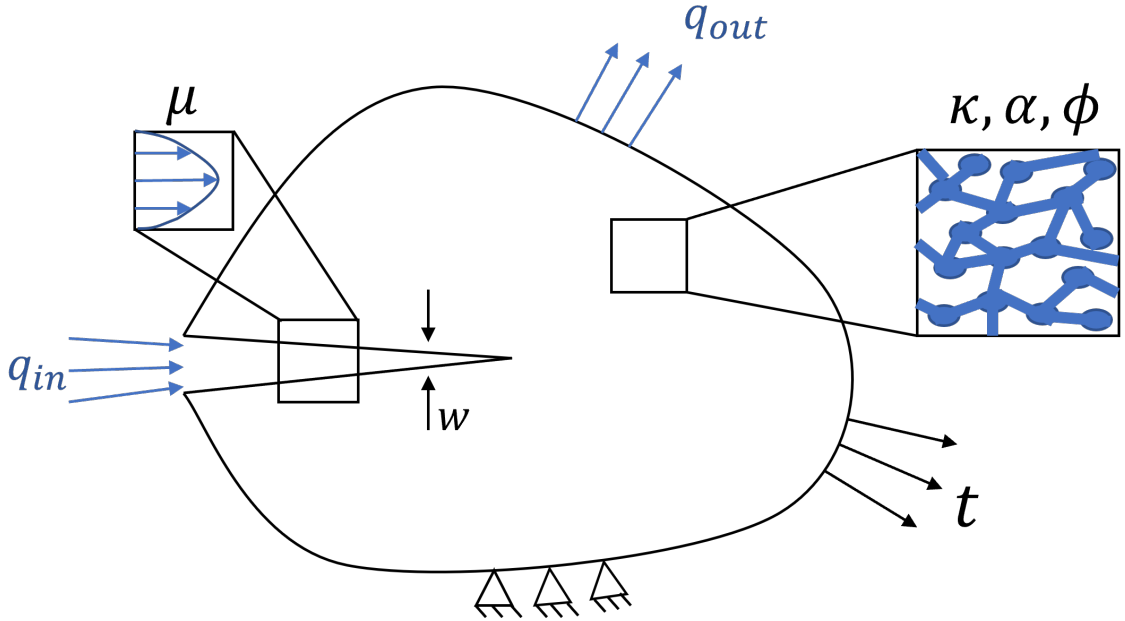


FIGURE 3.1. Schematic of a poroelastic rock with a fracture, inspired by [2].

boundary conditions are given by

$$\boldsymbol{\sigma} \cdot \mathbf{n} = \mathbf{t} \text{ on } \partial\Omega_t, \quad (3.2)$$

$$\mathbf{u} = \bar{\mathbf{u}} \text{ on } \partial\Omega_u, \quad (3.3)$$

where  $\mathbf{n}$  denotes the normal direction at any point on  $\partial\Omega$ ,  $\mathbf{t}$  are the applied tractions, and  $\bar{\mathbf{u}}$  denotes the prescribed displacements.

Fluid flow within the cracks gives rise to pressure loads on the crack surfaces, translating into the boundary condition

$$\boldsymbol{\sigma}^+ \cdot \mathbf{n}_\Gamma = -\boldsymbol{\sigma}^- \cdot \mathbf{n}_\Gamma = -p_f \mathbf{n}_\Gamma \text{ on } \Gamma, \quad (3.4)$$

where  $p_f$  is the pressure inside the crack and  $\mathbf{n}_\Gamma$  is the normal vector to  $\Gamma$  at any point. In this work, we assume that fractures are open and neglect contact conditions on crack faces. For additional considerations to account for closed fractures, see the model described in Cusini et al.[5].

In terms of the fluid flow, the fluid velocity  $\mathbf{v}_m$  in the matrix is governed by the mass balance

$$\frac{\partial(\rho\phi)}{\partial t} + \nabla \cdot (\rho\mathbf{v}_m) = Q_m + Q_{mf} \text{ on } \Omega \setminus \Gamma. \quad (3.5)$$

where  $\rho$  denotes the fluid density and  $\phi$  is the porosity, and  $Q_m$  is a prescribed source term in the matrix. The source term  $Q_{mf}$  accounts for the exchange of fluid between the matrix and the fractures. The boundary is partitioned into pressure  $\partial\Omega_p$  and flux  $\partial\Omega_q$  portions, such that  $\partial\Omega = \partial\Omega_p \cup \partial\Omega_q$ , and the following boundary conditions are applied,

$$\rho\mathbf{v}_m \cdot \mathbf{n} = \mathbf{q} \text{ on } \partial\Omega_q, \quad (3.6)$$

$$p_m = \bar{p}_m \text{ on } \partial\Omega_p, \quad (3.7)$$

where  $p_m$  denotes the pore-pressure and  $\bar{p}_m$  is a prescribed pressure.

In a comparable manner, the fluid velocity  $\mathbf{v}_f$  within fractures is governed by the mass balance

$$\frac{\partial(\rho w)}{\partial t} + \nabla_\Gamma \cdot (\rho w \mathbf{v}_f) = Q_f + Q_{fm} \text{ on } \Gamma, \quad (3.8)$$

where  $w$  denotes the normal fracture aperture,  $Q_f$  is a prescribed source term within the fracture, and  $Q_{fm}$  accounts for the exchange of fluid between the fracture and the matrix<sup>2</sup>. In the above,  $\nabla_\Gamma$  indicates a gradient operator taken on the lower dimensional manifold  $\Gamma$ . Boundary conditions similar to (3.6) and (3.7) can also be applied.

Constitutive relationships are required to close the system and tie the stresses to the displacements  $\mathbf{u}$  and the fluid velocities to the pressures. In particular, we adopt

---

<sup>2</sup> the flux interactions  $Q_{fm}$  and  $Q_{mf}$  are modeled as in classical well models, following [46]. This ensures the balance of mass between the fractures and matrix  $\int_V Q_{mf} dV = - \int_\Gamma Q_{fm} d\Gamma$ .

the basic assumptions of Biot's theory of poroelasticity [107], Darcy's law for the flow in the matrix, and a lubrication theory approximation for the flow in fractures. This gives rise to the following set of constitutive relationships for the stress, porosity, and velocities:

$$\boldsymbol{\sigma} = \mathbb{C} : \boldsymbol{\epsilon}(\mathbf{u}) - \alpha p_m \mathbb{I} \text{ on } \Omega \setminus \Gamma, \quad (3.9)$$

$$\dot{\phi} = \alpha \nabla \cdot \dot{\mathbf{u}} + \frac{\dot{p}_m}{N} \text{ on } \Omega \setminus \Gamma, \quad (3.10)$$

$$\mathbf{v}_m = -\frac{\kappa}{\mu} \nabla p_m \text{ on } \Omega \setminus \Gamma, \quad (3.11)$$

$$\mathbf{v}_f = -\frac{w^2}{12\mu} \nabla_{\Gamma} p_f \text{ on } \Gamma. \quad (3.12)$$

In the above,  $p_m$  is the pore-pressure,  $\mathbb{C}$  is the fourth-order isotropic tensor of drained elastic moduli,  $\boldsymbol{\epsilon}(\mathbf{u})$  is the mechanical strain,  $\alpha$  is the Biot coefficient, and  $\mathbb{I}$  is the second-order identity tensor. The temporal evolution of the porosity is governed by the rate of dilatation and time rate of change in the pore pressure, as modulated by the modulus  $N$ . The fluid velocity in the matrix is related to the gradient of the pressure through the ratio of the intrinsic permeability  $\kappa$  to the viscosity  $\mu$ .

The fluid is assumed to be linearly compressible. For both the fluid in the fractures and the matrix, this implies that the density is updated from its reference value  $\rho_{ref}$  based on the change in pressure according to

$$\rho = \rho_{ref} \left( 1 + \frac{p - p_{ref}}{K_F} \right) \text{ on } \Omega, \quad (3.13)$$

where  $p_{ref}$  denotes a reference value for the pressure, and  $K_F$  is the fluid bulk modulus.

Finally, the initial conditions for the displacements and pressures are given by

$$\mathbf{u}(\mathbf{x}, 0) = \mathbf{u}^0 \text{ on } \Omega \setminus \Gamma, \quad (3.14)$$

$$p_m(\mathbf{x}, 0) = p_m^0 \text{ on } \Omega \setminus \Gamma, \quad (3.15)$$

$$p_f(\mathbf{x}, 0) = p_f^0 \text{ on } \Gamma. \quad (3.16)$$

For a given crack geometry, the combination of equations (3.1), (3.5) and (3.8), with constitutive assumptions (3.9) - (3.13), boundary conditions (3.2)-(3.4),(3.6),(3.7) and initial conditions (3.14)-(3.16) leads to a system of equations whose solution can be approximated by many different numerical methods. What remains is a model to describe the evolution of the crack geometry.

In the context of standard sharp interface approaches for hydraulic fracture, the evolution of the crack geometry is typically governed by a set of criteria that dictate whether or not a crack front extends and, if so, in what orientation. For crack extension, a standard approach is to adopt Griffith's criteria [50], which states that crack propagation should occur when the energy release rate  $G$  reaches the critical value  $G_c$  for the material, i.e.  $G \leq G_c$ . In terms of changes to orientation, several different criteria are typically employed, such as the maximum hoop stress criteria [108, 109, 110] or the maximum energy release rate condition [111, 112, 113]. Examples of works from the hydraulic fracture field employing such criteria include [114, 115, 116].

Although such methods have seen some success in simulating the propagation

of hydraulically-driven cracks, even in three dimensions [41, 42, 117], they struggle as crack evolution becomes sufficiently complex. By contrast, regularized methods have seen far more success in treating complex geometric evolution. In the next subsection, we present the governing equations for a phase-field method for fracture, a regularized approach for representing fractures and their evolution. Phase-field for fracture models generally start from a single energetic postulate that generalizes Griffith's criteria, and which is able to describe the entire fracture propagation process.

### 3.2.2 The phase-field method for fracture

The phase-field method for fracture started as an approximation [48] to the variational approach for fracture by Francfort and Marigo [47] for the quasi-static propagation of fracture in brittle materials. This model essentially states that a crack should evolve in a way that minimizes a total energy functional, among all admissible states, which are those that contain the current crack set (so that no healing is possible). For the method adopted in this work, we follow the work of Chukwudzie et al. [59] and associate the following total energy to a crack configuration  $\Gamma$  in a poroelastic brittle solid  $\Omega$ : where the tractions applied to the boundary are denoted by  $\mathbf{t}$ , the normal to the crack is denoted by  $\mathbf{n}_\Gamma$  and  $\mathcal{H}^{n-1}(\Gamma)$  is the  $n - 1$  dimensional Hausdorff measure of  $\Gamma$ .

The strain energy density  $W(\boldsymbol{\epsilon}(\mathbf{u}), p_m)$  is postulated as,

$$W(\boldsymbol{\epsilon}(\mathbf{u}), p_m) = \frac{1}{2} \left( \boldsymbol{\epsilon}(\mathbf{u}) - \frac{\alpha}{nK} p_m \mathbb{I} \right) : \mathbb{C} : \left( \boldsymbol{\epsilon}(\mathbf{u}) - \frac{\alpha}{nK} p_m \mathbb{I} \right), \quad (3.17)$$

with  $K$  denoting the bulk modulus and  $n$  the system's dimension (2 or 3). The phase-field regularization, based on the Ambrosio-Tortorelli [118] functional is then performed by the introduction of the damage parameter  $d$  and the regularization

length  $\ell$ ,

$$\begin{aligned}\mathcal{E}_\ell(\mathbf{u}, d, p_m, p_f) = & \int_{\Omega} \widetilde{W}(\boldsymbol{\epsilon}(\mathbf{u}), p_m, d) d\Omega - \int_{\partial\Omega_N} \mathbf{t} \cdot \mathbf{u} ds \\ & - \int_{\Omega} \mathbf{b} \cdot \mathbf{u} d\Omega + \int_{\Omega} p_f \mathbf{u} \cdot \nabla d d\Omega + \frac{G_c}{c_0} \int_{\Omega} \left( \frac{\zeta(d)}{\ell} + \ell \nabla d \cdot \nabla d \right) d\Omega,\end{aligned}\quad (3.18)$$

where the function  $\zeta(d)$  is the local dissipation function, which is usually taken as  $\zeta(d) = d$  or  $d^2$ . The constant  $c_0$  is given by  $c_0 = 4 \int_0^1 \sqrt{\zeta(z)} dz$  and the regularized strain energy is defined by,

$$\widetilde{W}(\boldsymbol{\epsilon}(\mathbf{u}), p_m, d) = \frac{1}{2} \left( (1-d)\boldsymbol{\epsilon}(\mathbf{u}) - \frac{\alpha}{nK} p_m \mathbb{I} \right) : \mathbb{C} : \left( (1-d)\boldsymbol{\epsilon}(\mathbf{u}) - \frac{\alpha}{nK} p_m \mathbb{I} \right), \quad (3.19)$$

which is consistent with an assumption of damage arising in the sub pore scale [59]. Finally, our regularized crack evolution problem is then stated as a minimization principle<sup>3</sup> for the functional  $\mathcal{E}_\ell(\mathbf{u}, d, p_m, p_f)$ , with respect to the variables  $\mathbf{u}$  and  $d$ , with the added condition that the damage process is irreversible and that the damage variable  $d$  is bounded between the values of zero (undamaged state) and unity (fully broken state):

$$\mathbf{u}, d = \underset{\mathbf{u}, d}{\operatorname{argmin}} \mathcal{E}_\ell(\mathbf{u}, d, p_m, p_f), \text{ subject to } \dot{d} \geq 0, \text{ and } 0 \leq d \leq 1. \quad (3.20)$$

The following set of evolution equations can then be derived from the Karush, Kuhn, Tucker (KKT) [98, 99] conditions:

---


$$\nabla \cdot ((1-d)^2 \mathbb{C} : \boldsymbol{\epsilon}(\mathbf{u}) - (1-d)\alpha p_m \mathbb{I}) + \mathbf{b} = p_f \nabla d, \quad (3.21)$$

<sup>3</sup> Since the focus of this Chapter is in the solution procedure, we opted to use the more established LVC hypothesis instead of the UVC one, proposed in Chapter 2.

$$S_d := \frac{2G_c\ell}{c_0} \Delta d - \frac{G_c}{c_0\ell} \zeta'(d) - g'(d)W(\boldsymbol{\epsilon}(\mathbf{u}), 0) + \alpha p_m \nabla \cdot \mathbf{u} + \nabla \cdot (p_f \mathbf{u}) \leq 0, \quad (3.22)$$

$$\dot{d} \geq 0, \quad (3.23)$$

$$0 \leq d \leq 1, \quad (3.24)$$

$$S_d \dot{d} = 0, \quad (3.25)$$

with boundary conditions,  $\boldsymbol{\sigma} \cdot \mathbf{n} = \mathbf{t}$  on  $\partial\Omega_N$  and  $(2G_c\ell\nabla d + c_0 p_f \mathbf{u}) \cdot \mathbf{n} \geq 0$  on  $\partial\Omega$ . The damaged stress is defined as  $\boldsymbol{\sigma} = (1-d)^2 \mathbb{C} : \boldsymbol{\epsilon}(\mathbf{u}) - (1-d)\alpha p_m \mathbb{I}$ .

In some cases, it is useful to decompose the energy (3.19) into positive and negative parts, in order to provide asymmetry between tension and compression states. In most problems studied in this Chapter, we found this decomposition to be important, and, unless otherwise mentioned, the spectral decomposition introduced in Miehe et al. [89] is used. With this decomposition, the equations for the macro-scale force balance (3.21) and the micro-force balance (3.22) are modified as

$$\nabla \cdot ((1-d)^2 \mathbb{C} : \boldsymbol{\epsilon}^+(\mathbf{u}) + \mathbb{C} : \boldsymbol{\epsilon}^-(\mathbf{u}) - (1-d)\alpha p_m \mathbb{I}) + \mathbf{b} = p_f \nabla d, \quad (3.22a)$$

$$S_d := \frac{2G_c\ell}{c_0} \Delta d - \frac{G_c}{c_0\ell} \zeta'(d) - g'(d)W(\boldsymbol{\epsilon}^+(\mathbf{u}), 0) - \alpha p_m \nabla \cdot \mathbf{u} + \nabla \cdot (p_f \mathbf{u}) \leq 0, \quad (3.23a)$$

and the damaged stress becomes  $\boldsymbol{\sigma} = (1-d)^2 \mathbb{C} : \boldsymbol{\epsilon}^+(\mathbf{u}) + \mathbb{C} : \boldsymbol{\epsilon}^-(\mathbf{u}) - (1-d)\alpha p_m \mathbb{I}$ . In the above,  $\boldsymbol{\epsilon}^+$  and  $\boldsymbol{\epsilon}^-$  denote the positive and negative parts of the strain tensor as described in [89].

Finally, to close this section, we note that the extent to which the solution to (3.20) approaches a particular sharp model in hydraulic fracture in the limit as the regularization length  $\ell \rightarrow 0$  has yet to be established. Nevertheless, the particular phase-field model adopted here contains all of the requisite components to allow for a proof of concept of the multi-resolution approach.

### 3.3 Multi-resolution method

#### 3.3.1 General overview

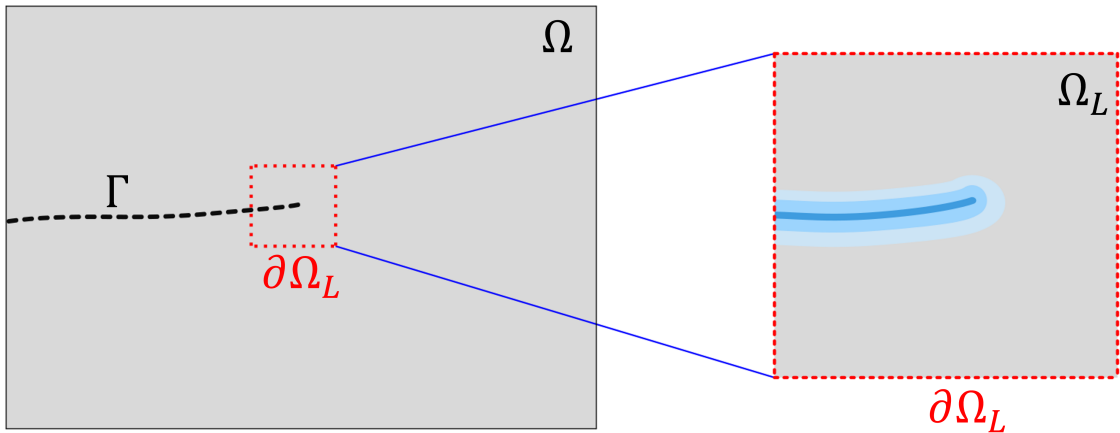


FIGURE 3.2. Global domain  $\Omega$  on the left and local domain  $\Omega_L$  on the right. The surface corresponding to the local domain boundary  $\partial\Omega_L$  is indicated within the global domain with the dashed red lines. The local domain is magnified to highlight the phase-field representation of the global crack  $\Gamma$ .

We propose a multi-resolution method to approximate the solution of the hydraulic fracture problem in porous media. It consists of coupling two problems between a global domain and a local subdomain, as shown in Figure 3.2. In the global domain problem, the governing equations (3.1)-(3.8) are discretized, and the crack is represented with a sharp geometry. The crack geometry is assumed to be fixed during a solution step in the global domain, and relevant fields are calculated over the entire domain.

By contrast, the local subdomain concerns only a portion of the entire domain,

namely in the vicinity of crack tips. It is encapsulated within the global domain as shown in Figure 3.2. In the local subdomain, a discretization of the variational principle (3.20) is used to simulate crack evolution. During a solution step in the local subdomain, the pressure fields within the fracture and matrix are assumed to be fixed.

The two problems are coupled in the following manner. The displacement and pressure fields are extracted from a solution step in the global domain and passed to the local subproblem in different ways. In particular, the global displacement fields are extracted along the surface  $\partial\Omega_L$ . These fields are then applied as Dirichlet boundary conditions for the local subproblem. The matrix pressure  $p_m$  and pressure in the fracture  $p_f$  are transferred as fields from the global domain to the local subdomain (see Section 3.3.3.2 for details), and assumed to be fixed for the local subproblem.

The aforementioned operations provide everything that is needed for the local subproblem from the global domain. Based on the imprint of the global crack geometry on the local subdomain, a regularized fracture surface is created (through an initial damage field) and then crack propagation is simulated in the local subdomain. Once an extension of the crack in a scale that can be represented in the global domain is identified, the sharp crack geometry in the global problem is updated accordingly.

In principle, the aforementioned multi-resolution approach can be implemented using a number of different discretization methods in the global domain and the local subdomain. In the sections that follow, we describe the particular choices used in this work as well as some important implementation details. The method is described in a two-dimensional context, but many aspects can be readily extended to three-dimensional problems.

### 3.3.2 Global problem discretization

The global problem in our multi-resolution approach encompasses the physics of fluid flow in both the fractures and the pore structure of our domain, as well as the deformation of the solid media. The set of governing equations consists of (3.1)-(3.8), combined with constitutive assumptions (3.9)-(3.13) and appropriate boundary conditions.

In this work, we use the discretization method proposed by Cusini et al. [5] in the study of fluid flow in fractured porous media. The domain  $\Omega$  is partitioned with a mesh  $\mathcal{T}$ . Then, the intersection of the fracture network  $\Gamma$  with  $\mathcal{T}$  defines the fracture triangulation  $\mathcal{F}$ . These meshes are then used to define discrete counterparts  $\mathbf{u}_G^h$ ,  $p_m^h$  and  $p_f^h$  of the unknown fields  $\mathbf{u}$ ,  $p_m$  and  $p_f$ , as well as discrete approximations of equations (3.1), (3.5) and (3.8).

A finite element approximation is constructed for the displacement field and employed in a standard Galerkin approximation to the global force balance (3.1). The continuous part of the displacement field is approximated with a standard space  $\mathcal{U}$  of 4-node bilinear shape functions  $\{\boldsymbol{\eta}_a\}$ . In the subset of elements that are “cut” by the global crack geometry, a space  $\mathcal{W}$  of discontinuous enrichment functions  $\{\boldsymbol{\phi}_b\}$  is constructed using the formulation described in [119].

The full displacement field in the global problem is constructed using both continuous and discontinuous parts as

$$\mathbf{u}_G^h = \underbrace{\sum_{a=1}^{n_u} u_a \boldsymbol{\eta}_a}_{\text{continuous part}} + \underbrace{\sum_{b=1}^{n_w} w_b \boldsymbol{\phi}_b}_{\text{discontinuous part}}, \quad (3.26)$$

where  $\{u_a\}, \{w_b\}$  are scalar degrees of freedom.

The flow equations (3.5) and (3.8) are discretized with a finite-volume method. Piecewise-constant pressure fields are constructed for  $p_m^h$  and  $p_f^h$  over the matrix mesh

$\mathcal{T}$  and the fracture mesh  $\mathcal{F}$ , respectively. Fluxes are computed using a two point flux approximation. The interaction between the flow in the fracture and matrix is effected via the embedded discrete fracture model (EDFM) [120, 46].

In terms of the temporal discretization, the parabolic nature of equations (3.5) and (3.8) gives rise to a stable time step for explicit schemes that scales with the cube of the mesh spacing [3, 66]. This upper bound is prohibitively small in most cases. Therefore, an implicit backward Euler method is used throughout. This gives rise to a fully-coupled system of nonlinear equations, whose solution is obtained with a Newton method, in a monolithic fashion.

One limitation of the construction (3.26) is that the discontinuous enrichment functions are not capable of representing a crack tip that terminates inside of an element. As such, any new extension of the crack geometry has to traverse from one side of a new element to another. The implementation of the fracture flow solver requires all cells to have non-zero volumes. Accordingly, new fracture cells are assigned a small aperture value ( $w_0$ ). The total discrete aperture of the cell is thus given by  $w_h = w_n + w_0$ , where  $w_n$  is the mechanical aperture that is consistent with the jump provided by the displacement field. The minimum opening  $w_0$  has been interpreted as a representation of the roughness of the fracture surfaces, providing a pathway for fluid flow even when the cracks are mechanically closed. See, for example [5].

### 3.3.3 Local problem initialization

#### 3.3.3.1 Construction of subdomain, submesh and damage-fixed nodes

A local subdomain of size  $L \times L$  is constructed by simply centering it on a global crack tip. The size  $L$  is selected to be an even integer multiplier of the global mesh spacing, leading to a square bounding box that conforms to the background mesh. This choice is adopted for convenience in this work, although other constructions are

possible, such as in [68].

To obtain the submesh  $\mathcal{T}_L$ , we start by considering the restriction of the global triangulation  $\mathcal{T}$  to the subdomain  $\Omega_L$ . The mesh for the local subdomain is constructed by uniformly refining the set of elements in this restriction. This facilitates the transfer of nodal data from the global to the local problem. The mesh size  $h_{local}$  in the local subdomain is chosen to be sufficiently small to resolve the damage band, of size  $\mathcal{O}(\ell)$ . In this work, we use  $\ell/h_{local} \approx 4$ .

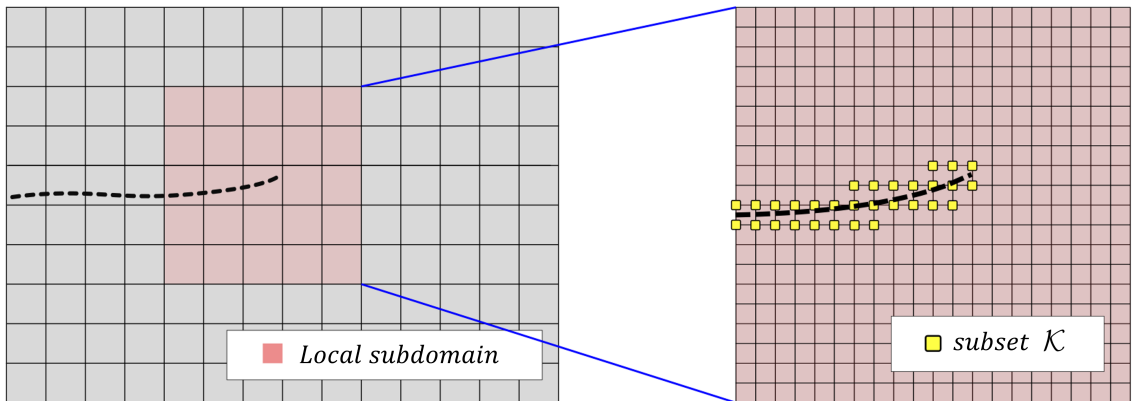


FIGURE 3.3. Global domain  $\Omega$  on the left and local domain  $\Omega_L$  on the right. The nodes in the subset  $\mathcal{K}$ , where  $d$  is set to 1 are colored in yellow.

The crack is represented by prescribing  $d = 1$  in a set  $\mathcal{K} \in \mathcal{T}_L$  of nodes in the local subdomain, as shown in Figure 3.3. This set is constructed in two steps. First, all elements of  $\mathcal{T}_L$  which are intersected by the global fracture triangulation  $\mathcal{F}$  are identified. Then,  $\mathcal{K}$  is defined to be the set of all nodes that belong to any of these intersected elements.

### 3.3.3.2 Transfer of global pressures to local mesh

Due to the different levels of resolution between the global and local problems, we find it advantageous to transfer the pressure fields in a particular manner. We note that in the global problem, the fracture pressures  $p_f^h$  are available at the cell centers of 1D finite volumes, and the matrix pressures  $p_m^h$  are available at the cell centers

of 2D finite volumes. These fields are transferred to quadrature points in the finite element mesh for the local subproblem using the transfer operators  $\Pi_f^{\Omega_L}$  and  $\Pi_m^{\Omega_L}$ .

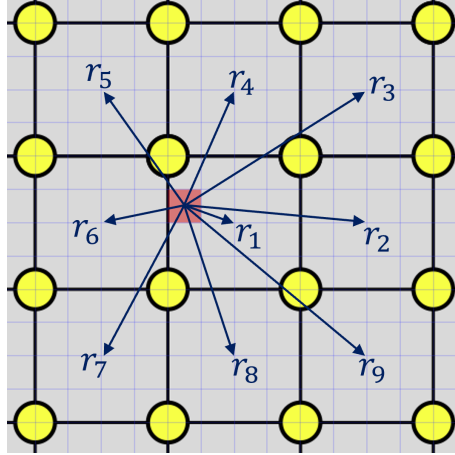


FIGURE 3.4. Illustration of global cells (in gray) in the neighborhood of a local element, indicated in pink. The matrix pressure at a quadrature point in the local element is calculated using an average of global pressures from neighboring cells  $\{i\}$ , with weights corresponding to the distances  $r_i$  between the quadrature point and the cell center.

The operator  $\Pi_f^{\Omega_L}$  that transfers the fracture pressure is straightforward, and inspired by a similar operation described in Santillán et al. [121]. Given any point  $\mathbf{x} \in \Omega_L$ , and a global fracture pressure field  $p_f^h$ ,  $\Pi_f^{\Omega_L} p_f^h(\mathbf{x})$  is obtained by finding the closest cell of  $\mathcal{F}$  to  $x$  and taking the value of  $p_f^h$  at this cell. More precisely,

$$\Pi_f^{\Omega_L} p_f^h(\mathbf{x}) = p_f^h(\arg \min_{c \in \mathcal{F}} \text{dist}(c, \mathbf{x})). \quad (3.27)$$

For the operator  $\Pi_m^{\Omega_L}$  that transfers the matrix pressure field, we use an averaging procedure. This has the effect of smoothing the matrix pressure field at the resolution of the local mesh. At a quadrature point  $\mathbf{x}_Q \in \Omega_L$ , the matrix pressure in the local domain is obtained from a weighted average of the pressures in the global cells that

surround the point. Specifically,

$$\Pi_m^{\Omega_L} p_m^h(\mathbf{x}_Q) = \frac{\sum_{i=1}^s r_i^{-1} p_m^h(c_i)}{\sum_{i=1}^s r_i^{-1}}, \quad (3.28)$$

where  $r_i$  denotes the distance between the quadrature point location and the center of global cell  $i$ , as indicated in Figure 3.4. In the sum, all cells that neighbor the global cell containing quadrature point  $\mathbf{x}_Q$  are used. In the particular case when a quadrature point happens to reside in the center of the local element and  $r_1 = 0$ , the above sum is replaced with  $\Pi_m^{\Omega_L} p_m^h(\mathbf{x}_Q) = p_m^h(c_1)$ .

### 3.3.4 Local problem discretization

With the local subdomain properly identified and initialized, we now describe the additional steps to discretize the displacement and damage fields in the local subdomain and solve for their approximations. The governing equations for the macro-force balance (3.21) and the damage evolution (3.22) are both treated with the finite element method. The damage and displacement fields are both approximated using four-node bilinear quadrilateral elements.

Let  $\Omega_L$  denote the local domain. From the finite-element approximation  $\mathbf{u}_G^h$  computed in the global problem, we extract  $\mathbf{u}_G^h|_{\partial\Omega_L}$  and use it to constrain the displacements on the boundary of the subproblem <sup>4</sup>. As such, the trial space  $\mathcal{U}^h$  is given by

$$\mathcal{U}^h = \{\mathbf{u}_L^h \in H^1(\Omega_L)^n \mid \mathbf{u}_L^h = \mathbf{u}_G^h \text{ on } \partial\Omega_L\}. \quad (3.29)$$

The function space  $\mathcal{D}^h$  of admissible damage fields is given by

---


$$\mathcal{D}^h = \{d^h \in H^1(\Omega_L) \mid d^h = 1 \text{ on } \mathcal{K}\}, \quad (3.30)$$

<sup>4</sup> In the multi-resolution method of Muixi et al. [69], the displacement boundary conditions near the crack base were released. We did not find this to be necessary in our approach.

where  $\mathcal{K}$  denotes the set of damage-fixed nodes that correspond to the global crack at the beginning of the load step, as described in subsection 3.3.3.1.

The test spaces are given by  $\mathbf{W}^h = H_0^1(\Omega_L)^n$  for the displacements and  $\mathcal{C}^h = \{c^h \in H^1(\Omega_L) \mid c^h = 0 \text{ on } \mathcal{K}\}$  for the damage field. The Galerkin approximation to the problem on the local subdomain is then:

### The spatially discrete form

Find  $\mathbf{u}_L^h \in \mathcal{U}^h$  and  $d^h \in \mathcal{D}^h$ , such that  $\forall \mathbf{w}^h \in \mathbf{W}^h$  and  $\forall c^h \in \mathcal{C}^h$ ,

$$(\nabla \mathbf{w}^h, \boldsymbol{\sigma}_L^h) - (\mathbf{w}^h, \Pi_f^{\Omega_L} p_f^h \nabla d^h) - (\mathbf{w}^h, \mathbf{b}) - \langle \mathbf{w}^h, \mathbf{t} \rangle_{\partial_t \Omega} = 0, \quad (3.31)$$

$$\begin{aligned} \frac{2G_c^h \ell}{c_0} (\nabla c^h, \nabla d^h) + \frac{G_c^h}{c_0 \ell} (c^h, \zeta'(d^h)) + (c^h, 2(d^h - 1) W(\boldsymbol{\epsilon}^+(\mathbf{u}_L^h), 0)) \\ + (c^h, \alpha \Pi_m^{\Omega_L} p_m^h \nabla \cdot \mathbf{u}_L^h) + (\nabla c^h, \Pi_f^{\Omega_L} p_f^h \mathbf{u}_L^h) = 0, \end{aligned} \quad (3.32)$$

where we have used  $(\cdot, \cdot)$  to denote the standard inner product in the  $L^2(\Omega)$  space, and  $\langle \cdot, \cdot \rangle$  to denote its restriction on the boundary. In the above,  $\boldsymbol{\sigma}_L^h$  denotes the discrete stress, given by

$$\boldsymbol{\sigma}_L^h = ((1 - d^h)^2 \mathbb{C} : \boldsymbol{\epsilon}(\mathbf{u}_L^h) - (1 - d^h) \alpha p_m^h \mathbb{I}). \quad (3.33)$$

We employ an alternating minimization scheme to solve the coupled system of equations (3.31)-(3.32). Convergence is measured with respect to the  $L_2$ -norms of the change in the damage  $d^h$  and displacement fields  $\mathbf{u}_L^h$ , using a relative tolerance of  $10^{-4}$ . With this approach, each of the equations becomes linear with respect to its primary variable, simplifying the solution process.

We note that (3.32) does not explicitly include the irreversibility constraint (3.25). Within the multi-resolution scheme, the Dirichlet condition  $d^h = 1$  on the crack set  $\mathcal{K}$  is sufficient to prevent the healing of the fracture surface relative to the initial global crack. It does not, however, enforce irreversibility of the damage throughout

the local subdomain, and it is possible that some crack healing could occur if regions are loaded and unloaded during a single time step. We did not find this to occur for the problems studied in this work, but it is possible that this could arise in more complex cases and the use of a more robust means of enforcing the constraint on the damage would be needed. Options include, for example, the active set solver described in [122].

In terms of the local dissipation function  $\zeta(d)$ , in this work we use  $\zeta(d) = d$  which corresponds to the AT-1 phase-field model of fracture. This is selected due to the fact that it gives rise to a compactly supported damage field and a fully elastic stage prior to damage initiation [123]. When using the AT-1 model, it is necessary to explicitly enforce the constraint  $d^h \geq 0$ , as in some cases, this formulation can lead to negative damage values. In this work, this is effected by invoking a lower threshold on the active part of the strain energy  $W(\boldsymbol{\epsilon}^+(\mathbf{u}_L^h), 0) = 3G_c/8\ell$ , as in [54].

Finally, we note that phase-field models of fracture tend to give rise to a mesh and regularization length dependent critical fracture energy that is larger than  $G_c$  [124]. To account for this, we use a discrete value of  $G_c^h$  that is obtained as a function of the local mesh spacing and regularization length, as

$$G_c^h = G_c \left( 1 + \frac{h_{local}}{c_0 \ell} \right)^{-1}, \quad (3.34)$$

such that the effective critical fracture energy is very close to that of the material.

### 3.3.5 Crack propagation: translating local damage updates into global crack extensions

A key step of the algorithm concerns how changes to the damage in the local subdomain are translated into updates to the crack geometry in the global domain. We provide details of our algorithm for this procedure here. The scheme is presented in the context of a single crack tip that is propagating through the global domain.

Although we do not consider much more complex cases in this work, such as changes in crack topology (due to crack branching or merging), we note that such problems have been examined in other works employing hybrid phase-field approaches. This includes the recent work of Muixi et al. [69], albeit in a purely mechanical context.

At each step in the solution algorithm, in the global problem, we keep track of two geometric entities, namely the global crack tip and the global tip element (Figure 3.5a). The global crack tip is defined by the interior endpoint of the crack. The global tip element is the element that contains the tip on one of its sides, but is not yet “cut” by the crack. In essence, it is the global element just ahead of the propagating crack tip. In the local subproblem, we identify a local version of the crack tip that is obtained from the discrete damage field  $d^h$  (Figure 3.5b and 3.5c). The algorithm to extend the global crack geometry depends on the relative location of the global crack tip, global tip element, and local crack tip, as described below.

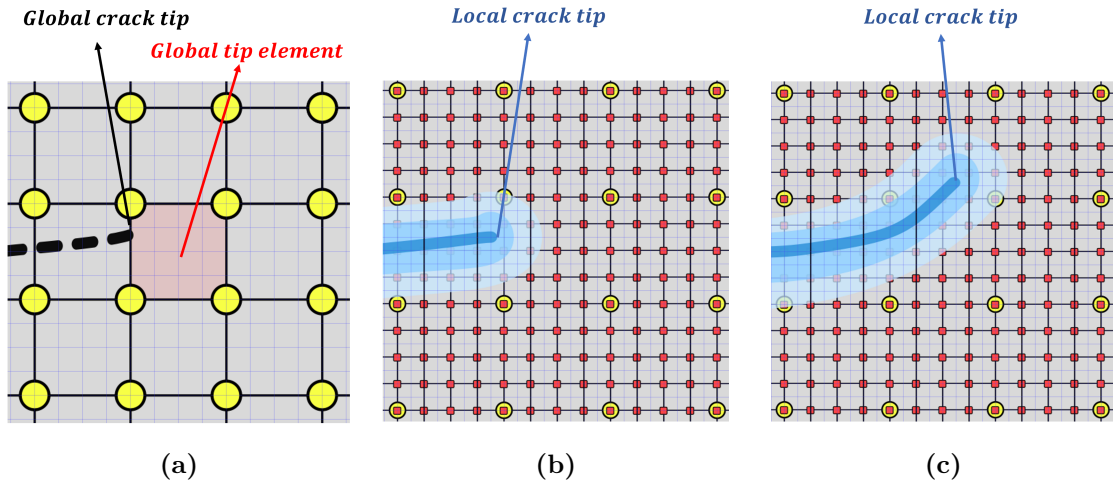


FIGURE 3.5. (a): Illustration of the global crack tip and global tip element. (b) Case when the local tip falls inside the tip element. (c) Case when the local tip falls outside the tip element.

The enrichment strategy described in Section 3.3.2 requires global elements that are completely cut by the crack geometry. As such, any extension of the crack geom-

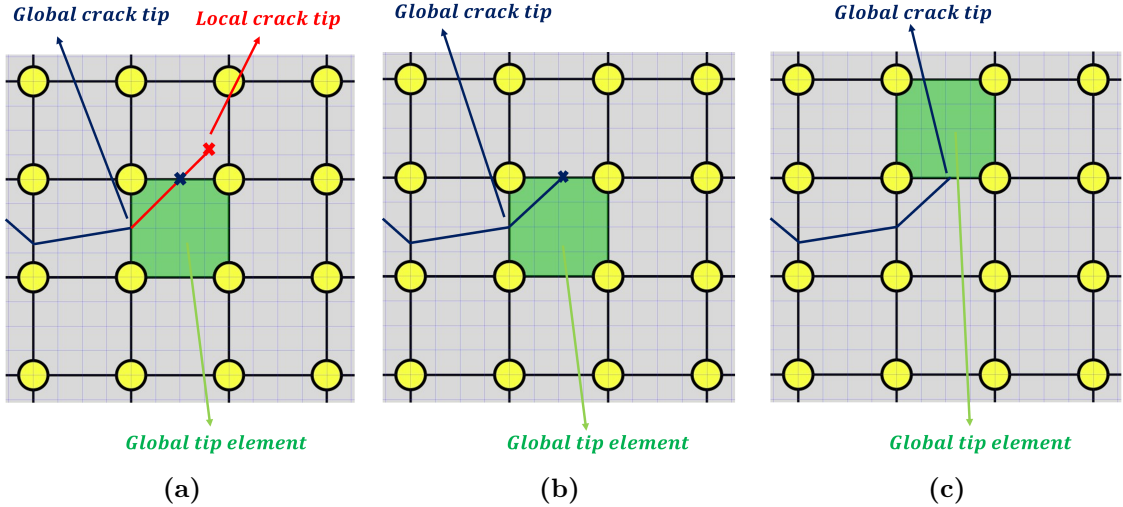


FIGURE 3.6. (a): Construction of the segment connecting global and local tips. (b) New crack segment to be added. (c) Update of the global crack tip and global tip element.

etry at the global scale must correspond to the global tip element being fractured. Accordingly, global crack propagation is triggered whenever the local tip falls outside the tip element. In this case, the new global tip is identified by connecting the current global tip and the local tip. Since the local tip is outside the tip element, a new segment will intersect the perimeter of the tip element exactly once (neglecting the obvious intersection at the current global tip). This process is illustrated in Figure 3.6. Any crack advance beyond this new tip location is neglected at this point, and the algorithm returns to a new global solve with an updated crack geometry.

In general, the problem of extracting a sharp crack front from a diffuse representation is not trivial. When the crack evolution involves complex topological changes, it is particularly difficult[125]. In the numerical examples studied in this Chapter, we take advantage of the relatively simple fracture geometry and predicted crack patterns to simplify this process. In particular, we first identify all elements in the local subdomain with nodes whose damage values are all above a threshold  $d_{tr}$ . A similar approach was proposed in [68]. The local crack tip is taken to be the center

of the element in this set that is farthest from the base of the crack in the local subdomain. The threshold used for this process is taken to be  $d_{tr} = 1 - h_{local}/(2\ell)$ , which is based on the estimate for a damage field near a crack tip given in [61]. In essence, for a phase-field model of fracture, this threshold identifies nodes that are expected to correspond to the peaks of the discrete damage field. For a damage band resolved with a mesh spacing of  $\ell/h_{local} = 4$ , this gives rise to a threshold of  $d_{tr} = 0.875$ .

### 3.3.6 Algorithm summary

Having described the solution strategies for both the global and local problems and the transfer of various quantities, we now detail the algorithm (1) that couples the two problems together to simulate crack propagation. Figure 3.7 provides an illustration of the algorithm. Within each time step (outer loop), the algorithm employs an inner loop that allows the global problem to be updated as soon as any large enough change in the crack geometry is detected in the local subproblem. The inner loop is terminated when the propagation step, described in subsection 3.3.5 does not identify any crack advance. The construction with two nested loops can be viewed as an implicit treatment of the fracture front position, which, according to Lecampion et al. [66] tends to be more accurate and robust, permitting the use of larger time steps.

---

**Algorithm 1:** Solution algorithm for multi-resolution hydraulic fracture

---

Define initial and boundary conditions

$n = 1$

$n_F = endStep$

**while**  $n \leq n_F$  **do**

- $\mathcal{F}_n^1 = \mathcal{F}_{n-1}$
- for**  $1 \leq k \leq maxIter^a$  **do**

  - (1) Solve **Global Problem** and obtain  $\mathbf{u}_G^{k,n}, p_m^{k,n}, p_f^{k,n}$
  - (2) Construct subdomain  $\Omega_L$  and submesh  $\mathcal{T}_L$ . Identify subset of cracked nodes  $\mathcal{K}$ .
  - (3) Prescribe local boundary conditions  $\mathbf{u}_L^h|_{\partial\Omega_L} = \mathbf{u}_G^{k,n}|_{\partial\Omega_L}$  and  $d^h = 1$  on  $\mathcal{K}$ .
  - (4) Construct local pressure fields  $p_m = \Pi_m^{\Omega_L}(p_m^{k,n})$  and  $p_f = \Pi_f^{\Omega_L}(p_f^{k,n})$
  - (5) Solve the **Local Problem** to obtain  $d^k$ .
  - (6) Use  $d^k$  and the propagation step (subsection 3.3.5) to update discrete fracture  $\mathcal{F}_n^k$ .

- if**  $\mathcal{F}_n^{k+1} = \mathcal{F}_n^k$  **then**

  - $n = n + 1$
  - $\mathcal{F}_n = \mathcal{F}_n^k$
  - $\mathbf{u}_G^n = \mathbf{u}_G^{k,n}$
  - $p_m^n = p_m^{k,n}$
  - $p_f^n = p_f^{k,n}$
  - break

- end**

**end**

**end**

---

<sup>a</sup> The index  $k$  is only a dummy variable for this loop that searches for the correct fracture geometry at a given time step.

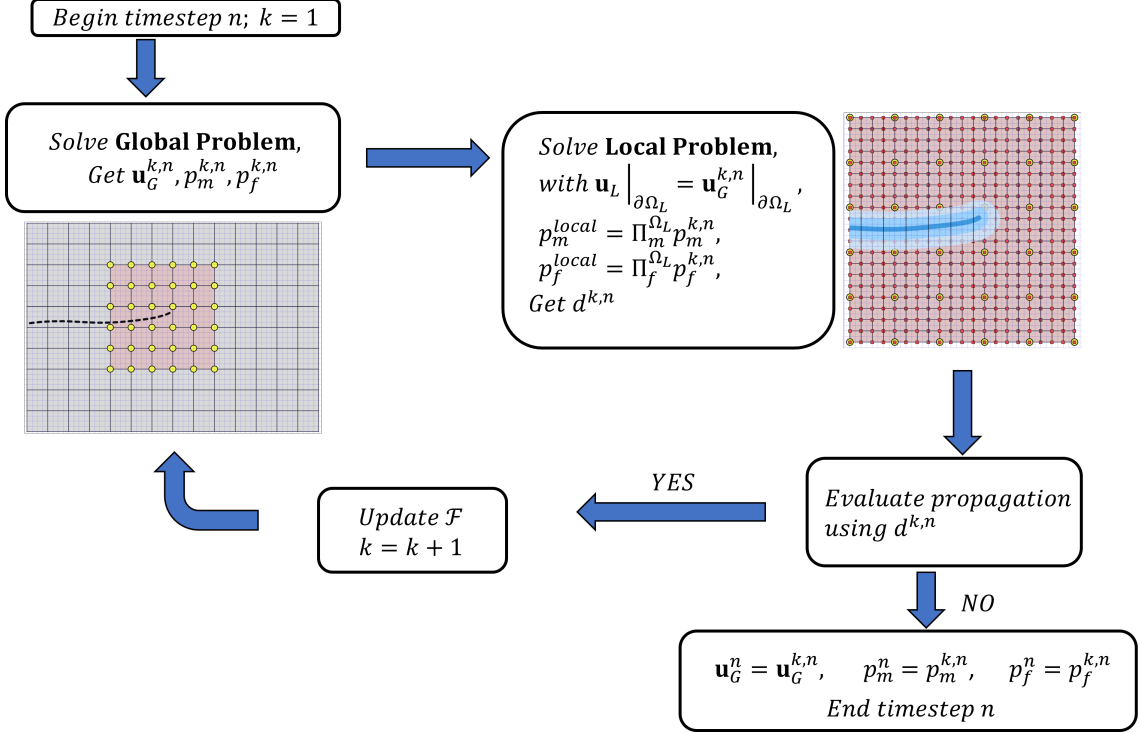


FIGURE 3.7. Multi-resolution solution algorithm.

### 3.4 Numerical Results

We now present the results from various benchmark problems in fluid-driven fracture propagation. The problems range from those in which flow is only present within the cracks to fully coupled problems involving flow in both the matrix and the evolving manifold that is the fracture geometry. With the sole exception of the toughness-dominated KGD problem, all of the results in this section employ the spectral split of the energy, as described in Section 3.2.2.

#### 3.4.1 KGD problems

We begin with the well-known Khristianovic, Geertsma and De Klerk (KGD) problems of hydraulic fracture [20, 19]. The problems concern the propagation of a planar fracture in an infinite, impermeable domain, under the injection of a viscous fluid at a constant rate (Figure 3.8).

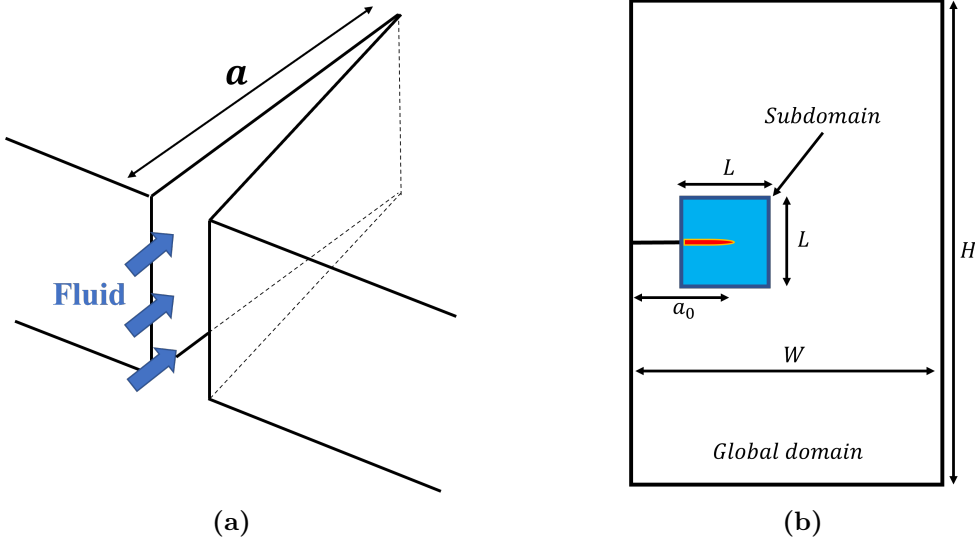


FIGURE 3.8. (a) Schematic of the KGD problem, inspired by [3]. (b) Computational domain for the KGD problem (not to scale).

The response of the system can be characterized by the dimensionless group  $\mathcal{K}$  [90]:

$$\mathcal{K} = \frac{4G_c^{1/2}}{(6\pi^2 E' Q \mu)^{1/4}}, \quad (3.35)$$

where  $E' = E/(1 - \nu^2)$ . Values of  $\mathcal{K} > 4$  correspond to the “toughness dominated regime” in which crack growth is largely controlled by the fracture toughness of the media. By contrast, when  $\mathcal{K} < 1$ , the fracture toughness is relatively small and the fluid viscosity is the main factor controlling the speed of crack growth. In the following, we explore the performance of the multi-resolution algorithm to simulate problems in both regimes.

#### 3.4.1.1 Toughness-dominated regime

The toughness dominated regime is characterized by the creation of new fracture surfaces accounting for almost all of the energy dissipation. In this scenario, the fluid can be considered to be inviscid, which leads to a constant pressure distribution over

the entire crack. The assumption of inviscid flow reduces much of the complexity, allowing for the construction of a simple analytical solution for this problem. Here, we consider a problem in the toughness-dominated regime resulting from the material parameters and settings given in Table 3.1. Using these values in (3.35), we obtain  $\mathcal{K} = 6.54$ .

	Value	Unit
Young's modulus ( $E$ )	16.0	GPa
Poisson's ratio ( $\nu$ )	0.18	—
Fluid viscosity ( $\mu$ )	$1.0 \times 10^{-12}$	GPa . s
Energy release rate ( $G_c$ )	$1.85 \times 10^3$	N/m
Injection rate ( $Q$ )	$1.0 \times 10^{-3}$	m <sup>2</sup> /s
Initial crack size ( $a_0$ )	4	m

**Table 3.1.** Material properties and problem parameters for the toughness-dominated KGD problem

The analytical solution for this problem can be separated into two stages as a function of time. In the first stage, the pressure builds linearly with time and the crack does not propagate, as the pressure is below the critical threshold  $p_{cr} = (G_c E' / \pi a_0)^{1/2}$ . The pressure then reaches the critical value at  $t = t_{cr}$ , after which the crack begins to propagate. In the second stage the propagation is stable, since the amount of fluid injected is finite and crack propagation leads to a pressure drop as the total space available for the fluid to occupy increases.

The solution for the crack length and pressure in the crack can be written as

$$a(t) = \begin{cases} a_0, & t \leq t_{cr}, \\ \left( \frac{E'(Qt)^2}{\pi G_c} \right)^{1/3}, & t \geq t_{cr}, \end{cases} \quad (3.36)$$

$$p(t) = \begin{cases} \frac{t}{t_{cr}} p_{cr}, & t \leq t_{cr}, \\ \left( \frac{E' G_c^2}{\pi Q t} \right)^{1/3}, & t \geq t_{cr}, \end{cases} \quad (3.37)$$

where  $t_{cr} = (\pi G_c a_0^3 / Q^2 E')^{1/2}$ . A derivation of this solution can be found in Yoshioka [61].

For simulations using the multi-resolution scheme, a computational domain of size  $W \times H = 30 \text{ m} \times 240 \text{ m}$  is used (Figure 3.8b). According to [126], this domain size should be sufficiently large to yield a good approximation to an infinite plane. We first report results using a sub-domain size of  $L \times L = a_0 \times a_0$ . The sensitivity of the results to the choice of sub-domain size will be discussed later in this subsection.

In what follows, we report results from a refinement study. In particular, we report results for three different regularization lengths of decreasing value, beginning with  $\ell = a_0/15$ . As the regularization length is decreased, we maintain a mesh size in the subdomain of  $h_{local} = \ell/4$ . This allows the finite-element approximation to sufficiently resolve the regularized fracture band. We also note that the effective fracture toughness in the computational problem depends on  $h/\ell$  [61]. In the global domain, we maintain the mesh spacing at the ratio of  $h_{global} = 3h_{local}$ . For the coarsest global mesh, this translates into roughly 20 elements over the span of the initial crack geometry. This level of resolution is consistent with those found to be sufficient for resolving pressurized cracks using the Embedded Finite Element Method, in Cusini et al. [5].

The results obtained with the multi-resolution scheme are compared to the analytical solutions 3.36 and 3.37 in Figures 3.9a and 3.9b. We note the overall good match between the simulation results and the analytical solution, as well as the convergence of the results towards 3.36 and 3.37 when  $\ell$  decreases. Although this problem is relatively simple as the matrix is assumed to be impermeable, it does test the coupling between the global and the local domains and verifies that the phase-field method, even when used only in a vicinity of the crack tip, can still provide accurate predictions of fracture propagation. Although the spectral split was not employed for this problem, we did examine the results using it. Qualitatively they

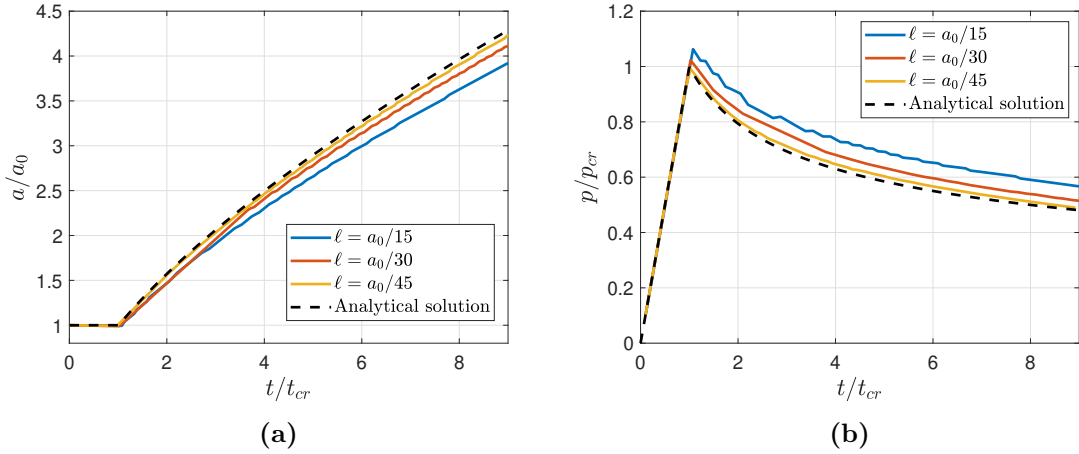


FIGURE 3.9. Comparison of numerical results and analytical solution for the toughness-dominated KGD problem: (a) crack length vs. time and (b) pressure vs. time.

were found to be very similar, with slightly less accuracy in the calculated values of the critical pressure.

We now examine the sensitivity of the results to changes in the subdomain size. This is accomplished by fixing the sizes of the global and local meshes as well as the regularization length, and varying only  $L$  in Figure 3.8b. In particular, we fix the regularization length to  $\ell = 0.13$  m and vary the sub-domain size between  $15\ell$  and  $45\ell$ .

Figures 3.10a and 3.10b provide the results for the pressure and crack length as a function of time, for the various choices of subdomain size. Table 3.2 shows the error in the computation of the crack length relative to the analytical solution. The error is taken as an average over the time range, starting at the beginning of propagation.

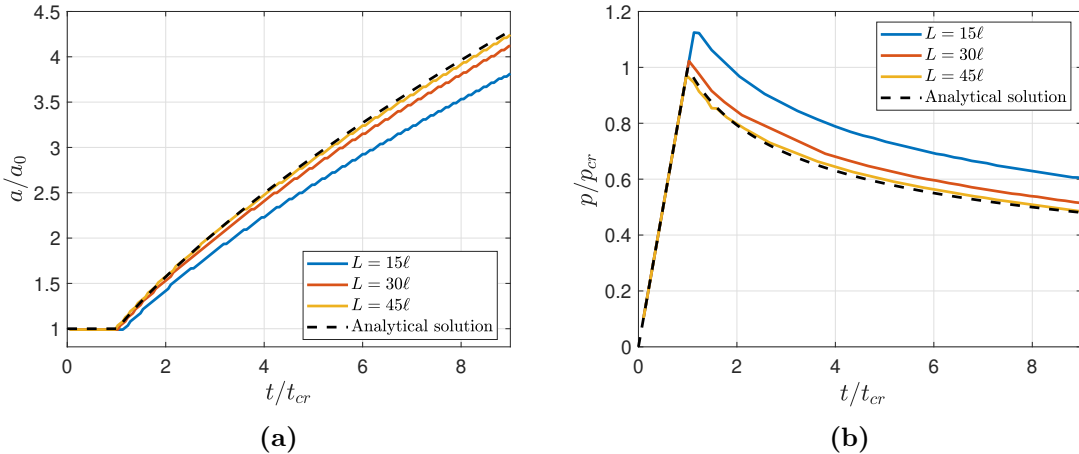


FIGURE 3.10. Study of the effects of subdomain size on the results of the toughness-dominated KGD problem: (a) influence on predicted crack length and (b) predicted pressure.

Subdomain size	Relative error
$L = 15\ell$	11.5%
$L = 30\ell$	3.3%
$L = 45\ell$	1.1%

**Table 3.2.** Effect of subdomain size on the relative error in the crack length.

The results indicate that the error reduces as the subdomain size is increased. In this particular study, both the global and subdomain meshes are fairly refined, and so the improvement in accuracy as  $L$  increases is not likely due simply to better resolution in the local subdomain. Rather, it may be due to the fact that the two problems are coupled through the global displacements applied to the subdomain boundary. As the subdomain size is increased, the boundary of the subdomain moves farther from the crack tip singularity, and one would expect a better correspondence between the displacement fields obtained from the global problem and those obtained using a phase-field approximation over the entire domain. Furthermore, as the global displacements are held fixed until the regularized crack advances sufficiently far, there is some sensitivity of the proximity of the regularized crack tip to the subdomain

boundary.

In more general cases, one would expect the subdomain mesh to be at quite a bit higher resolution than the global mesh. Since the phase-field problem also requires several iterations in the alternate minimization scheme, problems are expected to become much more computationally expensive as  $L$  is increased. As a result, a trade-off between accuracy and computational cost is to be expected. In general, one should select a subdomain size that strikes a balance between being large enough to capture the crack evolution and small enough to render the overall calculation efficient.

#### 3.4.1.2 Viscosity dominated KGD problem

We now consider a case in which the choice of parameters gives rise to conditions wherein the energy dissipation is dominated by viscous dissipation. In particular, we consider the material properties and problem parameters provided in Table 3.3. Consistent with (3.35), these values give rise to  $\mathcal{K} = 0.57$ , a result that is clearly within the viscosity-dominated regime.

	Value	Unit
Young's modulus ( $E$ )	0.17	GPa
Poisson's ratio ( $\nu$ )	0.20	—
Fluid viscosity ( $\mu$ )	$1.0 \times 10^{-10}$	GPa . s
Energy release rate ( $G_c$ )	21	N/m
Injection rate ( $Q$ )	$1.0 \times 10^{-3}$	m <sup>2</sup> /s
Initial crack size ( $a_0$ )	4.0	m

**Table 3.3.** Material properties and problem parameters for the viscosity-dominated KGD problem

In this scenario, the toughness of the medium can be neglected, and the fracture evolution is effectively dictated by the motion of the fluid front. In this case, the pressure varies with time and space over the length of the fracture surface. Although this problem does not include a pressure field in the matrix, it bears emphasis that it does require the transfer of the pressure field in the fracture from the global scale

to the phase-field problem in the subdomain. As such, it serves as a test of that aspect of the multi-resolution scheme. The presence of dynamic terms in the fluid equation also implies the need for a discretization with sufficiently accurate temporal resolution, and in what follows we examine the sensitivity of the results to the choice of the time step size.

Once again, consider a computational domain with dimensions  $W \times H = 30 \text{ m} \times 240 \text{ m}$ . The sub-domain size is taken as  $L \times L = a_0 \times a_0$ , and the regularization length is taken to be  $\ell = a_0/15$ . In contrast to what we observed for the toughness regime, we note that the results to the viscosity-dominated problem were found to be largely insensitive to the choice of the regularization length, provided that  $\ell < a_0/10$ . This is not surprising, given that the phase-field subproblem only serves to propagate a crack that has effectively zero toughness.

In what follows, we report results using mesh spacings in the local and global domains of  $h_{local} = \ell/4$  and  $h_{global} = 3h_{local}$ . As an initial condition, the pressure field is prescribed to match the analytical solution. We report on the temporal convergence of results obtained using fixed time steps, beginning with  $dt_0 = 0.5\text{s}$ . As (discrete) negative pressures arose in our simulations, the phase-field model was modified to account for a tension-compression asymmetry. In particular, consistent with the model described in Miehe et al. [89], the strain energy density was split into active and inactive parts, and only the “tensile” part was degraded with the damage.

Figure 3.11 compares the analytical solutions for the crack length and inlet pressure to the model-based simulation results for a sequence of decreasing time steps. The initial time ( $t_0 = 8.5 \text{ s}$ ), initial inlet pressure ( $p_0 = 40 \text{ kPa}$ ) and initial crack size ( $a_0 = 4 \text{ m}$ ) were used to render the results dimensionless. The particular values of  $t_0$  and  $p_0$  were chosen in order to make our initial state a snapshot of the analytical solution. Overall, the good agreement between the results indicates that the

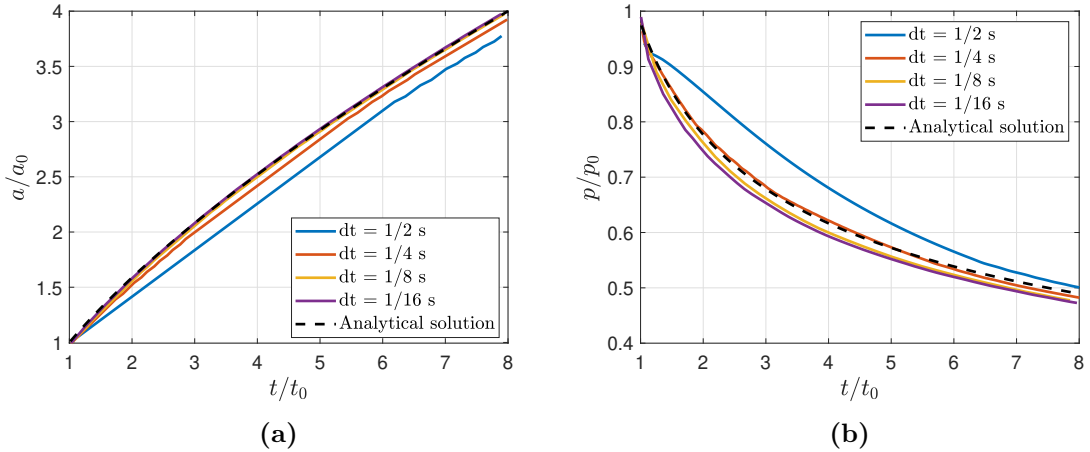


FIGURE 3.11. Numerical results and analytical solution for the viscosity-dominated KGD problem: (a) crack length vs. time; and (b) inlet pressure vs. time.

multi-resolution scheme is capable of handling a viscosity-dominated case.

The results for the crack length show an excellent agreement with the analytical solution as the time step is decreased. The results for the inlet pressure (Figure 3.11b) appear to converge to a trajectory that is slightly offset from the analytical solution as the time step is decreased. This relatively small discrepancy can be explained by the presence of a minimum aperture that is assigned to the newly-initialized finite volumes in the flow solver. As explained in [39], this is necessary to preserve the stability of the scheme when new crack segments are added. The recent work by Jin et al. [127] proposes a method for removing this parameter by employing partially fractured elements. The incorporation of similar modifications in the context of the multi-resolution scheme is the subject of future work.

### 3.4.2 Poroelastic problem with coupled matrix-fracture flow

We now examine a problem in which the matrix is permeable and there is a coupling between the fluid flow in the fracture, fluid flow in the matrix, and crack propagation. A schematic of the problem is shown in Figure 3.12. It corresponds to a rectangular

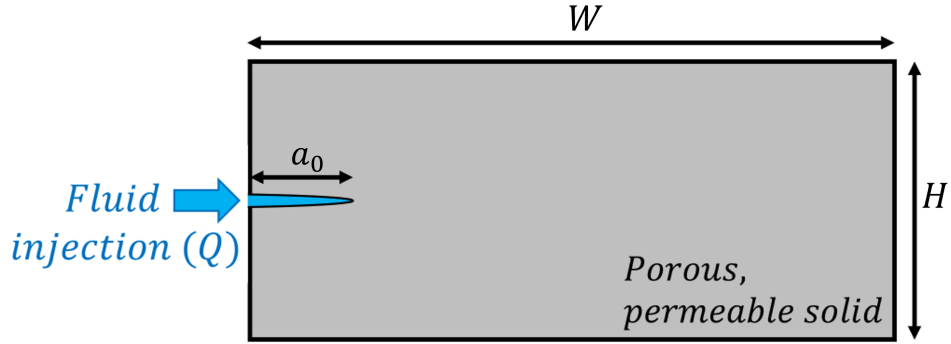


FIGURE 3.12. Geometry and notation for the coupled poroelastic-fracture problem.

domain subject to the injection of a viscous fluid at the mouth of an initial fracture. The fluid injection rate  $Q$  is assumed to be constant, and the displacement in the normal direction is fixed on all sides of the domain.

Although this problem is relatively simple, to our knowledge an analytical solution is not available. In what follows, we therefore compare our results to those that are obtained using an existing phase-field method for hydraulic fracture. In particular, we compare our results to those obtained using the method described by Miehe and Mauthe [53, 54]. This is arguably one of the simpler methods available for this class of problems, combining the equations for phase-field fracture, Biot's theory of linear poroelasticity in the matrix, and lubrication theory for fluid flow within fractures.

The model assumes that a Darcy model of flow holds in the matrix, with isotropic permeability. In the fractures, a lubrication flow model is assumed. The transition between the two flow regimes is effected through the use of a permeability tensor that varies as a function of the crack aperture and orientation. In particular, the permeability tensor  $\kappa$  is given by

$$\kappa = \kappa_0 + d^\xi \frac{w_n^2}{12} (\mathbf{I} - \mathbf{n}^d \otimes \mathbf{n}^d), \quad (3.38)$$

$$w_n = h(\mathbf{n}^d \cdot \boldsymbol{\epsilon} \cdot \mathbf{n}^d), \quad (3.39)$$

in which the normalized gradient  $\mathbf{n}^d = \nabla d / |\nabla d|$  approximates the normal to the crack plane. In the above,  $\kappa_0$  is an isotropic part of the permeability that accounts for the undamaged permeability of the matrix,  $w_n$  is the crack's normal aperture, and  $\xi$  is a weighting exponent. The weighting exponent concentrates the effects of the second term in 3.38 to areas where  $d \approx 1$ . Consistent with the work of Miehe and Mauthe [53, 54], we use  $\xi = 50$ .

	Value	Unit
Young's modulus ( $E$ )	16.0	GPa
Poisson's ratio ( $\nu$ )	0.18	-
Fluid viscosity ( $\mu$ )	$1.0 \times 10^{-12}$	GPa . s
Energy release rate ( $G_c$ )	3.67	N/m
Biot coefficient ( $\alpha$ )	0.79	-
Rock permeability ( $\kappa_0$ )	$1.0 \times 10^{-13}$	m <sup>2</sup>

**Table 3.4.** Material properties for poroelastic problem

	Value	Unit
Phase-Field reg. length ( $\ell$ )	0.2	m
Subdomain size ( $L$ )	4.0	m
Domain width ( $W$ )	30	m
Domain height ( $H$ )	10	m
Initial crack size ( $a_0$ )	4.0	m
Injection rate ( $Q$ )	$1.0 \times 10^{-3}$	m <sup>2</sup> /s

**Table 3.5.** Problem settings

The material properties used in this problem are given in Table 3.4, while the problem and model parameters are provided in Table 3.5. The results reported in this section rely on the use of an eigen-decomposition of the strain energy, as described in Miehe et al. [89]. The subdomain size for the multi-resolution method was chosen to be proportional to the initial crack size, or  $a_0 \times a_0$ . The problem

was discretized spatially using a uniform mesh in the local domain with  $h_{local} = \ell/4$ , while  $h_{global} = 3h_{local}$  was used in the global domain. For the temporal discretization, a uniform time step of  $dt = 0.125$  s was used. This level of spatial and temporal discretization was found to yield results that were sufficiently converged.

An important difference between the phase-field formulation used in Miehe and Mauthe [53, 54] and that employed in the current multi-resolution method concerns the use of pressure-dependent driving forces. We draw the reader's attention to the terms involving the pressure fields  $p_m$  and  $p_f$  in the evolution equation (3.22) for the damage field. In our studies of the KGD problem, we found these terms necessary to include in order to obtain sufficiently accurate simulations. We refer to these terms as "driving pressures" as the pressure fields contribute directly to the evolution of the damage field. Importantly, the phase-field formulation of Miehe and Mauthe [53, 54] does not include these terms in the damage evolution equation. Accordingly, in what follows we find it useful to compare results from Miehe and Mauthe [53, 54] to those obtained using our multi-resolution method with and without the driving pressures.

Results for the crack length and inlet pressure as a function of time are provided in Figure 3.13. Contour plots of the damage and pressure fields for the multi-resolution scheme and the full phase-field formulation are provided in Figure 3.14. Despite the numerous differences in the models, the results obtained with the multi-resolution compare very favorably to those obtained using our implementation of the phase-field fracture model [54]. This is particularly the case when the driving pressures are removed from the multi-resolution method, such that the two phase-field models are as close as possible. At early times the crack remains stationary, as the pressure at the inlet increases. At some point the pressure near the crack tip reaches a magnitude that is sufficient to give rise to crack propagation. After crack propagation begins,

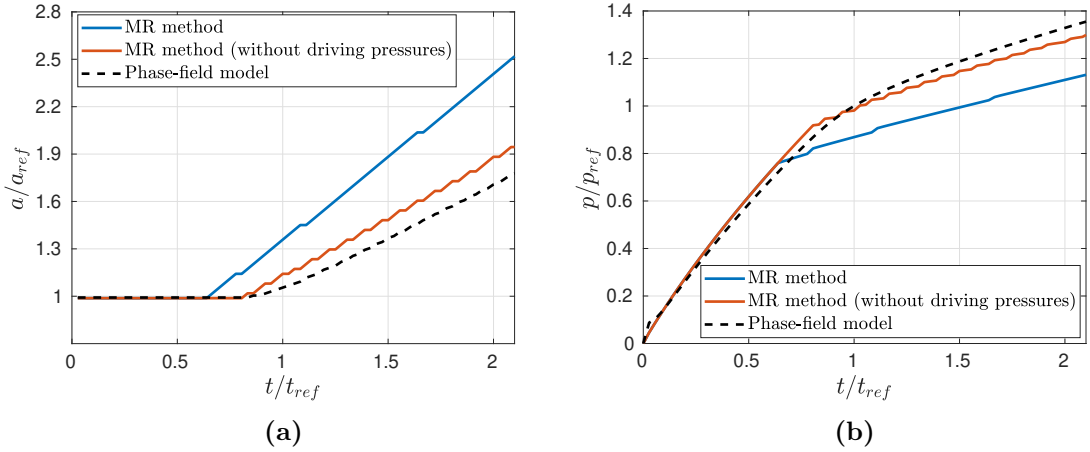


FIGURE 3.13. Results from the fully coupled poroelastic-fracture problem for the multi-resolution method (with and without driving pressures) and a standard phase-field model: (a) crack size over time, (b) inlet pressure. The time for crack propagation ( $t_{ref}$ ) in the phase-field model and the corresponding inlet pressure ( $p_{ref}$ ) are used as references for the dimensionless charts above.

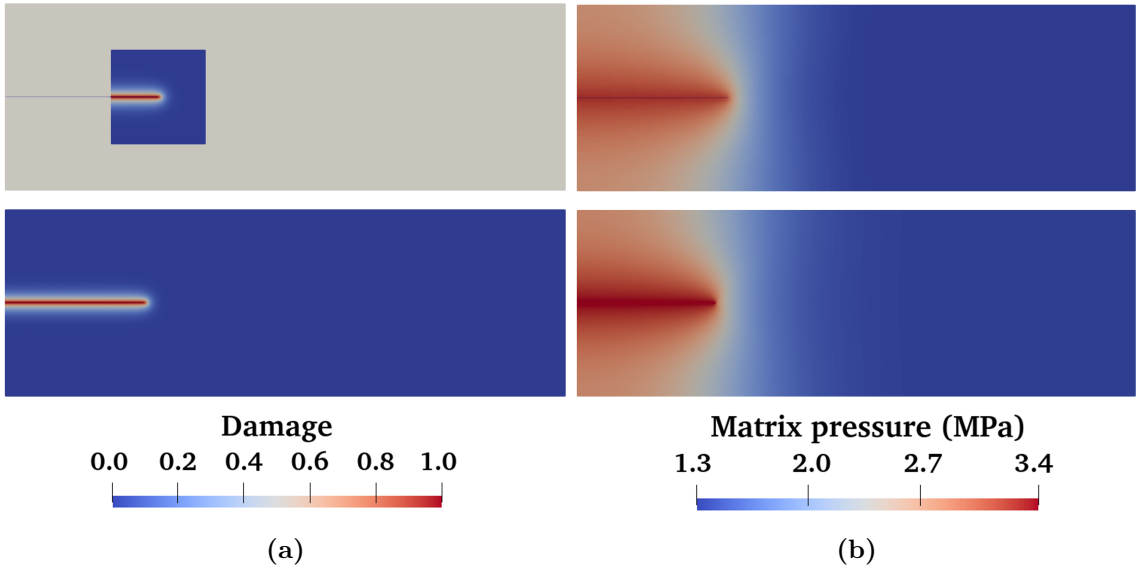


FIGURE 3.14. Fields from the coupled poroelastic-fracture problem, taken at the end of the simulation, contrasting results from the multi-resolution scheme without the driving pressures (top row) to those obtained using a standard phase-field model of fracture in poroelastic media (bottom row). (a) Contour plots of the damage field. (b) Contour plots of the pressure field.

the rate of pressure increase begins to decrease with time, as crack growth allows for additional fluid to be accommodated within the fracture. Clearly the phase-field subproblem with a frozen pressure field that acts effectively as a body force is still capable of simulating crack propagation, even when there is flow in the crack and the matrix. It bears emphasis that the multi-resolution scheme does not need to rely on estimations such as 3.38,3.39 to extract an approximation to the aperture from the regularized crack geometry.

### 3.4.3 Propagation around an inclusion

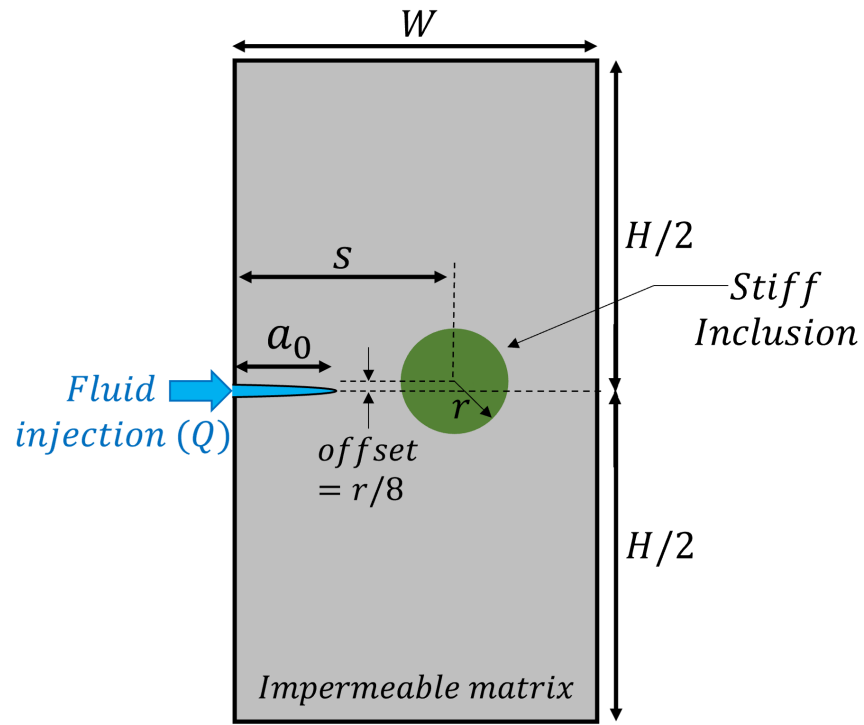


FIGURE 3.15. Geometry for the inclusion problem.

We now consider a problem that gives rise to a non-planar crack evolution. Specifically, we investigate the effects of a stiff inclusion on the trajectory of a hydraulically-driven fracture in an impermeable medium. The problem setup is shown in Figure 3.15. A circular inclusion of radius  $r$  is placed in a rectangular domain, at a distance

$s$  from the left boundary, and slightly offset from the axis of symmetry. The inclusion is assumed to have properties that are identical to the matrix, with the exception of the Young's modulus. An initial crack of size  $a_0$  is placed in the left boundary and a fluid is injected at a constant rate  $Q$ . The complete set of material properties and geometric parameters are listed in Tables 3.6 and 3.7.

	Value	Unit
Young's modulus ( $E$ )	9.0	GPa
Poisson's ratio ( $\nu$ )	0.25	—
Fluid viscosity ( $\mu$ )	$1.0 \times 10^{-12}$	GPa . s
Energy release rate ( $G_c$ )	$2.5 \times 10^6$	N/m

**Table 3.6.** Material properties for inclusion problem

	Value	Unit
Phase-Field reg. length ( $\ell$ )	0.4	m
Subdomain size ( $L$ )	4.0	m
Domain width ( $W$ )	20	m
Domain height ( $H$ )	40	m
Initial crack size ( $a_0$ )	4.0	m
Injection rate ( $Q$ )	$1.2 \times 10^{-1}$	$\text{m}^2/\text{s}$

**Table 3.7.** Problem settings

Simulations using the multi-resolution scheme were conducted for three different values of inclusion stiffness, with  $h_{local} = \ell/6$  in the local domain, and  $h_{global} = 3h_{local}$  in the global domain. The objective was to test how the stiffness of the inclusion influenced the crack trajectory. Consider the following two limiting cases. When the inclusion is just slightly stiffer than the matrix, one would expect the crack trajectory to remain straight. At the other extreme, when the inclusion is much stiffer, one would expect the crack to propagate around it.

The crack paths predicted by the multi-resolution scheme are shown in Figure 3.16. The deformed meshes are shown with displacements exaggerated to highlight the crack trajectories. As expected, for an inclusion with much higher stiffness,

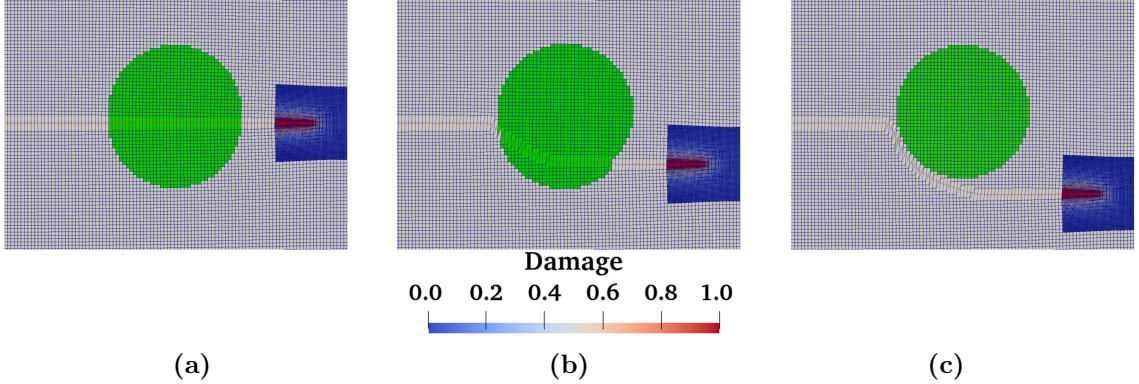


FIGURE 3.16. Crack paths for the inclusion problem: (a) 2X stiffer inclusion; (b) 7X stiffer inclusion; and (c) 15X stiffer inclusion.

the crack propagates around it. By contrast, when the stiffness of the inclusion is relatively close to that of the matrix (2X case), the trajectory remains nearly straight. Interestingly, for an intermediate value, where the inclusion is 7 times stiffer than the matrix, the crack trajectory gets deflected, but still goes through the inclusion.

The pressures at the injection point are plotted as a function of time in Figure 3.17. Due to the very high toughness of the material, they are almost uniform over the crack. For this problem, we did not observe much sensitivity of the results to the choice of time step size. By analyzing these curves, we can identify several different stages for this problem. At early times before any crack propagation begins, we observe a linear increase in pressure with time. Then, as we reach a certain pressure, which we denote as  $p_{ref} = 60$  MPa, straight crack propagation starts and proceeds until the tip approaches the inclusion. Due to the higher stiffness of the inclusion, the crack arrests and pressure builds up again until it reaches a level that is sufficient to allow propagation to continue. This is accompanied by a pressure drop that is most pronounced for the higher-stiffness inclusion cases.

This problem highlights several capabilities of the multi-resolution scheme, such as the simple handling of crack curving as well as changes in the crack speed, including crack arrest. Although we are not aware of any analytical solution for problems like

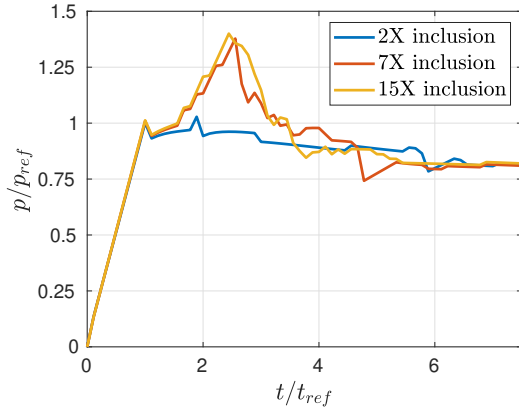


FIGURE 3.17. Inlet pressure as a function of time for the three inclusion problems, corresponding to inclusions with different stiffnesses. The reference values of the pressure  $p_{ref}$  and time  $t_{ref}$  were defined as the minimum pressure that led to fracture growth and the associated time, considering the simulated injection rate.

this, the results we have obtained appear to make sense qualitatively.

# 4

## Extending the Multi-Resolution Approach to Three Dimensions

### 4.1 Introduction

While two-dimensional simulations, based on the multi-resolution algorithm proposed in the previous chapter, can be useful to study fundamental processes in hydraulic fracturing, realistic systems are almost always three-dimensional. Therefore, an extension of the approach to 3D is certainly the most natural next step to be taken.

This chapter then proposes a new propagation algorithm for the multi-resolution approach that is suited for planar fractures in three dimensions. This algorithm is implemented in the HPC solver GEOS [37, 38, 39] in a fruitful collaboration with the Lawrence Livermore National Laboratory.

The chapter begins with a brief recap of the multi-resolution algorithm and moves on to the detailed description of the new propagation algorithm for the case of planar fractures. Illustrative examples are then presented, including in-plane merging of two-penny shaped cracks. In the end, in Section 4.5, the extension to non-planar

fractures in 3D is discussed, and the prototype of an algorithm is presented. A simplified version of this algorithm is implemented and tested in a 2.5D problem with a curved crack. While it addresses some of the challenges, it requires further work to handle the general case.

## 4.2 Theory

In Chapter 3, the mathematical model for single-phase fluid-driven fracture is described in Section 3.2. In what follows, this same model is assumed, as all derivations are independent of the system's dimensionality as well as fracture shapes. Since the multi-resolution framework is employed, two coexisting descriptions are used. In a global domain, cracks are assumed to be represented by two-dimensional surfaces embedded in the 3D domain and the governing equations and boundary condition are those from (3.1) - (3.16), which assume a fixed fracture geometry. In the local domain, the fracture problem is treated with a variational phase-field formulation, given by (3.21)-(3.25) which assume flow quantities to be fixed.

A more detailed discussion of the motivation and fundamentals of the multi-resolution method is provided in Section 3.3. This type of approach is particularly interesting for simulating fluid-driven fracture due to the presence of a discrete fracture in the global level, which simplifies the computation of the fracture apertures that must be coupled to the fluid problem. If a pure phase-field description is used, extracting these apertures becomes a challenging task. In addition to that, a multi-resolution approach, can also alleviate the computational cost that comes with the highly-refined grids needed to solve phase-field problems. This becomes a remarkable limitation in the context of hydraulic fracturing since the length of fractures is usually of the order of kilometers.

An attentive reader will realize that the only part of the multi-resolution algorithm proposed in Chapter 3 that is not extendable to three-dimensions is the

propagation step described in the subsection 3.3.5. In this part of the algorithm, the crack tip location is extracted from the damage field in the local problem and used to inform the global problem how to advance the crack. The concept of a crack tip does not exist in three-dimensions (it becomes a fracture front). In addition to that, while in 2D it is always possible to connect line cuts (which are just line segments) to form an approximation to the crack geometry, in 3D these become planar cuts, which may fail to connect on element boundaries, as shown in Figure 4.1. Therefore, the way crack propagation is handled needs to be revisited in order to extend the method to three-dimensions.

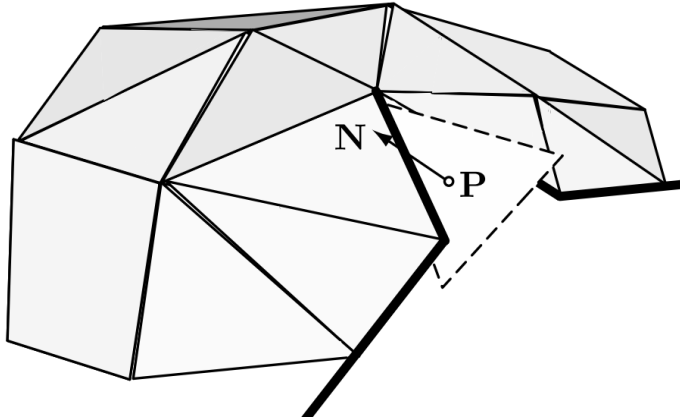


FIGURE 4.1. Illustrative example of a 3D surface with gaps, because surface elements do not connect smoothly. Extracted from [4].

The first extension discussed in this chapter deals with the case of planar fractures in 3D. The main challenge here consists of tracking the entire fracture front and evolve it according to the damage field computed in the local problem. This is done by defining a discrete set of crack front elements which are investigated for damage throughout the problem execution. The construction of this layer of front elements ahead of the crack is important to preserve the accuracy of the solution, because the absense of a fluid solver in the local problem can lead to spurious unstable solutions<sup>1</sup>.

---

<sup>1</sup> In hydraulic fracture, the fracture propagation is in general stable because the pressure drops as

### 4.3 Algorithm for planar fractures

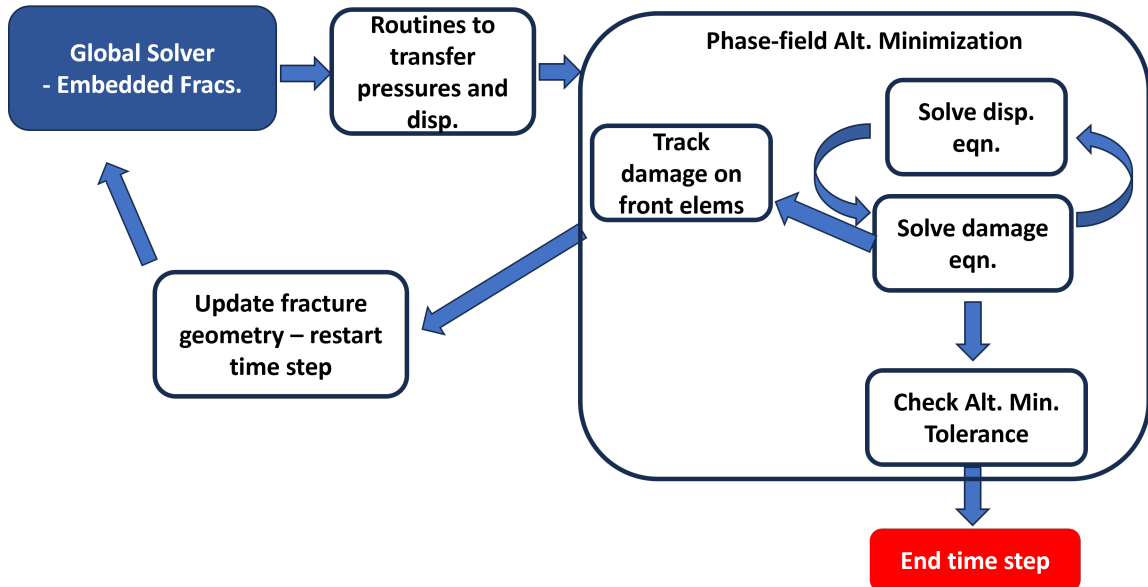


FIGURE 4.2. Multi-resolution solution algorithm.

A high-level description of the propagation algorithm for planar fractures in 3D is shown in Figure 4.2. It summarizes each of the steps involved in the solution procedure for a single time-setp. The process begins with the solution of the global problem (i.e, the box colored in blue in 4.2). As pointed out in chapter 3, the algorithm is agnostic with respect to the numerical methods employed. The approximate fields for pressure and displacements are then transferred to the local problem, as explained in the steps (3) and (4) of Algorithm 3.7.

In the 2D algorithm, one would now move to the solution of the local problem with an alternate minimization approach and only then check for fracture propagation. In the proposed 3D algorithm, this is changed and a damage tracking function is launched in parallel with the damage solver. This function checks the amount of damage in the elements of the fracture from (which is described in detail in subsection

---

the fracture volume increases. However, this effect only appears when the fluid solver is coupled to fracture propagation.

4.3.1). Different measurements of damage can be employed, and they will likely depend on the discretization method employed. A simple one, which works well for planar fractures in structured grids is the volume of damage, which is defined as the total volume of subdiscretization' elements with damage above a threshold (usually around 0.9). This approach is effective since, for planar fractures aligned with structured grids, the fracture area on each element can be predicted beforehand. This simplified criteria is used in the example problems shown in Section 4.4. It is discussed in more detail, together with a more general approach in subsection 4.3.2.

If any of the front elements is identified as being cracked (i.e, the level of damage on it is very high), the alternate minimization iterations are halted. The geometry of the discrete fracture in the global is then updated. This update consists of the addition of a planar cut in this cracked element, followed by an advance in the fracture front. This in turns lead to an advance in the local domain.

If multiple front elements are cracked, this process is done for all of them. The current time-step is then re-launched. Convergence is achieved when the alternate minimization procedure reaches a prescribed tolerance without triggering the fracture propagation. When that happens, an equilibrium state is obtained and the time-step can be advanced.

#### 4.3.1 *Fracture front construction*

The fracture front plays an important role in the propagation step. It greatly reduces the computational expense associated with the inspection of damage in the global elements while also serving to indicate a reference position to place the subdomains as the crack advances. It's construction happens during the initial discretization of the fracture in the global domain. One goes over all fractured elements and among its neighbors, adding to the front those elements that share a fractured face (but are not yet fractured) with the fractured ones (Figure 4.3). This step is repeated every

time the global fracture geometry is updated (i.e new fracture cells are inserted).

Figure 4.4 shows the fracture front for a penny shaped crack. Figure 4.5 shows the sequence of steps involved in the fracture propagation process, including the update of the fracture front.

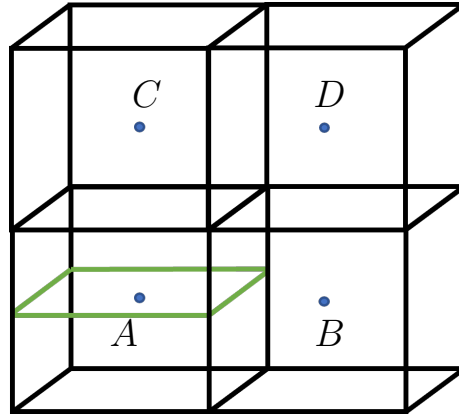


FIGURE 4.3. Fractured element A and some of its neighbors. Element B is assigned to the front because the face it shares with A is fractured. C is not on the front because the face it shares with A is not fractured. D is not on the front because it does not share a face with a fractured element.

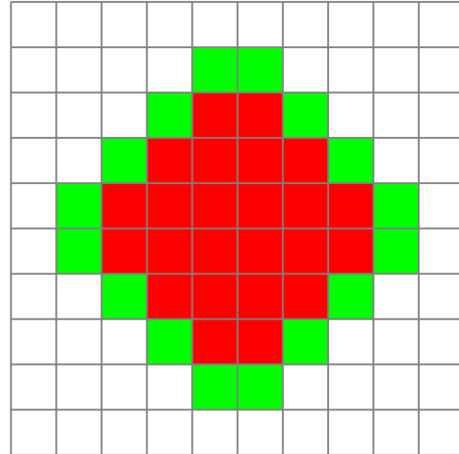
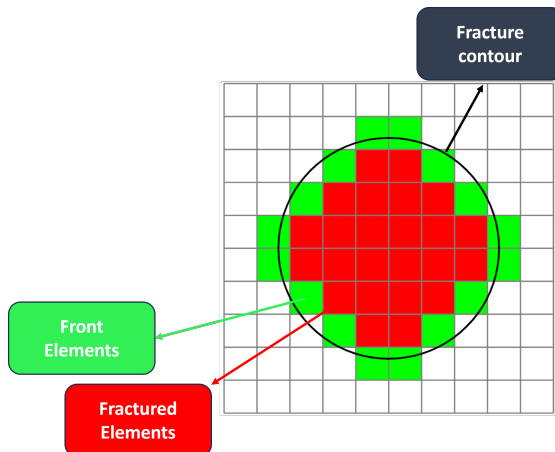
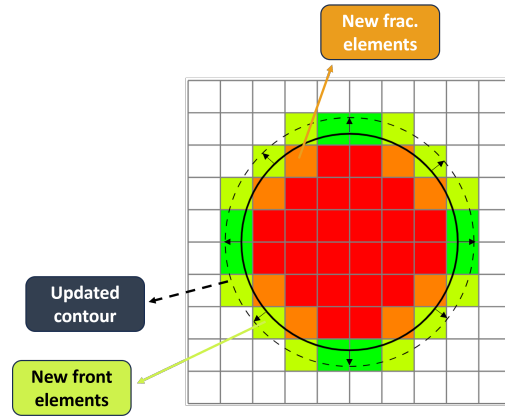


FIGURE 4.4. Penny shaped crack discretized in a coarse grid. Red elements represent the fractured elements (which contain EFEM enrichments). The fracture front elements are shown in green.

(a) Beginning of time step. The phase-field fracture is shown as a counter to facilitate the visualization. As in 4.4, green elements represent the front and red the discrete fracture.



(b) After a few iterations in the local problem, the phase-field advances and some front elements (now in orange) are identified as fully damaged. They will be fractured and their neighbors in light green will be added to the front.



(c) Final configuration after the updates. Since the global fracture changed, the time-step must be relaunched.

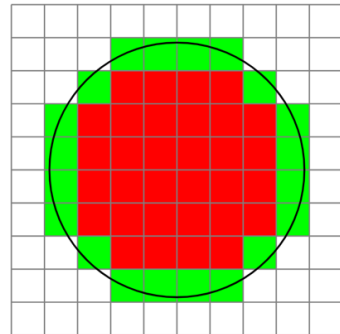


FIGURE 4.5. Sequence of steps performed during crack propagation.

### *4.3.2 Tracking damage in the fracture front elements*

The process of tracking the damage in the front elements also deserves a more detailed explanation. First, a simplified criterion suitable for planar cracks in structured grids is detailed. This is the one that is used in the preliminary results shown next. Then, a more general approach that can be used for unstructured meshes is described.

#### *4.3.2.1 Volume of damage criterion*

For this criterion, consider a structured grid, aligned with the coordinate axis and with the fracture planes. Suppose that a given element in the global domain has dimensions  $H_x, H_y$  and  $H_z$  whereas the local one has  $h_x, h_y$  and  $h_z$ .

This criterion begins by first computing the cross sectional area of that element along the fracture plane. For example, for a fracture whose normal is in the x direction, one gets  $H_y H_z$ . This is only possible when the structured grid is aligned with the fracture (either in  $x, y$  or  $z$ ).

Then, assuming that the fully damaged region of a phase-field fracture consists of a single element across the damage band width, the volume of the fully-cracked region can be estimated to be  $h_x H_y H_z$  when the damage completely crosses the element. So, to check if that has happened, the volume of local elements with damage above a threshold (consider 0.9) is computed from the local problem solution. A global element is then considered fractured if this volume reaches  $h_x H_y H_z$ .

This method contains multiple limitations, such as the need for planar fractures aligned with a structured grid and also the hypothesis that the damage band has a single fully degraded element along its width. However, in many practical applications, the fractures are indeed assumed to be parallel to each other and structured grids are also preferred, as they can substantially reduce memory use.

#### 4.3.2.2 Topological criterion

An alternative method to circumvent these limitation is inspired by [69]. It consists of evaluating the damage field in the edges of an element. It assumes that a fractured element has at least three fractured faces and that a fractured face is cut on two of its edges.

For each global element in the crack front, the damage field, computed in the local mesh, is inspected on every edge. If damage above a threshold (typically 0.9 or 0.95) is identified in a given edge, that edge is considered cut. If any face contains two cut edges, it is marked as cut. An element is then marked as fracture when at least three of its faces are cut.

This criteria circumvents some of the limitations of the simplified one, removing the need for structured grids. It is also applicable to nonplanar fractures as well. However, it is not perfectly robust and certain relative configurations between the damage field and the global element in the front can lead to unexpected results. This will be shown in Section 4.5 that discusses the case of nonplanar fractures.

## 4.4 Numerical examples

In this Section, a two example problems computed with the aforementioned method are presented. These examples illustrate the main capabilities of the approach, but also serve to demonstrate some of the limitations. They all consist of hydraulic fracture propagation in a poroelastic medium involving different fracture configurations that are relevant to practical fracking applications. The main goal is to ensure that the proposed algorithm supports these two representative scenarios and that it can be used to simulate real world fracking treatments whenever the assumption of planar growth is adequate.

Importantly, a true verification procedure is not performed here. For example,

mesh convergence studies and comparisons with well-known solutions are yet to be performed for these 3D problems as we did in Chapter 3. These require a few enhancements in the solver technology that are currently under development. First, due to the high discrepancy between the scales of degrees of freedom (matrix displacements, fracture apertures and pressures), general purpose linear solvers struggle to converge when the meshes are refined past a certain point. Because of that, special preconditioners that take into account the block structure of the system are being developed. Second, analytical solutions for poroelastic problems are scarce, so, a common verification procedure consists in solving them with vanishing small permeability coefficients to verify convergence towards the impermeable case, which does have a closed-form solution. However, as the permeability decreases, the poromechanics problem starts to display spurious pressure oscillations unless LBB-stable elements [128] or a stabilized formulations, such as [129] are used. These enhancements in the solver infrastructure are left for future work.

For the two problems in this Section, the material properties used are listed in Table 4.1. The fluid injection rate  $Q$  is set to  $2.0\text{m}^3/\text{s}$  (on each injection point).

	Value	Unit
Young's modulus ( $E$ )	16.0	GPa
Poisson's ratio ( $\nu$ )	0.18	-
Fluid viscosity ( $\mu$ )	$1.0 \times 10^{-12}$	GPa . s
Fluid bulk modulus ( $K_f$ )	$1.0 \times 10^{10}$	GPa
Critical energy release rate ( $G_c$ )	2.5	N/m
Biot coefficient ( $\alpha$ )	1.0	-
Rock permeability ( $\kappa_0$ )	$1.0 \times 10^{-13}$	$\text{m}^2$
Initial porosity ( $\phi_0$ )	0.2	-

**Table 4.1.** Material properties for planar fracture problems.

#### 4.4.1 Two parallel circular fractures under fluid injection

In the first problem, a pair of parallel penny-shaped fractures is stimulated with the injection of a viscous fluid. This configuration is representative of a very common

scenario in real-world fracking treatments where, in general, there are multiple clusters with several parallel fractures in each. Their simultaneous stimulation can lead to all fractures growing simultaneously or to situations in which only a few show substantial propagation while the others arrest early in the process. These scenarios can lead to very different well behaviors.

Depending on the distance between the fractures, there may also be non-planar growth, with fractures propagating away from each other, forming a cup shaped geometry. This is a consequence of the interaction between the stress fields in the vicinity of the multiple fractures fronts. This interaction is often called stress shadow effect. In this numerical example shown here, the initial fractures are placed far from each other to prevent this non-planar behavior. The far-field boundary conditions are assumed to be homogenous for pressures and displacements. Figure 4.6 illustrates the geometry. The dimensions are described in Table 4.2.

As for the discretization, the coarser global mesh consists of a structured grid that is refined near the fracture planes, with an element size of around 0.075m in the width direction and 0.15m in the other directions. The local mesh is 5 times smaller and the regularization length used in the phase-field subproblem is 0.05m. Importantly, the local domain consists of all local elements within a distance of 1m to the fracture front. Since the fractures are penny shaped, this local domain will have the shape of a torus. As for the time-step, it is uniformly set to 0.01s.

Due to the uniform boundary conditions and homogenous material properties, the fractures are expected to grow radially, preserving their circular shape. This feature is confirmed in the simulated results shown in Figure 4.8. In these snapshots, the right-side of the domain shows the pressure field computed in the global domain whereas the left side shows the discrete crack geometry, colored in gray scale indicating the aperture field. This figure also shows the subdomain around the crack front, colored by the damage field.

The aperture and pressure at the injection sources are important quantities of interest in this type of problem and their simulated time series are shown in Figure 4.7. Due to the symmetry, both fractures have the same pressure and aperture results. The reference values used to make the curves nondimensional are listed in Table 4.3.

	$d_1$	$d_2$	$d_3$	$L_x$	$L_y$	$L_z$	$r$
Value (m)	4.0	8.0	4.0	16.0	5.0	5.0	1.3

**Table 4.2.** Domain dimensions

	Value	Unit
$p_{ref}$	320	MPa
$w_{ref}$	$5.0 \times 10^{-4}$	m
$t_{ref}$	10	s

**Table 4.3.** Reference values used in the time series plots.

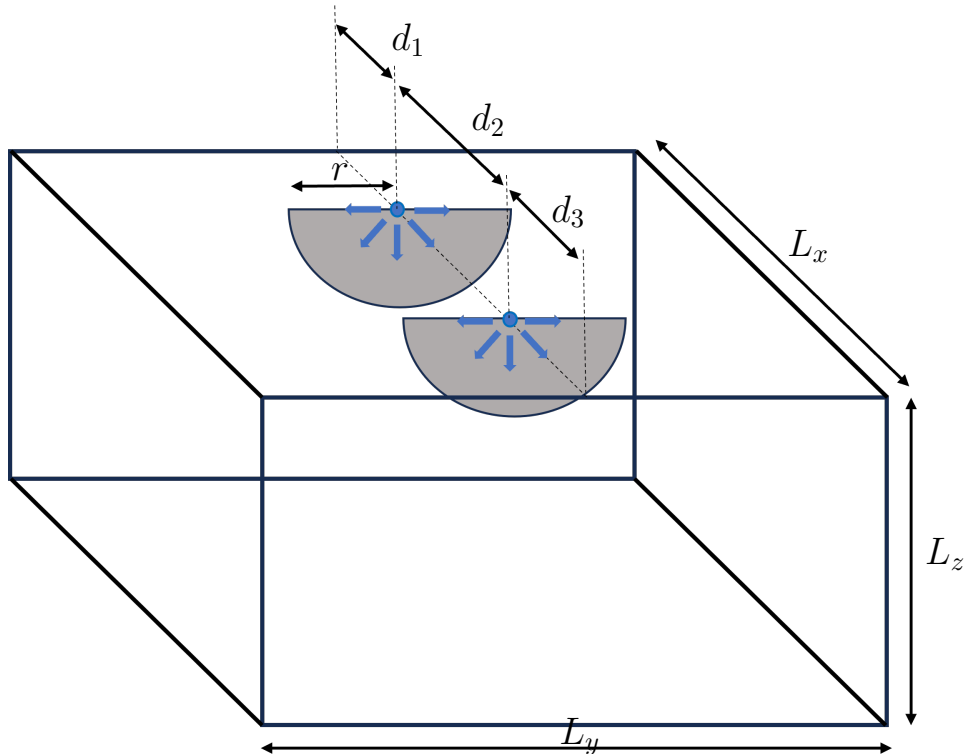


**FIGURE 4.6.** Schematic of the problem geometry.

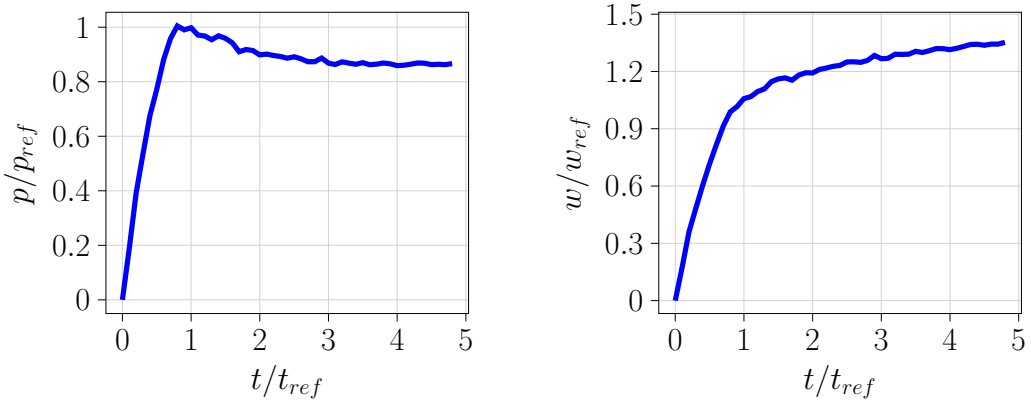
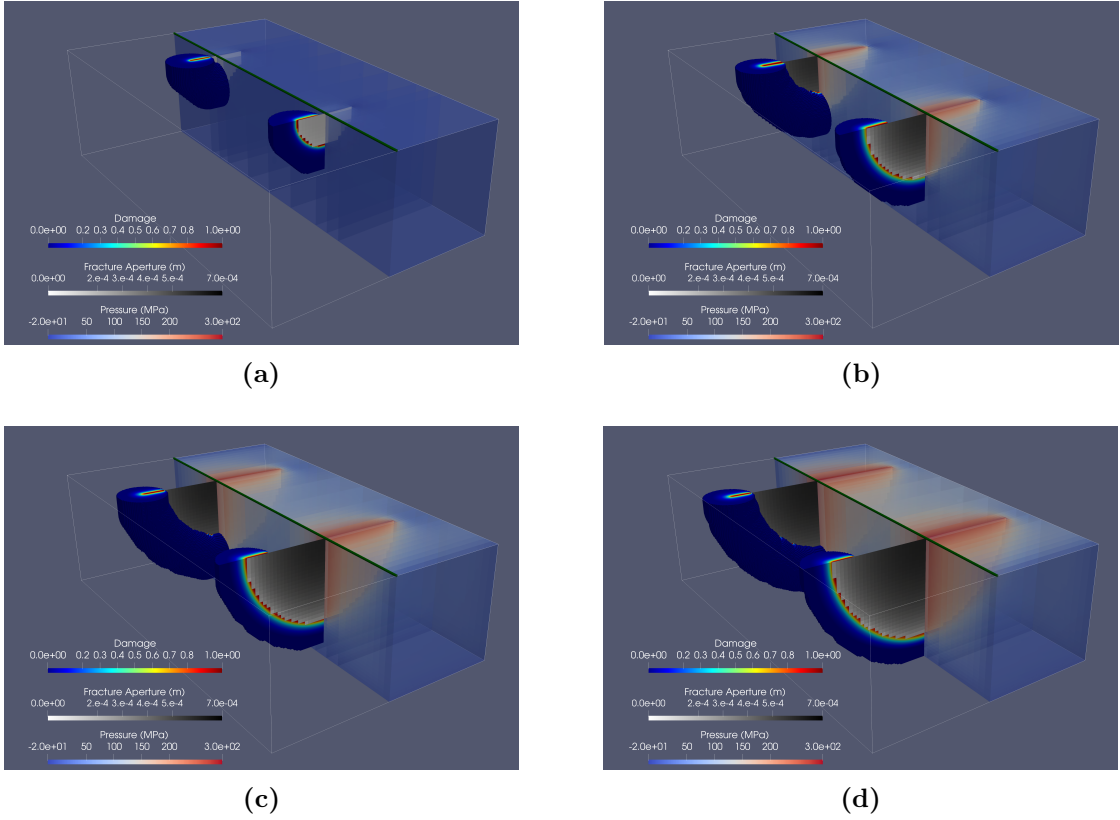


FIGURE 4.7. Two quantities of interest for the parallel fracture problem. On the left, the time series of the pressure at the injection point, on the right, the fracture aperture. Both plots show results scaled by reference values, calculated at the onset of propagation.



**FIGURE 4.8.** Snapshots of the simulated propagation. The left side of the figures shows the discrete fracture colored in grayscale according to the aperture and the subdomain colored according the damage value. The right side shows the pressure field in the global domain. (a) Snapshot  $t/t_{ref} = 0$ ; (b)  $t/t_{ref} = 1.5$ ; (c)  $t/t_{ref} = 3$ ; and (d)  $t/t_{ref} = 4.5$ .

#### 4.4.2 Merging two circular fractures

The second problem deals with the case of in-plane fracture merging. In general, fracture merging is one of the most difficult behaviors to simulate with discrete fracture approaches. That is due to the interaction between the stress fields of two fracture fronts, which makes most attempts to extract a stress intensity factor inaccurate. In practice, these situation may happen when fracking wells are drilled parallel to each other.

For problems involving crack merging, the phase-field approach becomes handy, allowing for the computation of crack advances through the solution of PDEs that are independent of the fracture topology. The multi-resolution approach explore this advantage, keeping a phase-field description around the fracture front and removing the limitations of discrete methods.

Since this problem deals with in-plane merging, getting the discrete fracture planes from the phase-field values is straightforward. However, it is important to mention that this can be a challenge in the case of non-planar merging.

The problem under consideration consists of two parallel fractures, initially of circular shape, embedded in a poroelastic matrix. Both are injected with a viscous fluid and propagate radially, eventually merging. An schematic of the geometry is shown in Figure 4.9, with the dimensions listed in Table 4.4. As in the previous problem, the far-field boundary conditions are assumed to be homogenous for pressures and displacements.

As for the discretization, the coarser global mesh consists of a structured grid that is refined near the fracture planes, with an element size of around 0.095m in the width direction and 0.15m in the other directions. The local mesh is 5 times smaller and the regularization length used in the phase-field subproblem is 0.05m. Importantly, the local domain consists of all local elements within a distance of 1m

to the fracture front. Initially, they consist of two separate torus, but they eventually merge as the cracks get closer. As for the time-step, it is uniformly set to 0.01s.

The simulated behavior is depicted in Figure 4.11, which shows the expected behavior, which the cracks growing perfectly as circles until they approach each other and merge. After the merge, the most concave part of the crack grows and opens up until the pressure drops enough for the propagation to arrest. While there is not reference solution to compare, at least qualitatively, the results make sense. As for the previous problem, the times series for the aperture and pressure in the injection point are shown in Figure 4.10. The reference values used to make these charts nondimensional are given in Table 4.5.

	$d_1$	$d_2$	$d_3$	$L_x$	$L_y$	$L_z$	$r$
Value (m)	6.5	7.0	6.5	8.0	20.0	5.0	1.5

**Table 4.4.** Domain dimensions

	Value	Unit
$p_{ref}$	520	MPa
$w_{ref}$	$7.0 \times 10^{-4}$	m
$t_{ref}$	10	s

**Table 4.5.** Reference values used in the time series plots.

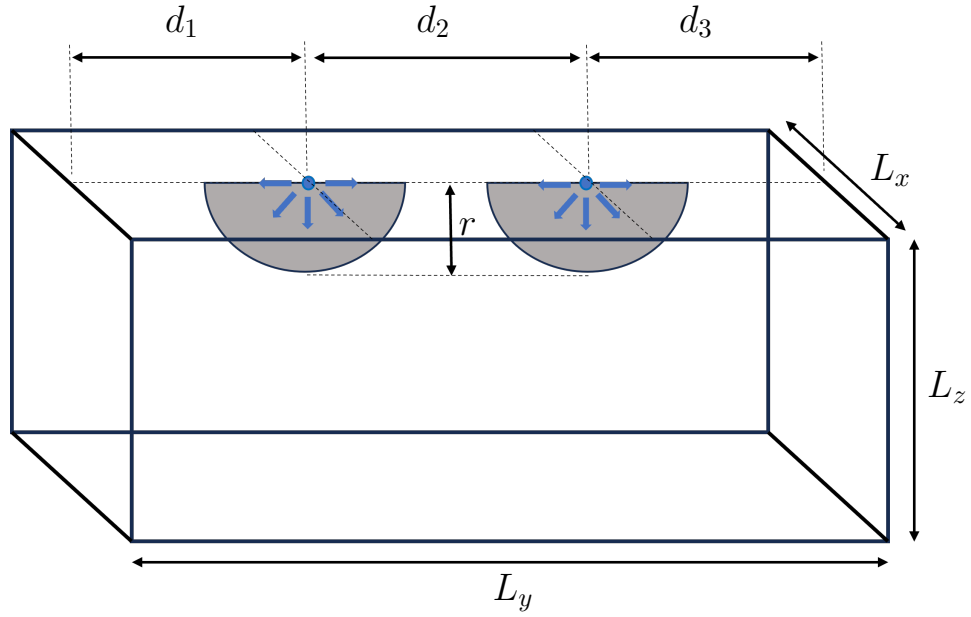


FIGURE 4.9. Schematic of the geometry for the merging problem.

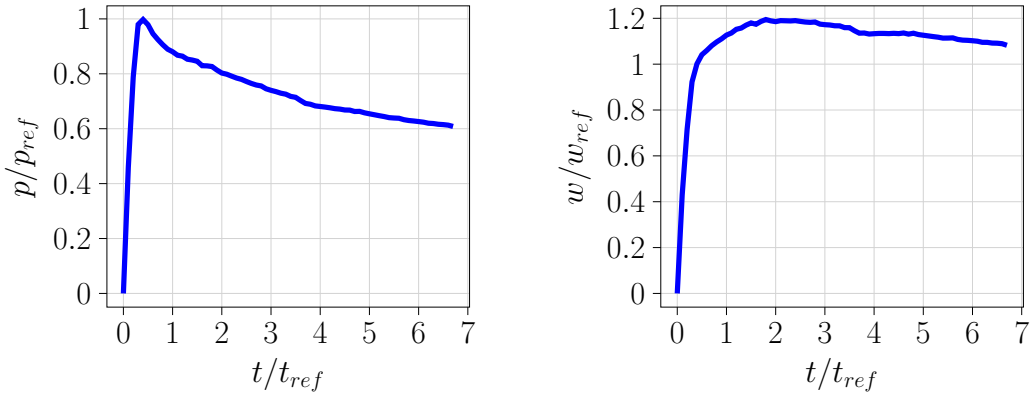


FIGURE 4.10. Two quantities of interest for the merging fracture problem. On the left, the time series of the pressure at the injection point, on the right, the fracture aperture. Both plots show results scaled by reference values, calculated at the onset of propagation.

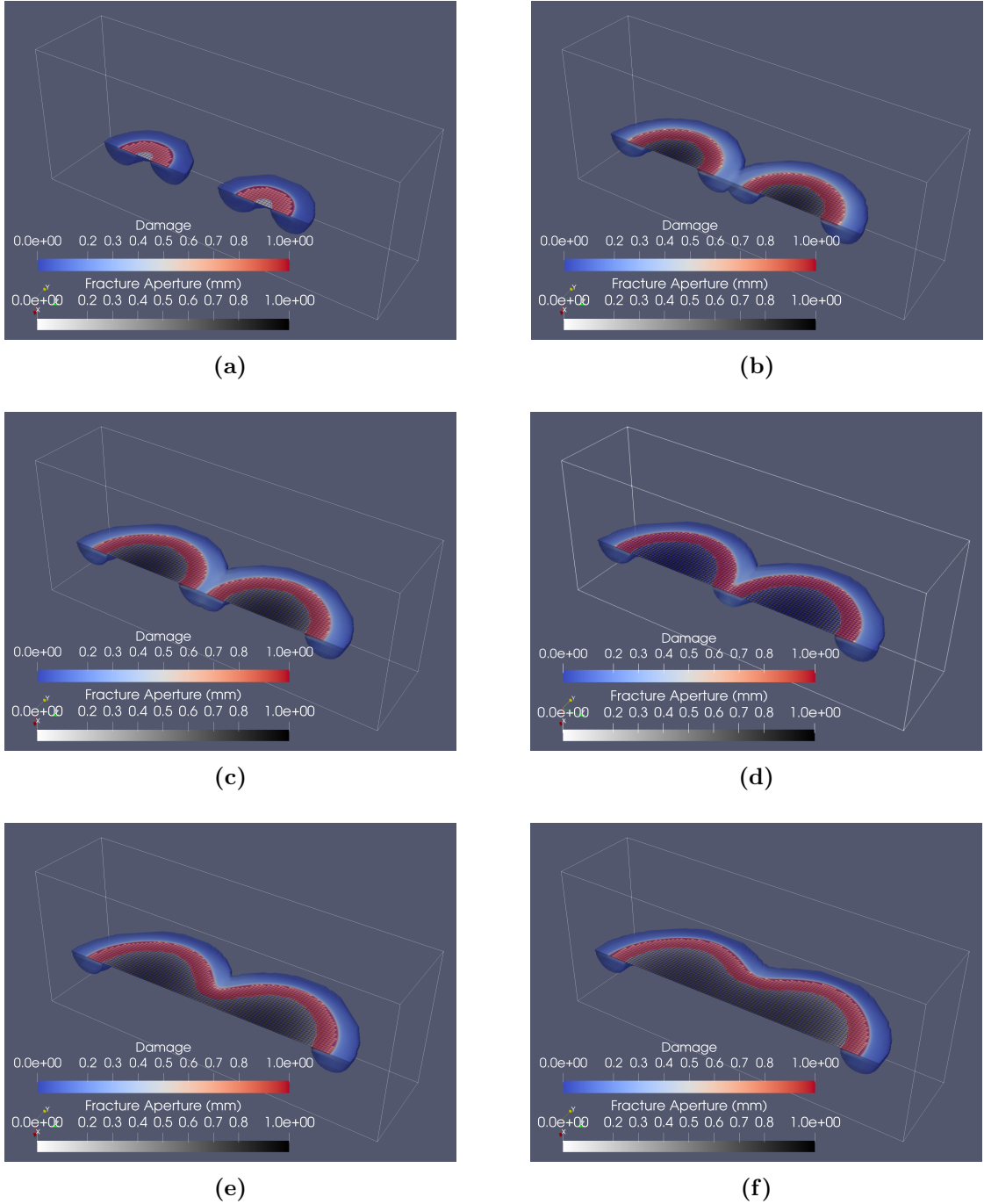


FIGURE 4.11. Snapshots of the simulated propagation. The discrete fracture is colored in grayscale according to the aperture and the subdomain colored according the damage value. (a) Snapshot  $t/t_{ref} = 0$ ; (b)  $t/t_{ref} = 1.3$ ; (c)  $t/t_{ref} = 2.6$ ; (d)  $t/t_{ref} = 3.9$ ; (e)  $t/t_{ref} = 5.2$ ; and (f)  $t/t_{ref} = 6.5$ .

## 4.5 Extension to non-planar fractures

While in several practical cases, such as in layered formation, the assumption of planar fractures is recommended [130], in many others, a general treatment that allows for non-planar growth is needed. However, in the context of the multi-resolution approach presented herein, this extension requires additional challenges to be addressed. In the last Section of this work, these challenges are discussed and a skeleton of a possible modified algorithm is described. A simplified nonplanar fracture problem in 2D is then used to test it. Although the result is favorable, the extension of this algorithm to full 3D problems requires additional modifications whose robustness is unclear.

### 4.5.1 Overview of a propagation algorithm for non-planar fractures

In Section 4.3, the algorithm 4.2 showed how to use the multi-resolution method to treat planar fractures in 3D. To extend it to non-planar cases, at a minimum, the following parts must be modified.

- First, the algorithm for tracking the damage in the front elements described in subsection 4.3.2 must be revisited, considering that the damage field is not planar. That definitely breaks the hypothesis of the damage volume criterion and also introduces pathological cases that make the applicability of the topological criterion more difficult.
- The update of the geometry becomes more complex for the same reason. Given a nonplanar damage field in an element, how to insert a planar<sup>2</sup> cut in the mesh that represents it well?

---

<sup>2</sup> While it is possible to develop embedded methods that allow for curved cuts inside elements, those are rarely used in practice due to the complex integration techniques needed. Because of that, in the current work, while strong assumptions on the embedded scheme are avoided, the focus is on first-order (i.e planar cuts) methods.

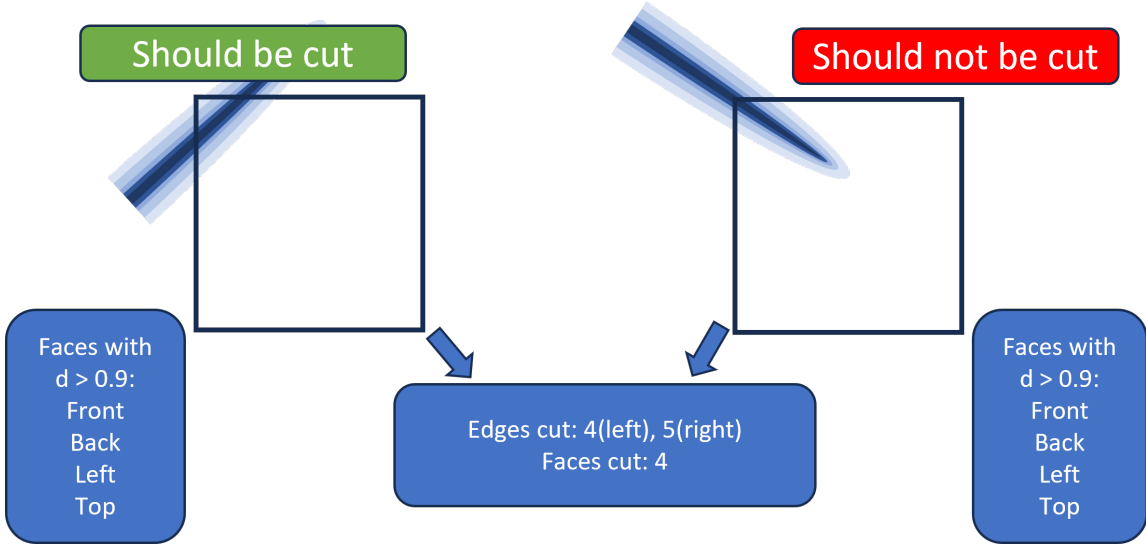


FIGURE 4.12. This figure shows a pathological case for the topological criterion proposed in 4.3.2. The element on the right is only partially damaged, however, the counts of cut edges and faces are higher than the ones for the element on the left, which is indeed fully cut.

- Finally, while for planar cuts the continuity of the fracture surface is always guaranteed, in nonplanar case, local (element-wise) approximations of the damage field with discrete cuts may lead to gaps in the fracture surface, such as the ones shown in Figure 4.1.

To address the first bullet point, one can start with the topological criterion proposed in 4.3.2, where the number of edges and faces with damage above a threshold is used. In general, if the damage band is small compared to the global element size, there is likely no ambiguity in the identification of cutting points. However, if the regularization length or the mesh size in the local problem are not very small, some difficulties may arise. For example, a wide damage band approaching the element diagonally may cut two adjacent edges as shown in Figure 4.12. This leads to a configuration where the number of cut edges and faces is large albeit the actual global element is not yet fractured.

Overcoming this limitation likely requires the use of information about the dam-

age in neighboring elements. One approach, used in the example problem shown next, keeps the topological criterion the same, but introduces a check on the cutting angle that is obtained after an element is cut. This check consists of comparing the normal to the new cut with the neighboring fractured elements. If the normals are too different (i.e  $\mathbf{n} \cdot \mathbf{n}_{neighbor} << 1$ ), then, this newly inserted cut is assumed to be due to a pathological case and then removed. The respective element is only considered for cutting again when the number of damaged faces increases. This check will be referred to as “the angle check”.

This heuristic relies on the assumption that fractures do not kink strongly over element boundaries, which is only true if the fracture curves have a large radius of curvature compared to the global element size.

Now, in terms of the second bullet point, regarding the extraction of the cutting plane from a damage field, an optimization algorithm such as [67] can be employed. In a nutshell, this method searches over the space of planes embedded in an element and constructs an idealized damage profile around this plane, using the optimal profile<sup>3</sup> given by  $d(x) = (1 - \text{dist}(x)/2\ell)^2$ , where  $\text{dist}(x)$  denotes the distance from  $x$  to the plane. These idealized profiles are then compared to the actual damage field and the one which is closest in the  $L_2$ -sense is chosen to be the cutting plane for that damage field.

One must be careful when integrating this optimization approach with the angle check described above. That heuristic works under the assumption that an attempted cut on an element which is not yet fractured will lead to a cutting plane that does not conform well to its neighbors. If an optimization approach is employed, that might not always be true. For example, in the case shown in Figure 4.12, the optimization approach can find the cutting plane induced by the partial fracture which will conform well to the existing cuts, even though the element is only partially cut.

---

<sup>3</sup> This is the profile for an AT-1 phase-field formulation.

So, in order to use the angle check, instead of applying the optimization method and then comparing the calculated plane with its neighbors, the idea of a coarser “pre-cut” is used. The idea of these pre-cuts is to rely only on the relative position of the cut identified in the element edges and faces by the topological criterion. This is done to ensure that, if one is dealing with a pathological case for the topological criterion, the pre-cut will indicate that and fail the angle check. In a 2D scenario, these pre-cuts can be obtained for example, by connecting the midpoints of the fractured faces. In 3D, the mapping becomes more complex. Figure 4.13 shows the four basic ways that a plane can intersect a brick element, rotations and reflections also need to be included. The pre-cut to be chosen for an element in 3D can then be obtained by evaluating which of these best approximate the set of damaged faces computed by the topological criterion for that element (based on its damage field in the local scale).

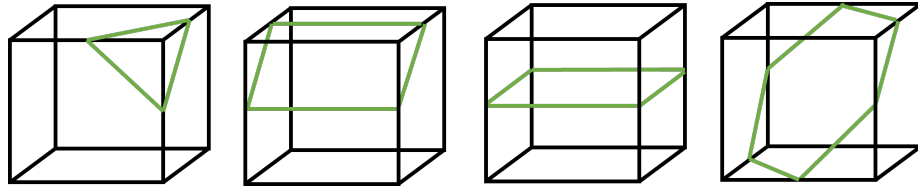


FIGURE 4.13. Basic shapes for a planar cut in a brick element.

Even with these modifications, the third and last bullet point, that concerns the continuity of the fracture surface must be addressed. For general embedded fracture approaches, continuity of the fracture surface is a necessary feature for the construction of the approximation space for the displacement field. This imposes serious complications to any type of algorithm that tries to construct surface increments on an element to element basis such as the one used here. However, the EFEM/EDFM approach used in this work and first proposed in [5] does offer a possible way to handle this issue. Unfortunately, that does break the generality of the multi-resolution approach with respect to the discretization technique used in the global domain.

By construction, the EFEM method does not assume continuity of the displacement field across element boundaries. In fact, the enrichment employed to represent the displacement jump does not interact with the neighboring elements and the final aperture might indeed be discontinuous. Still, the method does converge to the continuous solution in space. Figure 4.14, from [5] shows a typical aperture field computed with EFEM. This flexibility allows one to work with a fracture surface that has gaps in its geometry and still compute an accurate aperture field.

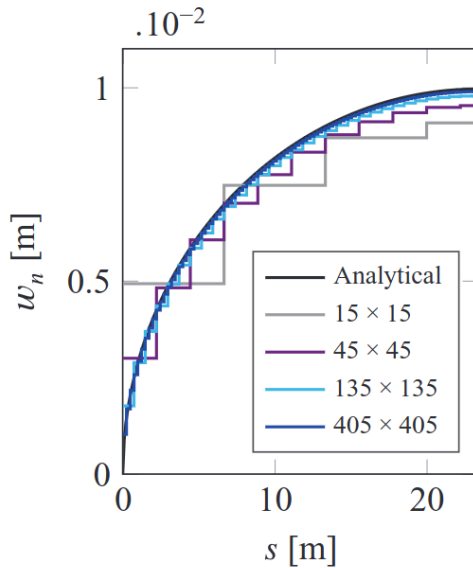


FIGURE 4.14. This figure shows how the aperture field computed with EFEM approaches an analytical solution as the mesh is refined. Note that the aperture field is discontinuity across element boundaries. Courtesy from [5]

On the other hand, for the computation of the flow problem, continuity is still required to calculate fluxes from a fracture cell to its neighbors. In fact, two compute the flux between two embedded cells, their common edge is used. That is, if one obtains a discontinuous fracture surface, there will be neighboring cells that do not share an edge and therefore, the flux between them will be zero.

Luckily, this issue can be circumvented by noting that the damage intersection on any edge is the same for all elements that contain that edge. Therefore, instead of

computing the fluxes directly from the common edge of neighboring fracture cells, one can store the intersections of the damage field with the global element edges and use them to build segments in between two neighboring cells. These segments can then be used to compute the fluxes, ensuring that even neighboring cells that happen to be on a surface discontinuity still get a unique, meaningful flux. Figure 4.15 shows two neighboring fracture elements that form a gap. In this case, the damage intersections D1 and D2 should be used to define the common edge that enters the flux calculation.

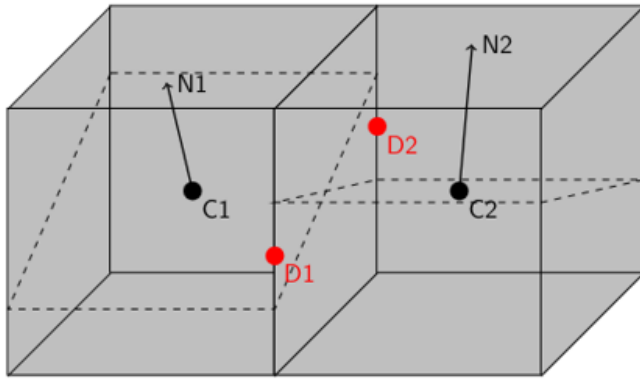


FIGURE 4.15. Flux in discontinuous fracture surfaces. D1 and D2 are the intersections of the damage field with the edges and serve to define a line segment that can be used to calculate the flux between the two fracture elements.

Combining all the workaround described in this Section, we can obtain an algorithm that extends algorithm 4.2 to allow for the treatment of non-planar fractures with a multi-resolution scheme. These modification are displayed as an algorithm in Figure 4.16.

While this algorithm theoretically answers most of the challenges discussed in this Section, a full implementation for general 3D problems is not yet completed. Currently, only the first modification to the algorithm, which concerns the topological criterion and its enhancement with the angle check and pre-cuts is implemented and tested. The optimization scheme and the flux computations based on the damage

intersections in the edges are left for future investigations.

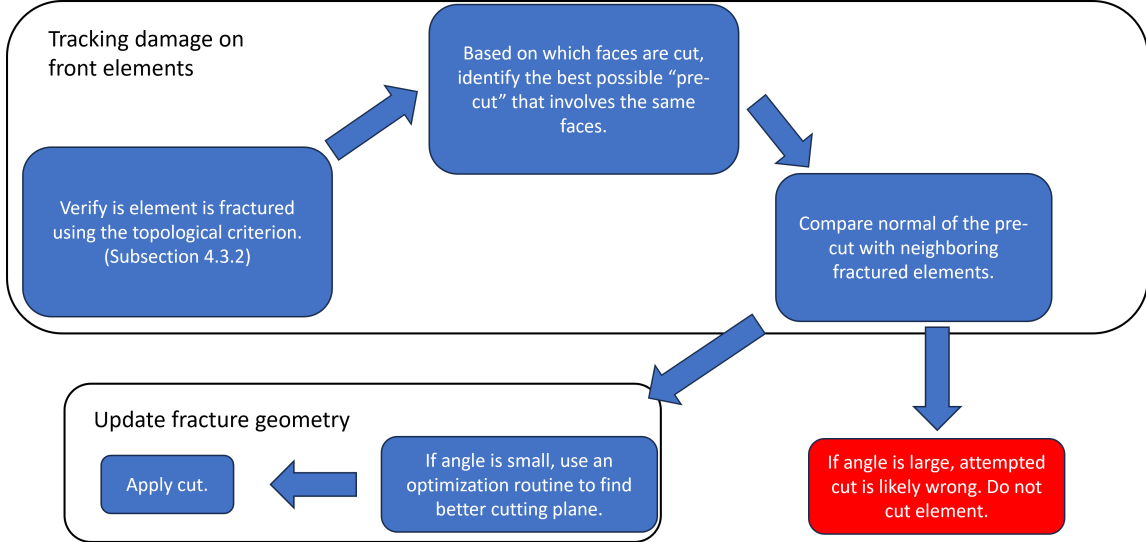


FIGURE 4.16. Enhancements to 4.2 to allow for non-planar fracture propagation.

In the next section, this simplification of the algorithm described above is applied to a 2.5D problem where the crack path is curved. It serves to check the efficacy of the proposed changes in the process of identifying the crack path. The fluid flow and poroelastic effects are turned off for simplicity.

#### 4.5.2 Example problem

This subsection presents a small 2D problem used to test some features of the algorithm presented in 4.5.1. The problem consists of an edge crack in a square plate, which is pulled in the top edge by an inclined displacement  $\Delta u$ , at an angle of 45deg, as shown in Figure 4.17. The bottom surface is held fixed while the sides are left with a zero traction boundary condition. The material properties and geometric parameters are given in Table 4.6. All the fluid effects are removed, as the focus is only on the algorithm to track the fracture and insert the discrete cuts. The subdomain is set to be the entire domain, which simplifies the transfer of boundary conditions from the global to local problem.

	Value	Unit
Young's modulus ( $E$ )	16.0	GPa
Poisson's ratio ( $\nu$ )	0.18	–
Critical energy release rate ( $G_c$ )	2.5	N/m
Regularization length ( $\ell$ )	0.04	m
Applied displacement ( $\Delta u$ )	$2.0 \times 10^{-5}$	m
Initial crack length (a)	2.5	m
Plate size (L)	5.0	m

**Table 4.6.** Material properties for non-planar fracture problem.

In terms of discretization, the coarser global mesh uniformly splits the domain in 21x21 elements, with the finer grid being 11 times smaller. That leads to a subdomain element whose size is 2 times smaller than the phase-field regularization length. The load increment used was  $2.0 \times 10^{-7}$  m.

A very similar problem was studied in [68]. Despite the differences in material properties, it serves as a reference solution for the crack path, which is the main quantity of interest for this analysis. So, their results are shown in Figure 4.18a. Despite the simplification in defining the cut direction, the discrete fracture is still capable of tracking the damage band quite well, as shown in Figure 4.18b, displaying a great agreement with the reference solution. Interestingly, this problem involves multiple cases of the damage band approaching the diagonal of an element, which constitutes a pathological case, described previously. This shows that the correction based on the neighboring cutting angles is indeed useful and necessary in this type of approach.

A relative straightforward improvement can be done with the introduction of an optimization method, as discusssed in 4.5.1 to produce cuts that better align with the damage band locally. However, the use of “crude” approximations (pre-cuts) is still important to test the angle criteria and prevent lightly damaged elements from being wrongly cut due to a pathological case, such as the one shown in Figure 4.12.

One the downside, this example doesn't explore a lot of the difficulties that arise

in general three-dimensional problems. First, creating a map between the damaged faces and the pre-cuts shown in Figure 4.13 becomes much more difficult in 3D. In addition to that, the angle criteria may work well in cracks that evolve progressively as the one in this example, however, it may get into a “locking” situation if two cracks are merging at an angle. This is, different neighbors may impose constraints in the cutting angle of an element that may be impossible to satisfy simultaneously.

Overcoming these challenges likely requires a more severe reformulation of the algorithm used for planar fractures. One promising approach is to employ a global method of surface reconstruction after the solution of the phase-field problem. This is a research topic on its own, with important contributions developed in recent years, such as [131, 132, 133]. In the context of hybrid phase-field methods, the authors of [134] used a global surface reconstruction to improve the simulation of ductile fracture. They used the gradient of the damage to guide the identification of a discrete fracture surface embedded in a triangular mesh. While the robustness of their reconstruction in the presence of crack merging and branching is still unclear, it certainly points to a promising direction that can be explored in the context of the multi-resolution approach for hydraulic fracture.

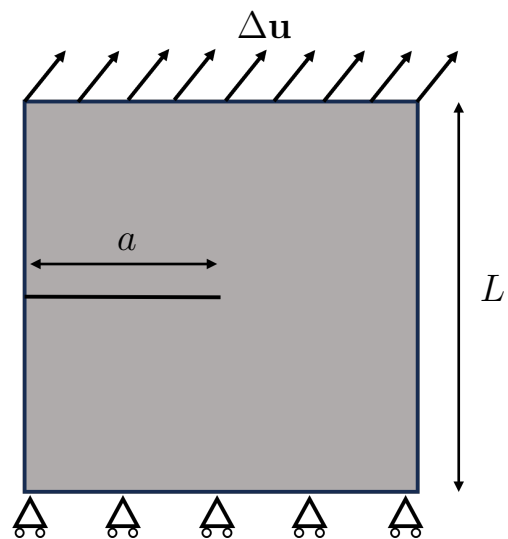


FIGURE 4.17. Schematic of the edge crack problem. The load of the top surface is inclined 45deg, which leads to a curved fracture path.

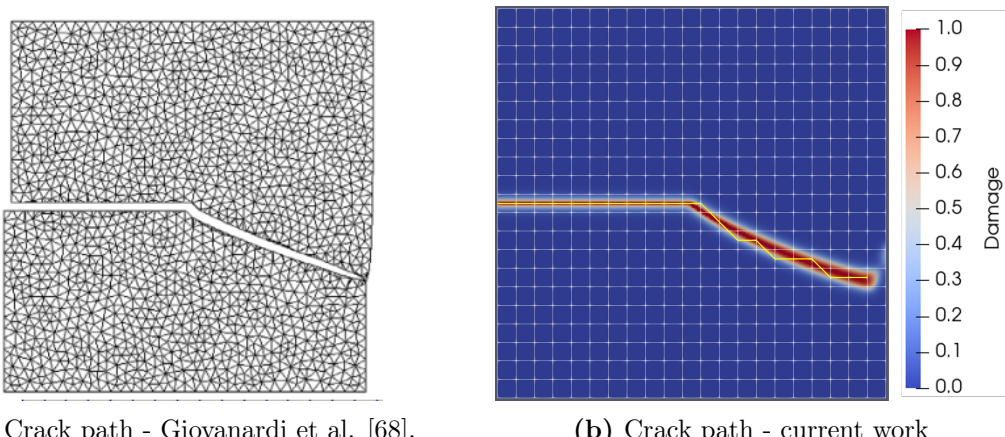


FIGURE 4.18. Comparision of the crack paths obtained for the edge crack problem. Despite the roughness of the crack path in (b), the overall path compares very well to the reference result.

# 5

## Conclusions and Future Work

In this dissertation, methods for computer simulation of fluid-driven fracture are studied. In particular, the phase-field approach, whose application in this context is still in its infancy, is explored as a technology to improve the accuracy and robustness of models. Some known challenges associated with the use of the phase-field, namely the application of tractions on the diffuse surfaces and the computation of fracture apertures are circumvented by the novel contributions of this work.

Chapter 2 reviews various models for incorporating pressure loads on diffuse crack faces. This includes the analysis of a new formulation that can be obtained by assuming that the pressure load does not act on the virtual extension of a crack. The new formulation is referred to as the “unloaded virtual crack formulation” (UVC). A new form of the J-Integral for pressurized cracks in the phase-field context is also derived. This J-Integral proves to be particularly useful in verifying the accuracy of the various models for propagating cracks,

The new (UVC) formulation allows for an unified treatment of crack nucleation and propagation in scenarios involving either brittle or cohesive fracture, and provides for better accuracy in some problems compared to existing approaches. As

it allows for the use of the same governing equation for the damage parameter, its computational implementation within existing phase-field solvers is also simpler.

Chapter 3 presents a new approach for simulating fluid-driven fracture. The method relies on a global problem that captures flow and deformation fields, and a local problem that captures crack growth with the aid of a phase-field method. The two problems are coupled through the transfer of displacement and pressure fields, as well as updates to the crack geometry. This multi-resolution approach allows the phase-field method to be used as a tool to update the crack geometry without the need to explicitly reconstruct the crack aperture from the diffuse representation.

The accuracy of the multi-resolution approach is evaluated through several numerical examples. These include the well-known KGD problem, for which a good agreement with analytical solutions is obtained in both the toughness and viscosity regimes. A problem with a curved crack trajectory around a stiff inclusion also demonstrates the overall robustness of the approach.

Finally, Chapter 4 extends the multi-resolution method proposed in Chapter 3 to three dimensions. It begins with the simpler, yet useful case of planar fractures. A modified algorithm is presented and its implementation in the HPC code GEOS is developed. Representative examples are shown to highlight the capabilities of the model and also the robustness of the code. Then, the case of non-planar fractures is investigated. The previous algorithm for planar fractures in 3D is revisited and several modifications are provided to allow for more complex geometry. A simplified implementation is then tested in a 2.5D problem, helping to identify the main challenges and paving the way for future work in the topic.

Multiple areas for future work naturally present themselves throughout the dissertation and can lead to new research topics in this field.

- The (UVC) formulation from Chapter 2 is shown to be capable of predicting

fracture nucleation. However, it suffers from the well-known issues of energetic phase-field models which can not represent the true strength-based resistance of fracture of real-world materials. Therefore, incorporating such model in a strength-based formulation such as [135] is key to improve simulations of fracture nucleation.

- Also in Chapter 2, modifications to accelerate the convergence of the model with respect to the phase-field parameter  $\ell$  will also important, given that the current form requires very fine grids to achieve accurate results.
- For the multi-resolution approach, the directions of future work can be split in two parts. The first concerns the robustness of the algorithm developed for planar fractures, with the aim to turn it into a practical tool for engineering simulation. This line of work includes a revision of the algorithm to handle unstructured grids and additional physics. It also concerns the numerical solver, which would benefit a lot from a physics-informed linear solver as well as from a stabilization procedure. Additional verification examples, such as the ones shown in Chapter 3 are also needed.
- The second direction is the treatment of non-planar fractures. For this task, the main challenge appears to be the identification of fractured elements from the damage field. Based on the discussion and preliminary results shown in Chapter 4, global algorithms to reconstruct are sharp geometry from the phase-field are likely to help considerably in this task. They will also help handling the issue of gaps that can appear when stitching new fracture cells to the current discrete crack.

# Appendix A

## Equivalence to SIF condition

In this appendix, the energy release rate for a single, straight crack under an arbitrary pressure load  $p(x)$  is computed, assuming that infinitesimal crack increments are traction-free, as shown in Figure 2.2a. Griffith's criterion states that propagation should happen whenever this energy release rate, which will be denoted by  $G$ , reaches  $G_c$ . This will give rise to a condition for propagation based on the pressure distribution  $p(x)$ , the crack size  $a$  and Young's modulus  $E'$ <sup>1</sup>. The purpose of the following derivation is to demonstrate that this condition is equivalent to the stress intensity factor criterion [136].

Initially, consider the Sneddon-Lowengrub solution for the aperture of a pressure loaded crack in an infinite plate, under plane strain conditions,

$$w(x) = \frac{4a}{\pi E'} \int_0^1 p(sa) Z(x/a, s) ds \quad (\text{A.1})$$

where

---

<sup>1</sup> assuming plane strain,  $E' = E/(1 - \nu^2)$

$$Z(r, s) = \log \left| \frac{\sqrt{1 - r^2} + \sqrt{1 - s^2}}{\sqrt{1 - r^2} - \sqrt{1 - s^2}} \right| \quad (\text{A.2})$$

is a convolution kernel. The work done by the pressure load is then,

$$W_p = \int_{-a}^a p w dx = \int_{-a}^a p(y) \frac{4a}{\pi E'} \int_0^1 p(sa) Z(x/a, s) ds dy. \quad (\text{A.3})$$

Clayperon's theorem [137] states that the potential energy is negative half of the work exerted in the boundary, which, in this case is only  $W_p$ . Hence

$$U = -\frac{1}{2} W_p = -\frac{1}{2} \int_{-a}^a p w dx = -\frac{4a^2}{\pi E'} \int_0^1 p(ar) \int_0^1 p(sa) Z(r, s) ds dr. \quad (\text{A.4})$$

Let's write the energy release rate, assuming that the pressure field doesn't vary as the crack advances by a small amount  $da$ . That is,

$$p^{a+da}(x) = \begin{cases} p^a(x), & \text{if } x \leq a \\ 0, & \text{if } a \leq x \leq a + da \end{cases} \quad (\text{A.5})$$

$$dU = U(a + da, p^{a+da}) - U(a + da, p^a), \quad (\text{A.6})$$

$$\begin{aligned} dU = -\frac{4}{\pi E'} \int_0^{a+da} p^{a+da}(x) \int_0^{a+da} p^{a+da}(y) Z\left(\frac{x}{a+da}, \frac{y}{a+da}\right) dy dx \\ + \frac{4}{\pi E'} \int_0^a p^a(x) \int_0^a p^a(y) Z(x/a, y/a) dy dx. \end{aligned} \quad (\text{A.7})$$

Using the definition of  $p^{a+da}$  given above,

$$dU = -\frac{4}{\pi E'} \int_0^a p^a(x) \int_0^a p^a(y) \left( Z\left(\frac{x}{a+da}, \frac{y}{a+da}\right) - Z(x/a, y/a) \right) dy dx. \quad (\text{A.8})$$

By symmetry, both tips of the crack propagate with the same energy release rate, so, one can write,

$$2G = -\frac{dU}{da} = \frac{4}{\pi E'} \int_0^a p^a(x) \int_0^a p^a(y) \frac{1}{da} \left( Z\left(\frac{x}{a+da}, \frac{y}{a+da}\right) - Z(x/a, y/a) \right) dy dx. \quad (\text{A.9})$$

The term between parenthesis can be re-written as,

$$\begin{aligned} Z\left(\frac{x}{a+da}, \frac{y}{a+da}\right) - Z(x/a, y/a) &= \\ \log \left| \frac{\sqrt{(a+da)^2 - x^2} + \sqrt{(a+da)^2 - y^2}}{\sqrt{(a+da)^2 - x^2} - \sqrt{(a+da)^2 - y^2}} \right| - \log \left| \frac{\sqrt{a^2 - x^2} + \sqrt{a^2 - y^2}}{\sqrt{a^2 - x^2} - \sqrt{a^2 - y^2}} \right| \\ &= \log \left| \frac{\sqrt{(a+da)^2 - x^2} + \sqrt{(a+da)^2 - y^2}}{\sqrt{a^2 - x^2} + \sqrt{a^2 - y^2}} \right| \\ &\quad - \log \left| \frac{\sqrt{(a+da)^2 - x^2} - \sqrt{(a+da)^2 - y^2}}{\sqrt{a^2 - x^2} - \sqrt{a^2 - y^2}} \right|. \quad (\text{A.10}) \end{aligned}$$

The second term contains a singularity, which can be removed if one re-writes it as,

$$\begin{aligned}
& \log \left| \frac{\sqrt{(a+da)^2 - x^2} - \sqrt{(a+da)^2 - y^2}}{\sqrt{a^2 - x^2} - \sqrt{a^2 - y^2}} \right| = \\
& \quad \log \left| \frac{\sqrt{(a+da)^2 - x^2} - \sqrt{(a+da)^2 - y^2}}{\sqrt{a^2 - x^2} - \sqrt{a^2 - y^2}} \right. \\
& \quad \times \frac{\sqrt{(a+da)^2 - x^2} + \sqrt{(a+da)^2 - y^2}}{\sqrt{a^2 - x^2} + \sqrt{a^2 - y^2}} \\
& \quad \times \frac{\sqrt{a^2 - x^2} + \sqrt{a^2 - y^2}}{\sqrt{(a+da)^2 - x^2} + \sqrt{(a+da)^2 - y^2}} \left. \right| \\
& = \log \left| \frac{(a+da)^2 - x^2 - (a+da)^2 + y^2}{a^2 - x^2 - a^2 + y^2} \right. \\
& \quad \times \frac{\sqrt{a^2 - x^2} + \sqrt{a^2 - y^2}}{\sqrt{(a+da)^2 - x^2} + \sqrt{(a+da)^2 - y^2}} \left. \right| \\
& = -\log \left| \frac{\sqrt{(a+da)^2 - x^2} + \sqrt{(a+da)^2 - y^2}}{\sqrt{a^2 - x^2} + \sqrt{a^2 - y^2}} \right|. \quad (\text{A.11})
\end{aligned}$$

This expression can be plugged back into (A.10) to obtain,

$$\begin{aligned}
& Z\left(\frac{x}{a+da}, \frac{y}{a+da}\right) - Z(x/a, y/a) = \\
& \log \left| \frac{\sqrt{(a+da)^2 - x^2} + \sqrt{(a+da)^2 - y^2}}{\sqrt{(a+da)^2 - x^2} - \sqrt{(a+da)^2 - y^2}} \right| - \log \left| \frac{\sqrt{a^2 - x^2} + \sqrt{a^2 - y^2}}{\sqrt{a^2 - x^2} - \sqrt{a^2 - y^2}} \right| \\
& = 2 \log \left| \frac{\sqrt{(a+da)^2 - x^2} + \sqrt{(a+da)^2 - y^2}}{\sqrt{a^2 - x^2} + \sqrt{a^2 - y^2}} \right|. \quad (\text{A.12})
\end{aligned}$$

Hence,

$$\begin{aligned}
& \frac{1}{da} \left( Z\left(\frac{x}{a+da}, \frac{y}{a+da}\right) - Z(x/a, y/a) \right) \\
& = \frac{2}{da} \log \left| \frac{\sqrt{(a+da)^2 - x^2} + \sqrt{(a+da)^2 - y^2}}{\sqrt{a^2 - x^2} + \sqrt{a^2 - y^2}} \right|. \quad (\text{A.13})
\end{aligned}$$

Now, the terms in the numerator can be expanded with a Taylor series,

$$\sqrt{(a + da)^2 - x^2} = \sqrt{a^2 - x^2} + \frac{a}{\sqrt{a^2 - x^2}} da + O(da^2), \quad (\text{A.14})$$

leading to,

$$\begin{aligned} \frac{1}{da} \left( Z\left(\frac{x}{a + da}, \frac{y}{a + da}\right) - Z(x/a, y/a) \right) &= \\ \frac{2}{da} \log \left| \frac{\sqrt{a^2 - x^2} + \frac{a}{\sqrt{a^2 - x^2}} da + O(da^2)}{\sqrt{a^2 - x^2} + \sqrt{a^2 - y^2}} \right. & \\ \left. + \frac{\sqrt{a^2 - y^2} + \frac{a}{\sqrt{a^2 - y^2}} da + O(da^2)}{\sqrt{a^2 - x^2} + \sqrt{a^2 - y^2}} \right|, \quad (\text{A.15}) \end{aligned}$$

which, after using a Taylor expansion, simplifies to,

$$\frac{1}{da} \left( Z\left(\frac{x}{a + da}, \frac{y}{a + da}\right) - Z(x/a, y/a) \right) = \frac{2a}{\sqrt{a^2 - x^2} \sqrt{a^2 - y^2}} + O(da). \quad (\text{A.16})$$

Now, we can finally go back to the energy release rate,

$$\begin{aligned} 2G = -\frac{dU}{da} &= \frac{4}{\pi E'} \int_0^a p^a(x) \int_0^a p^a(y) \frac{2a}{\sqrt{a^2 - x^2} \sqrt{a^2 - y^2}} dy dx = \\ \frac{8a}{\pi E'} \int_0^1 \frac{p^a(ar)}{\sqrt{1 - r^2}} \int_0^1 \frac{p^a(as)}{\sqrt{1 - s^2}} ds dr &= \frac{8a}{\pi E'} \left( \int_0^1 \frac{p^a(as)}{\sqrt{1 - s^2}} ds \right)^2. \quad (\text{A.17}) \end{aligned}$$

From [138], the stress intensity factor under these same conditions is,

$$K_I = 2\sqrt{\frac{a}{\pi}} \left( \int_0^1 \frac{p^a(as)}{\sqrt{1 - s^2}} ds \right) \quad (\text{A.18})$$

From a simple inspection, one can see that  $G = K_I^2/E'$ , which guarantees the equivalence of the energy release rate criterion under the assumption in Figure 2.2a and

the stress intensity factor condition. If instead, one assumes that the pressure load in the vicinity of a propagating crack behaves as in Figure 2.2b, this equivalence between the energetic criterion and the stress intensity factor may be violated.

# Bibliography

- [1] Blaise Bourdin, Chukwudi P Chukwudzie, Keita Yoshioka, et al. A variational approach to the numerical simulation of hydraulic fracturing. In *SPE Annual Technical Conference and Exhibition*. Society of Petroleum Engineers, 2012.
- [2] C. Landis and Z. Wilson. The Phase-field Modeling of Hydraulic Fracture. In *workshop: Variational Models of Fracture*, 2016. <http://www.birs.ca/workshops//2016/16w5090/files/Banff-Landis.pdf>, visited on 2022-05-05.
- [3] J Adachi, E Siebrits, A Peirce, and J Desroches. Computer simulation of hydraulic fractures. *International Journal of Rock Mechanics and Mining Sciences*, 44(5):739–757, 2007.
- [4] Thomas C Gasser and Gerhard A Holzapfel. 3d crack propagation in unreinforced concrete.: A two-step algorithm for tracking 3d crack paths. *Computer Methods in Applied Mechanics and Engineering*, 195(37-40):5198–5219, 2006.
- [5] Matteo Cusini, Joshua A White, Nicola Castelletto, and Randolph R Settgast. Simulation of coupled multiphase flow and geomechanics in porous media with embedded discrete fractures. *International Journal for Numerical and Analytical Methods in Geomechanics*, 45(5):563–584, 2021.
- [6] Eia data on u.s. gas sources, 2022. URL <https://www.eia.gov/tools/faqs/faq.php?id=847&t=6>.
- [7] Eia data on u.s. oil sources, 2022. URL <https://www.eia.gov/tools/faqs/faq.php?id=907&t=8>.
- [8] Peng-Zhi Pan, Jonny Rutqvist, Xia-Ting Feng, and Fei Yan. Tough–rdca modeling of multiple fracture interactions in caprock during co<sub>2</sub> injection into a deep brine aquifer. *Computers & Geosciences*, 65:24–36, 2014.
- [9] Zissis Moschovidis, Ronald Steiger, Richard Peterson, Norm Warpinski, Chris Wright, Ed Chesney, Joe Hagan, Ahmed Abou-Sayed, Richard Keck, Matt Frankl, Carole Fleming, Steve Wolhart, Buddy McDaniel, Allen Sinor, Steinar Ottesen, Lynn Miller, Reid Beecher, John Dudley, Dick Zinno, and Oktay

- Akhmedov. The Mounds Drill-Cuttings Injection Field Experiment: Final Results and Conclusions. In *IADC/SPE Drilling Conference*. OnePetro, February 2000. doi: 10.2118/59115-MS. URL <https://dx.doi.org/10.2118/59115-MS>.
- [10] J. Desroches. Stress testing with the micro-hydraulic fracturing technique: Focus on fracture reopening. In *The 35th US Symposium on Rock Mechanics (USRMS)*. OnePetro, June 1995. URL <https://dx.doi.org/>.
  - [11] J Desroches and M Thiercelin. Modelling the propagation and closure of micro-hydraulic fractures. In *International Journal of Rock Mechanics and Mining Sciences & Geomechanics Abstracts*, volume 30, pages 1231–1234. Elsevier, 1993.
  - [12] Mark Board, Tony Rorke, Gary Williams, and Nick Gay. Fluid injection for rockburst control in deep mining. In *The 33rd US Symposium on Rock Mechanics (USRMS)*. OnePetro, June 1992. URL <https://dx.doi.org/>.
  - [13] Xi Zhang, Emmanuel Detournay, and Rob Jeffrey. Propagation of a penny-shaped hydraulic fracture parallel to the free-surface of an elastic half-space. *International Journal of Fracture*, 115(2):125–158, May 2002. ISSN 1573-2673. doi: 10.1023/A:1016345906315. URL <https://doi.org/10.1023/A:1016345906315>.
  - [14] Permeability and stress in crystalline rocks - Banks - 1996 - Terra Nova - Wiley Online Library, 1996. URL <https://onlinelibrary.wiley.com/doi/abs/10.1111/j.1365-3121.1996.tb00751.x>.
  - [15] C. Less and N. Andersen. Hydrofracture: State Of The Art In South Africa. *Applied Hydrogeology*, 2(2):59–63, 1994. ISSN 1435-0157. doi: 10.1007/s100400050050.
  - [16] TK Perkins and L Re Kern. Widths of hydraulic fractures. *Journal of Petroleum Technology*, 13(09):937–949, 1961.
  - [17] IN Sneddon and HA Elliot. The opening of a griffith crack under internal pressure. *Quarterly of Applied Mathematics*, 4(3):262–267, 1946.
  - [18] RP Nordgren. Propagation of a vertical hydraulic fracture. *Society of Petroleum Engineers Journal*, 12(04):306–314, 1972.
  - [19] A Khristianovic Zheltov. 3. formation of vertical fractures by means of highly viscous liquid. In *4th World Petroleum Congress*. OnePetro, 1955.
  - [20] J Geertsma and F De Klerk. A rapid method of predicting width and extent of hydraulically induced fractures. *Journal of Petroleum Technology*, 21(12):1571–1581, 1969.

- [21] J Desroches, E Detournay, B Lenoach, P Papanastasiou, John Richard Anthony Pearson, M Thiercelin, and Ailan Cheng. The crack tip region in hydraulic fracturing. *Proceedings of the Royal Society of London. Series A: Mathematical and Physical Sciences*, 447(1929):39–48, 1994.
- [22] B Lenoach. The crack tip solution for hydraulic fracturing in a permeable solid. *Journal of the Mechanics and Physics of Solids*, 43(7):1025–1043, 1995.
- [23] E Detournay, JI Adachi, DI Garagash, et al. Asymptotic and intermediate asymptotic behavior near the tip of a fluid-driven fracture propagating in a permeable elastic medium. *Structural Integrity and Fracture*, pages 9–18, 2002.
- [24] E Detournay and DI Garagash. The near-tip region of a fluid-driven fracture propagating in a permeable elastic solid. *Journal of Fluid Mechanics*, 494:1–32, 2003.
- [25] D Garagash and E Detournay. The tip region of a fluid-driven fracture in an elastic medium. *J. Appl. Mech.*, 67(1):183–192, 2000.
- [26] Emmanuel Detournay. Propagation regimes of fluid-driven fractures in impermeable rocks. *International Journal of Geomechanics*, 4(1):35–45, 2004.
- [27] JI Adachi and E Detournay. Self-similar solution of a plane-strain fracture driven by a power-law fluid. *International Journal for Numerical and Analytical Methods in Geomechanics*, 26(6):579–604, 2002.
- [28] R Carbonell, Jean Desroches, and Emmanuel Detournay. A comparison between a semi-analytical and a numerical solution of a two-dimensional hydraulic fracture. *International journal of solids and structures*, 36(31-32):4869–4888, 1999.
- [29] AA Savitski and E Detournay. Propagation of a penny-shaped fluid-driven fracture in an impermeable rock: asymptotic solutions. *International journal of solids and structures*, 39(26):6311–6337, 2002.
- [30] Dmitry I. Garagash and Emmanuel Detournay. Plane-Strain Propagation of a Fluid-Driven Fracture: Small Toughness Solution. *Journal of Applied Mechanics*, 72(6):916–928, 04 2005. ISSN 0021-8936. doi: 10.1115/1.2047596.
- [31] Mark W McClure and Charles A Kang. A Three-Dimensional Reservoir, Wellbore, and Hydraulic Fracturing simulator that is Compositional and Thermal, Tracks Proppant and Water Solute Transport, Includes Non-Darcy and Non-Newtonian Flow, and Handles Fracture Closure. In *SPE Reservoir Simulation Conference*. OnePetro, 2017.
- [32] M. McClure, C. Kang, S. Medam, and C. Hewson. ResFrac technical writeup. *arXiv preprint arXiv:1804.02092*, 2018.

- [33] Itasca Consulting Group, Inc. Xsite, ver. 3.0. minneapolis: Itasca., 2019. Accessed June 10th, 2023. <https://www.itascacg.com/software/XSite>.
- [34] Schlumberger Ltd. Kinetix reservoir-centric stimulation-to-production software., 2021. Accessed June 10th, 2023. <https://www.slb.com/completions/stimulation/stimulation-optimization/kinetix-reservoir-centric-stimulation-to-production-software>.
- [35] Schlumberger USTC. Kinetix for petrel 2020.1., 2020. Accessed June 10th, 2023. <https://www.ocean.slb.com/en/plug-ins/plugindetails?ProductId=PMPW-B1>.
- [36] Bin Chen, Beatriz Ramos Barboza, Yanan Sun, Jie Bai, Hywel R Thomas, Martin Dutko, Mark Cottrell, and Chenfeng Li. A review of hydraulic fracturing simulation. *Archives of Computational Methods in Engineering*, pages 1–58, 2021.
- [37] R. R. Settgast, S. M. Johnson, P. Fu, S. D. C. Walsh, and F. Ryerson. Simulation of hydraulic fracture networks in three dimensions. Technical report, Lawrence Livermore National Lab.(LLNL), Livermore, CA (United States), 2012.
- [38] R. R. Settgast, S. M. Johnson, P. Fu, and S. D. C. Walsh. Simulation of hydraulic fracture networks in three dimensions utilizing massively parallel computing resources. In *SPE/AAPG/SEG Unconventional Resources Technology Conference*. OnePetro, 2014.
- [39] Randolph R Settgast, Pengcheng Fu, Stuart DC Walsh, Joshua A White, Chandrasekhar Annavarapu, and Frederick J Ryerson. A fully coupled method for massively parallel simulation of hydraulically driven fractures in 3-dimensions. *International Journal for Numerical and Analytical Methods in Geomechanics*, 41(5):627–653, 2017.
- [40] H. Zia and B. Lecampion. PyFrac: A planar 3D hydraulic fracture simulator. *Comput. Phys. Commun.*, 255:107368, 2020.
- [41] P Gupta and Carlos Armando Duarte. Simulation of non-planar three-dimensional hydraulic fracture propagation. *International Journal for Numerical and Analytical Methods in Geomechanics*, 38(13):1397–1430, 2014.
- [42] P Gupta and Carlos Armando Duarte. Coupled hydromechanical-fracture simulations of nonplanar three-dimensional hydraulic fracture propagation. *International Journal for Numerical and Analytical Methods in Geomechanics*, 42(1):143–180, 2018.

- [43] Huiying Tang, Shihao Wang, Ruihan Zhang, Sanbai Li, Liehui Zhang, and Yu-Shu Wu. Analysis of stress interference among multiple hydraulic fractures using a fully three-dimensional displacement discontinuity method. *Journal of Petroleum Science and Engineering*, 179:378–393, 2019.
- [44] Sanbai Li, Abbas Firoozabadi, and Dongxiao Zhang. Hydromechanical modeling of nonplanar three-dimensional fracture propagation using an iteratively coupled approach. *Journal of Geophysical Research: Solid Earth*, 125(8):e2020JB020115, 2020.
- [45] Sanbai Li and Dongxiao Zhang. Development of 3-d curved fracture swarms in shale rock driven by rapid fluid pressure buildup: Insights from numerical modeling. *Geophysical Research Letters*, 48(8):e2021GL092638, 2021.
- [46] Hadi Hajibeygi, Dimitris Karvounis, and Patrick Jenny. A hierarchical fracture model for the iterative multiscale finite volume method. *Journal of Computational Physics*, 230(24):8729–8743, 2011.
- [47] Gilles A Francfort and J-J Marigo. Revisiting brittle fracture as an energy minimization problem. *Journal of the Mechanics and Physics of Solids*, 46(8):1319–1342, 1998.
- [48] Blaise Bourdin, Gilles A Francfort, and Jean-Jacques Marigo. Numerical experiments in revisited brittle fracture. *Journal of the Mechanics and Physics of Solids*, 48(4):797–826, 2000.
- [49] Alain Karma, David A Kessler, and Herbert Levine. Phase-field model of mode iii dynamic fracture. *Physical Review Letters*, 87(4):045501, 2001.
- [50] Alan Arnold Griffith. Vi. the phenomena of rupture and flow in solids. *Philosophical Transactions of the Royal Society of London. Series A*, 221(582-593):163–198, 1921.
- [51] Yousef Heider. A review on phase-field modeling of hydraulic fracturing. *Engineering Fracture Mechanics*, 253:107881, 2021.
- [52] Mary F Wheeler, Thomas Wick, and W Wollner. An augmented-lagrangian method for the phase-field approach for pressurized fractures. *Computer Methods in Applied Mechanics and Engineering*, 271:69–85, 2014.
- [53] Christian Miehe, Steffen Mauthe, and Stephan Teichtmeister. Minimization principles for the coupled problem of darcy–biot-type fluid transport in porous media linked to phase field modeling of fracture. *Journal of the Mechanics and Physics of Solids*, 82:186–217, 2015.

- [54] Christian Miehe and Steffen Mauthe. Phase field modeling of fracture in multi-physics problems. part iii. crack driving forces in hydro-poro-elasticity and hydraulic fracturing of fluid-saturated porous media. *Computer Methods in Applied Mechanics and Engineering*, 304:619–655, 2016.
- [55] A Mikelić, Mary F Wheeler, and Thomas Wick. Phase-field modeling of a fluid-driven fracture in a poroelastic medium. *Computational Geosciences*, 19(6):1171–1195, 2015.
- [56] Andro Mikelić, Mary F Wheeler, and Thomas Wick. A phase-field method for propagating fluid-filled fractures coupled to a surrounding porous medium. *Multiscale Modeling & Simulation*, 13(1):367–398, 2015.
- [57] Zachary A Wilson and Chad M Landis. Phase-field modeling of hydraulic fracture. *Journal of the Mechanics and Physics of Solids*, 96:264–290, 2016.
- [58] H. C. Brinkman. A calculation of the viscous force exerted by a flowing fluid on a dense swarm of particles. *Flow Turbul. Combust.*, 1(1):27–34, 1949.
- [59] Chukwudi Chukwudzie, Blaise Bourdin, and Keita Yoshioka. A variational phase-field model for hydraulic fracturing in porous media. *Computer Methods in Applied Mechanics and Engineering*, 347:957–982, 2019.
- [60] Bin Chen, Yanan Sun, Beatriz R Barboza, Andrew R Barron, and Chenfeng Li. Phase-field simulation of hydraulic fracturing with a revised fluid model and hybrid solver. *Engineering Fracture Mechanics*, 229:106928, 2020.
- [61] Keita Yoshioka, Dmitri Naumov, and Olaf Kolditz. On crack opening computation in variational phase-field models for fracture. *Computer Methods in Applied Mechanics and Engineering*, 369:113210, 2020.
- [62] Timo Heister, Mary F Wheeler, and Thomas Wick. A primal-dual active set method and predictor-corrector mesh adaptivity for computing fracture propagation using a phase-field approach. *Computer Methods in Applied Mechanics and Engineering*, 290:466–495, 2015.
- [63] Sanghyun Lee, Mary F Wheeler, and Thomas Wick. Iterative coupling of flow, geomechanics and adaptive phase-field fracture including level-set crack width approaches. *Journal of Computational and Applied Mathematics*, 314:40–60, 2017.
- [64] Timo Heister and Thomas Wick. pfm-cracks: A parallel-adaptive framework for phase-field fracture propagation. *Software Impacts*, 6:100045, 2020.

- [65] Abhinav Gupta, U.~Meenu Krishnan, Tushar Kanti Mandal, Rajib Chowdhury, and Vinh Phu Nguyen. An adaptive mesh refinement algorithm for phase-field fracture models: Application to brittle, cohesive, and dynamic fracture. *Comput. Methods Appl. Mech. Engrg.*, 399:115347, 2022.
- [66] Brice Lecampion, Andrew Bunger, and Xi Zhang. Numerical methods for hydraulic fracture propagation: a review of recent trends. *Journal of Natural Gas Science and Engineering*, 49:66–83, 2018.
- [67] Rudy JM Geelen, Yingjie Liu, John E Dolbow, and Antonio Rodríguez-Ferran. An optimization-based phase-field method for continuous-discontinuous crack propagation. *International Journal for Numerical Methods in Engineering*, 116(1):1–20, 2018.
- [68] Bianca Giovanardi, Anna Scotti, and Luca Formaggia. A hybrid xfem–phase field (xfield) method for crack propagation in brittle elastic materials. *Computer Methods in Applied Mechanics and Engineering*, 320:396–420, 2017.
- [69] Alba Muixí, Onofre Marco, Antonio Rodríguez-Ferran, and Sonia Fernández-Méndez. A combined xfem phase-field computational model for crack growth without remeshing. *Computational Mechanics*, 67(1):231–249, 2021.
- [70] Kangan Li, Antonio Rodríguez-Ferran, and Guglielmo Scovazzi. A blended shifted-fracture/phase-field framework for sharp/diffuse crack modeling. *International Journal for Numerical Methods in Engineering*, 124(4):998–1030, 2023.
- [71] Nicolas Moës, John Dolbow, and Ted Belytschko. A finite element method for crack growth without remeshing. *International Journal for Numerical Methods in Engineering*, 46(1):131–150, 1999.
- [72] Yuan Sun, Zhiyuan Liu, and Xuhai Tang. A hybrid femm-phase field method for fluid-driven fracture propagation in three dimension. *Engineering Analysis with Boundary Elements*, 113:40–54, 2020.
- [73] Samuel Burbulla, Luca Formaggia, Christian Rohde, and Anna Scotti. Modeling fracture propagation in poro-elastic media combining phase-field and discrete fracture models. *Computer Methods in Applied Mechanics and Engineering*, 403:115699, 2023.
- [74] JiaNing Zhang, Hao Yu, WenLong Xu, ChengSi Lv, Marembo Micheal, Fang Shi, and HengAn Wu. A hybrid numerical approach for hydraulic fracturing in a naturally fractured formation combining the xfem and phase-field model. *Engineering Fracture Mechanics*, 271:108621, 2022.

- [75] Andre Costa, Tianchen Hu, and John E Dolbow. On formulations for modeling pressurized cracks within phase-field methods for fracture. *Theoretical and Applied Fracture Mechanics*, 127:104040, 2023.
- [76] Tianchen Hu. *A Variational Framework for Phase-Field Fracture Modeling with Applications to Fragmentation, Desiccation, Ductile Failure, and Spallation*. PhD thesis, Duke University, 2021.
- [77] Eric Lorentz, Sam Cuvilliez, and Kyrylo Kazymyrenko. Convergence of a gradient damage model toward a cohesive zone model. *Comptes Rendus Mécanique*, 339(1):20–26, 2011.
- [78] Rudy JM Geelen, Yingjie Liu, Tianchen Hu, Michael R Tupek, and John E Dolbow. A phase-field formulation for dynamic cohesive fracture. *Computer Methods in Applied Mechanics and Engineering*, 348:680–711, 2019.
- [79] Jian-Ying Wu. A unified phase-field theory for the mechanics of damage and quasi-brittle failure. *Journal of the Mechanics and Physics of Solids*, 103:72–99, 2017.
- [80] Andro Mikelić, Mary F Wheeler, and Thomas Wick. A quasi-static phase-field approach to pressurized fractures. *Nonlinearity*, 28(5):1371, 2015.
- [81] Christian Peco, Wei Chen, Yingjie Liu, MM Bandi, John E Dolbow, and Eliot Fried. Influence of surface tension in the surfactant-driven fracture of closely-packed particulate monolayers. *Soft Matter*, 13(35):5832–5841, 2017.
- [82] Wen Jiang, Tianchen Hu, Larry K Aagesen, Sudipta Biswas, and Kyle A Gamble. A phase-field model of quasi-brittle fracture for pressurized cracks: Application to UO<sub>2</sub> high-burnup microstructure fragmentation. *Theoretical and Applied Fracture Mechanics*, 119:103348, 2022.
- [83] Paul Sicsic and Jean-Jacques Marigo. From gradient damage laws to griffith's theory of crack propagation. *Journal of Elasticity*, 113(1):55–74, 2013.
- [84] Roberto Ballarini and Gianni Royer-Carfagni. Closed-path j-integral analysis of bridged and phase-field cracks. *Journal of Applied Mechanics*, 83(6), 2016.
- [85] MZ Hossain, C-J Hsueh, B Bourdin, and K Bhattacharya. Effective toughness of heterogeneous media. *Journal of the Mechanics and Physics of Solids*, 71: 15–32, 2014.
- [86] Fang Zhong Li, C Fong Shih, and A Needleman. A comparison of methods for calculating energy release rates. *Engineering Fracture Mechanics*, 21(2): 405–421, 1985.

- [87] CF Shih, B Moran, and T Nakamura. Energy release rate along a three-dimensional crack front in a thermally stressed body. *International Journal of Fracture*, 30(2):79–102, 1986.
- [88] Hanen Amor, Jean-Jacques Marigo, and Corrado Maurini. Regularized formulation of the variational brittle fracture with unilateral contact: Numerical experiments. *Journal of the Mechanics and Physics of Solids*, 57(8):1209–1229, 2009.
- [89] Christian Miehe, Martina Hofacker, and Fabian Welschinger. A phase field model for rate-independent crack propagation: Robust algorithmic implementation based on operator splits. *Computer Methods in Applied Mechanics and Engineering*, 199(45-48):2765–2778, 2010.
- [90] Emmanuel Detournay. Mechanics of hydraulic fractures. *Annual Review of Fluid Mechanics*, 48:311–339, 2016.
- [91] Andrew P Bunger, Emmanuel Detournay, and Dmitry I Garagash. Toughness-dominated hydraulic fracture with leak-off. *International Journal of Fracture*, 134(2):175–190, 2005.
- [92] Tianchen Hu, Brandon Talamini, Andrew J Stershic, Michael R Tupek, and John E Dolbow. A variational phase-field model for ductile fracture with coalescence dissipation. *Computational Mechanics*, 68(2):311–335, 2021.
- [93] Wen Jiang, Tianchen Hu, Larry K Aagesen, and Yongfeng Zhang. Three-dimensional phase-field modeling of porosity dependent intergranular fracture in UO<sub>2</sub>. *Computational Materials Science*, 171:109269, 2020.
- [94] Eric Lorentz and V Godard. Gradient damage models: Toward full-scale computations. *Computer Methods in Applied Mechanics and Engineering*, 200(21–22):1927–1944, 2011.
- [95] James R Rice et al. Mathematical analysis in the mechanics of fracture. *Fracture: an advanced treatise*, 2:191–311, 1968.
- [96] James R Rice. A path independent integral and the approximate analysis of strain concentration by notches and cracks. *Journal of Applied Mechanics*, 35(2):379–386, 1968.
- [97] A. Karlsson and J. Backlund. J-integral at loaded crack surfaces. *International Journal of Fracture*, 14:311–318, 1978.
- [98] W. Karush. Minima of functions of several variables with inequalities as side constraints. *M. Sc. Dissertation. Dept. of Mathematics, Univ. of Chicago*, 1939.

- [99] H. W. Kuhn and A. W. Tucker. Nonlinear Programming. In *Proceedings of the Second Berkeley Symposium on Mathematical Statistics and Probability*, pages 481–492. University of California Press, 1951.
- [100] Tianchen Hu, Johann Guilleminot, and John E Dolbow. A phase-field model of fracture with frictionless contact and random fracture properties: Application to thin-film fracture and soil desiccation. *Computer Methods in Applied Mechanics and Engineering*, 368:113106, 2020.
- [101] Tianchen Hu. RACCOON - a parallel finite-element code specialized in phase-field for fracture, 2020. URL <https://hugary1995.github.io/raccoon/index.html>.
- [102] Derek Gaston, Chris Newman, Glen Hansen, and Damien Lebrun-Grandjean. Moose: A parallel computational framework for coupled systems of nonlinear equations. *Nuclear Engineering and Design*, 239(10):1768–1778, 2009.
- [103] Cody J Permann, Derek R Gaston, David Andrs, Robert W Carlsen, Fande Kong, Alexander D Lindsay, Jason M Miller, John W Peterson, Andrew E Slaughter, Roy H Stogner, et al. Moose: Enabling massively parallel multi-physics simulation. *SoftwareX*, 11:100430, 2020.
- [104] Alexander D Lindsay, Derek R Gaston, Cody J Permann, Jason M Miller, David Andrs, Andrew E Slaughter, Fande Kong, Joshua Hansel, Robert W Carlsen, Casey Icenhour, et al. 2.0-moose: Enabling massively parallel multi-physics simulation. *SoftwareX*, 20:101202, 2022.
- [105] Ferdinand Stoeckhert, Michael Molenda, Sebastian Brenne, and Michael Alber. Fracture propagation in sandstone and slate—laboratory experiments, acoustic emissions and fracture mechanics. *Journal of Rock Mechanics and Geotechnical Engineering*, 7(3):237–249, 2015.
- [106] Andre Costa, Matteo Cusini, Tao Jin, Randolph Settgast, and John E Dolbow. A multi-resolution approach to hydraulic fracture simulation. *International Journal of Fracture*, 237(1-2):165–188, 2022.
- [107] Maurice A Biot. General theory of three-dimensional consolidation. *Journal of Applied Physics*, 12(2):155–164, 1941.
- [108] F. Erdogan and G. C. Sih. On the Crack Extension in Plates Under Plane Loading and Transverse Shear. *Jour. of Basic Eng.*, 85(4):519–525, 12 1963. ISSN 0021-9223.
- [109] JG Williams and PD Ewing. Fracture under complex stress—the angled crack problem. *Int. J. of Frac. Mech.*, 8(4):441–446, 1972.

- [110] I Finnie and A Saith. A note on the angled crack problem and the directional stability of cracks. *Int. J. of Fracture*, 9(4):484–486, 1973.
- [111] PD Ewing, JL Swedlow, and JG Williams. Further results on the angled crack problem. *Int. J. of Fracture*, 12(1):85–93, 1976.
- [112] B Cotterell. On brittle fracture paths. *Int. J. of Frac. Mech.*, 1(2):96–103, 1965.
- [113] MA Hussain, L Pu, and J Underwood. Strain energy release rate for. In *Proceedings of the 1973 National Symposium on Fracture Mechanics, University of Maryland, College Park, Md., 27-29 Aug. 1973*, volume 559, page 2, 1974.
- [114] Bo He and Xiaoying Zhuang. Modeling hydraulic cracks and inclusion interaction using xfem. *Underground Space*, 3(3):218–228, 2018.
- [115] Youngho Jang, Gayoung Park, Seoyoon Kwon, and Baehyun Min. Analysis of hydraulic fracture propagation using a mixed mode and a uniaxial strain model considering geomechanical properties in a naturally fractured shale reservoir. *Geofluids*, 2020, 2020.
- [116] Benjamin E Grossman-Ponemon and Adrian J Lew. An algorithm for the simulation of curvilinear plane-strain and axisymmetric hydraulic fractures with lag using the universal meshes. *Int. J. Numer. Anal. Methods Geomech.*, 43(6):1251–1278, 2019.
- [117] N. Shauer and C. A. Duarte. A three-dimensional Generalized Finite Element Method for simultaneous propagation of multiple hydraulic fractures from a wellbore. *Eng. Fract. Mech.*, 265:108360, 2022.
- [118] Luigi Ambrosio and Vincenzo Maria Tortorelli. Approximation of functional depending on jumps by elliptic functional via t-convergence. *Communications on Pure and Applied Mathematics*, 43(8):999–1036, 1990.
- [119] Christian Linder and Francisco Armero. Finite elements with embedded strong discontinuities for the modeling of failure in solids. *International Journal for Numerical Methods in Engineering*, 72(12):1391–1433, 2007.
- [120] Seong H Lee, MF Lough, and CL Jensen. Hierarchical modeling of flow in naturally fractured formations with multiple length scales. *Water Resources Research*, 37(3):443–455, 2001.
- [121] David Santillán, Ruben Juanes, and Luis Cueto-Felgueroso. Phase field model of hydraulic fracturing in poroelastic media: Fracture propagation, arrest, and branching under fluid injection and extraction. *Journal of Geophysical Research: Solid Earth*, 123(3):2127–2155, 2018.

- [122] Hu Tianchen, Johann Guilleminot, and John Dolbow. A phase-field model of fracture with frictionless contact and random fracture properties: Application to thin-film fracture and soil desiccation. *Computer Methods in Applied Mechanics and Engineering*, 368, 2020.
- [123] K. Pham, H. Amor, J.-J. Marigo, and C. Maurini. Gradient damage models and their use to approximate brittle fracture. *Int. J. Damage Mech.*, 20(4):618–652, 2011.
- [124] Blaise Bourdin, Gilles A Francfort, and Jean-Jacques Marigo. The variational approach to fracture. *Journal of elasticity*, 91(1-3):5–148, 2008.
- [125] Elena Tamayo-Mas and Antonio Rodríguez-Ferran. A medial-axis-based model for propagating cracks in a regularised bulk. *Internat. J. Numer. Methods Engrg.*, 101(7):489–520, 2015.
- [126] M. Isida. Analysis of stress intensity factors for the tension of a centrally cracked strip with stiffened edges. *Eng. Fract. Mech.*, 5(3):647–665, 1973.
- [127] T. Jin, J. A. White, and R. R. Settgast. A robust finite element-finite volume strategy for viscosity-dominated hydraulic fracture propagation using asymptotic tip enrichment. *Int. J. Numer. Anal. Methods Geomech.*, 2022.
- [128] Douglas N Arnold, Franco Brezzi, and Michel Fortin. A stable finite element for the stokes equations. *Calcolo*, 21(4):337–344, 1984.
- [129] Joshua A White and Ronaldo I Borja. Stabilized low-order finite elements for coupled solid-deformation/fluid-diffusion and their application to fault zone transients. *Computer Methods in Applied Mechanics and Engineering*, 197(49–50):4353–4366, 2008.
- [130] Mark McClure. The case for planar fracture modeling. Talk presented at ARMA HFC Robe Talk Series, 2020. URL <https://www.youtube.com/watch?v=qZxRGvJAKFE>.
- [131] Liang Yang, Yongtao Yang, Hong Zheng, and Zhijun Wu. An explicit representation of cracks in the variational phase field method for brittle fractures. *Computer Methods in Applied Mechanics and Engineering*, 387:114127, 2021.
- [132] Jun Zeng, Mengnan Zhang, Erjie Yang, Fucheng Tian, and Liangbin Li. A tracking strategy for multi-branched crack tips in phase-field modeling of dynamic fractures. *International Journal for Numerical Methods in Engineering*, 123(3):844–865, 2022.
- [133] Yue Xu, Tao You, and Qizhi Zhu. Reconstruct lower-dimensional crack paths from phase-field point cloud. *International Journal for Numerical Methods in Engineering*, 2023.

- [134] Hazem Eldahshan, José Alves, Pierre-Olivier Bouchard, Etienne Perchat, and Daniel Pino Munoz. Cipfar: A 3d unified numerical framework for the modeling of ductile fracture based on the phase field model and adaptive remeshing. *Computer Methods in Applied Mechanics and Engineering*, 387:114171, 2021.
- [135] Aditya Kumar, Blaise Bourdin, Gilles A Francfort, and Oscar Lopez-Pamies. Revisiting nucleation in the phase-field approach to brittle fracture. *Journal of the Mechanics and Physics of Solids*, 142:104027, 2020.
- [136] G. R. Irwin. Analysis of Stresses and Strains Near the End of a Crack Traversing a Plate. *Journal of Applied Mechanics*, 24(3):361–364, 1957.
- [137] R. Fosdick and L. Truskinovsky. About Clapeyron’s Theorem in Linear Elasticity. *Journal of Elasticity*, 72:145–172, 2003.
- [138] Zdenek P Bazant and Jaime Planas. *Fracture and size effect in concrete and other quasibrittle materials*. Routledge, 2019.

# Biography

Andre Costa earned his B.S. degree in Mechanical Engineering and M.S. degree in Mathematics from Universidade Federal de Minas Gerais, in Brazil. He joined the Department of Mechanical Engineering and Materials Science at Duke University in 2018 as a graduate research assistant. His Ph.D. degree was awarded in the Fall of 2023 and he will be working as a Software Engineer at Cadence Design Systems Inc.